

Role of shape in the self-assembly of
anisotropic colloids
by
Benjamin Arthur Schultz

A dissertation submitted in the partial fulfillment
of the requirements of the degree of
Doctor of Philosophy
(Physics)
in the University of Michigan
2015

Doctoral Committee:

Professor Sharon Glotzer, Chair
Professor Ronald Larson
Assistant Professor Xiaoming Mao
Professor Leonard Sander
Professor Michael Solomon

For Kiersten - whose love, patience and support have been unwavering.

Acknowledgements

The work contained in this thesis belongs as much to me as it does to the many intelligent and creative people with whom I've had the pleasure to work at Michigan

I'd like to acknowledge my dissertation committee: Sharon Glotzer, for her being an excellent ring-leader, scientist, advisor, all while being *cool*, for letting me follow my interests like a dowsing rod and for her patience; Michael Solomon, for his unmatched kindness, expertise and honesty; Xiaoming Mao, whose work I knew before I ever met her, for bringing her talent to Michigan Physics; Len Sander, for teaching me the fundamentals; Ron Larson, for his admirable rigor and insightful questions.

I'd like to further acknowledge Greg van Anders, for being an exemplary scientist, human being and role model; Michael Engel for his indefatigable intellect; Jens Glaser, for his boundless enthusiasm and making everything at least one order of magnitude faster than it needs to be; Joshua Anderson, for teaching me how to code effectively, for HOOMD-blue, for all his work maintaining our computing resources and for beating me at just about every board game we've ever played together; Daphne Klotsa for her creativity and insights; Eric Jankowski for his friendship, guidance and puns; Trung Nguyen for his tireless enthusiasm for our work; Daniel Beltran, for his patience when a bug in my code cost us nearly a month of simulation time; Aayush Shah, for being an excellent collaborator and mentor; Lilian Hsiao, for being another excellent collaborator; Khalid Ahmed for lively discussions and tolerating my coffee grinder for years; Ryan Marson, for his friendship, scholarship and down-home cooking; Eric Irrgang, for being a sweetheart and leaving no nit unpicked; Pablo Damasceno, for his scientific insights and Brazilian barbecue; the rest of the Glotzer group, who are all so interesting, smart and relatable that I have made it this far and still find Ph. D. comics unrelatable; Karen Coulter, for a list of things longer than this dissertation; and Common Cycle and my biking friends, for providing an escape every time I've needed it.

Contents

Dedication	ii
Acknowledgements	iii
List of Figures	viii
List of Tables	xi
Abstract	xii
Chapter 1: Introduction.	1
1.1 Entropic self-assembly	5
1.2 Emergent attraction	6
1.3 Surface anisotropy and shape	8
1.4 Summary	9
Chapter 2: Symmetry Considerations for the Targeted Assembly of Entropically Sta- bilized Colloidal Crystals via Voronoi Particles	10
2.1 Introduction	11
2.2 Background and approach	13
2.3 Results	15

2.3.1	General findings	15
2.3.2	An example: hexagonal diamond Voronoi particle	17
2.3.3	Beyond single component systems	20
2.3.4	Assembly engineering via mesoblock assembly	22
2.3.5	Discussion	24
2.4	Conclusions	25
2.5	Model and methods	26
2.5.1	Voronoi particle construction	26
2.5.2	Properties of Voronoi particles	27
2.5.3	Monte Carlo simulations of self-assembly	29
2.5.4	Field-directed self-assembly	30
2.5.5	Structural identification	30
2.5.6	Free energy calculations	31
2.5.7	Calculation of VP orientational correlation function	32
2.5.8	Coexistence simulations of hexagonal diamond VPs	33
Chapter 3:	Image processing of confocal image volumes	47
3.1	3-dimensional images in self-assembly	47
3.2	Beyond monodisperse spheres	48
3.3	A watershed segmentation approach to particle identification	50
3.4	Position and orientation identification	52
3.5	Implementation and verification	54

3.6	Conclusions	56
Chapter 4:	Self-assembly of depleted, oblate colloidal ellipsoids	63
4.1	Introduction	63
4.2	Materials and methods	65
4.2.1	Colloidal synthesis, stability, and self-assembly of PMMA oblate spheroids	65
4.2.2	Confocal microscopy imaging	69
4.2.3	Image processing and quantification of cluster aggregation and orientational order	69
4.2.4	Monte Carlo simulations of depletion-induced aggregation	71
4.2.5	Analytic ellipsoid-ellipsoid overlap check	72
4.3	Results	74
4.3.1	Phase behavior of self-assembled oblate spheroids	74
4.3.2	Kinetics of orientational self-assembly	76
4.4	Discussion	78
Chapter 5:	Actuation of shape-memory colloidal fibers of Janus ellipsoids	88
5.1	Introduction	88
5.2	Janus ellipsoid self-assembly	89
5.3	Phase diagram and mechanism of Janus ellipsoid self assembly	92
5.4	Simulations of Janus ellipsoid equilibrium assembly	95
5.4.0.1	Computational phase diagram: fluid and horizontal fiber phase	97
5.4.0.2	Janus balance and sharpness effects	98

5.5	Directed assembly of Janus ellipsoids by AC electric fields	99
5.5.1	Simulations of Janus ellipsoid configurations in AC field	101
5.6	Actuation of Janus ellipsoid fibers by AC electric fields	102
5.7	Control of Janus ellipsoid fiber length	104
5.8	Experimental methods	106
5.8.1	Janus ellipsoid synthesis	106
5.8.2	Chamber for AC electric field device	107
5.8.3	Synthesis of ellipsoids with varying aspect ratios	108
5.8.4	Self-Assembly of Janus ellipsoids	108
5.8.5	Self-assembly of carboxylate-stabilized Janus ellipsoid particles	109
5.8.6	AC field assembly of Janus ellipsoids	110
5.9	Hypotheses: mechanisms driving elongation of chains in AC electric fields	110
5.9.1	Competition between induced dipoles and electrostatic monopoles	111
5.9.2	Force driven compression of Janus ellipsoid chains	112
5.9.2.1	Current induced compressive forces	112
5.9.2.2	Electrophoretic forces of elongation	113
5.10	Outlook	114
Chapter 6:	Outlook.	128
Appendix		131
Bibliography		146

List of Figures

2.1	Construction and self assembly of Voronoi particles.	34
2.2	Voronoi particle assembly results	40
2.3	Thermodynamics of the hexagonal diamond Voronoi particle	41
2.4	Examples of orientationally degenerate crystals	42
2.5	Examples of binary Voronoi particle systems.	43
2.6	Mesoblock construction and field-directed assembly of Voronoi particles . . .	44
2.7	Phase coexistence of hexagonal diamond Voronoi particles in fluid and hexagonal diamond phases	45
2.8	Phase coexistence of hexagonal diamond Voronoi particles in orientationally degenerate diamond and hexagonal diamond phases	46
3.1	Schematic of a confocal microscope.	57
3.2	Example of the watershed cut with pre-flooding filter.	58
3.3	Benchmarks of the Gaussian blur filter.	59
3.4	Error magnitude as a function of noise for particle identification.	60
3.5	Flow diagram of ellipsoid particle identification	61

3.6	Image processing of prolate and oblate spheroids	62
4.1	Synthesis and stability of PMMA oblate spheroids	82
4.2	Phase behavior of colloidal oblate spheroids as a function of attraction strength	83
4.3	Kinetics of oriented and non-oriented self-assembly.	84
4.4	Valence of spheres and ellipsoids suspensions in simulation.	85
4.5	Effective interaction potential between two oblate ellipsoids.	86
4.6	Stability of colloid oblate spheroids without depletant.	87
5.1	Janus ellipsoid self-assembly at different NaCl concentrations	115
5.2	Phase diagram of Janus self-ellipsoid assembly and mechanism of Janus ellip- soid assembly	116
5.3	AC electric field assisted assembly of Janus ellipsoids.	117
5.4	Actuation of Janus ellipsoid fibers using AC electric fields.	118
5.5	Changes in Janus fiber length by AC electric fields.	119
5.6	Plots of the anisotropic potential used for simulations at 1.0 mM NaCl. . . .	120
5.7	Plots of the anisotropic potential used for simulations at 2.5 mM NaCl. . . .	121
5.8	Further plots of the Janus ellipsoid interaction potential	122
5.9	Simulation images of self-assembled phases of Janus ellipsoids in AC fields. .	123
5.10	Schematics of the electrostatic interactions in the CL and SC structures. . .	123
5.11	CLSM images of carboxylate-stabilized ellipsoid ($r = 5$) self-assembly.	124
5.12	CLSM images of Janus ellipsoid structures in an AC-field	124
5.13	Phase diagram of Janus ellipsoids in temperature and screening length. . . .	125

5.14	Phase diagram of Janus ellipsoids as a function of χ	126
5.15	Phase diagram of Janus ellipsoids as a function of w	127
A.1	Family of singly and triply truncated triangles	137
A.2	Singly truncated triangle crystals.	139
A.3	Triply truncated triangle crystals.	140
A.4	Extraction of work from changing particle truncation.	141
A.5	Valid thermodynamic integration paths for singly and triply truncated triangles	141
A.6	Family of complementary, hexagon-forming particles	143
A.7	Crystals formed by a) complementary and b) self-complementary particles .	143
A.8	Thermodynamic integration path to compare complementary and self-complementary particles	145

List of Tables

2.1	Table of Voronoi polyhedra that self assemble their space-filling structure . .	35
2.2	Table of Voronoi polyhedra that self assemble a non-space-filling crystal in- stead of their target crystal	36
2.3	Table 2.2, cont. (1)	37
2.4	Table 2.2, cont. (2)	38
2.5	Table of Voronoi polyhedra that do not self assemble a crystal	39
3.1	Standard deviations in particle number, positions and orientations from pro- cessing an arrested volume of oblate PMMA spheroids	56
5.1	Table of Janus ellipsoid potential parameters	97

Abstract

Self-assembly is the process of spontaneous organization of a set of interacting components - colloidal particles in suspension interacting with one another can organize into crystals, gels, glasses and even primitive devices on the microscale. We examine how particle shape - one of many possible interparticle interactions - drives the self-assembly of colloids in three different colloidal systems. When particles interact only via their shape, entropic crystallization can occur; we discuss a design strategy for creating hard, polyhedral particles that entropically stabilize arbitrary crystal structures. As a strategy for targeting novel crystal structures, we examine the use of Voronoi particles, which are hard, space-filling particles in the shape of Voronoi cells of a target structure. Although Voronoi particles stabilize their target structure in the limit of high pressure by construction, the thermodynamic assembly of the same structure at moderate pressure, close to the onset of crystallization, is not guaranteed. Indeed, we find that a more symmetric crystal is often preferred due to additional entropic contributions of several $k_B T$ arising from configurational or occupational degeneracy. We characterize the assembly behavior of the Voronoi particles in terms of the symmetries of the building blocks as well as the symmetries of crystal structures and demonstrate how controlling the degeneracies through a modification of particle shape and field-directed assembly can significantly improve the assembly propensity.

With the addition of non-adsorbing, polymer depletants, hard colloids experience an emergent attraction dependent on polymer concentration, the form of which is dictated by the colloid shape; we study a system of oblate, spheroidal colloids that self-assemble

thread-like clusters. We develop methods to identify particle position and orientation, and apply them in a joint analysis of experimental systems. In both simulation and experiment the colloids condense into orientationally disordered droplets at low polymer concentrations; at higher concentrations, where we expect orientational alignment, we observe kinetic arrest into primarily linear clusters of aligned colloids. We show that these low-valence structures are a result of the anisotropic particle shape, which give rise to an effective potential capable of forming mechanically stable, low valence structures.

Furthermore, particle surfaces can be patterned with metal coatings, introducing enthalpic attraction between particles; we study a system of prolate spheroidal colloids, half-coated in gold. These particles assemble one dimensional fibers that can be reversibly actuated upon the application of an electric field. Many natural micrometer-scale assemblies can be actuated to control their optical, transport, and mechanical properties, yet such functionality is lacking in colloidal structures synthesized thus far. Here, we show with experiments and computer simulations that Janus ellipsoids can self-assemble into self-limiting one-dimensional fibers with shape-memory properties, and that the fibrillar assemblies can be actuated on application of an external alternating-current electric field. Actuation of the fibers occurs through a sliding mechanism (allowed by the curved ellipsoidal surfaces) that permits the rapid and reversible elongation and contraction of the Janus-ellipsoid chains by 36%. Colloidal-scale actuation might be useful in microrobotics and in applications of shape-memory materials.

In these three, significantly different colloidal systems, we find shape plays a

critical role. By understanding and isolating its impact, we enhance shape's utility as a parameter for the design of self-assembling colloids.

Chapter 1

Introduction

Self assembly encompasses the process and outcome of the spontaneous structure formation from a system comprised of interacting components [1]. Self assembly is perhaps easiest understood in contrast to top-down, guided assembly, in which an agent with global knowledge of the end structure directs the components; instead the end structure is encoded into interactions of the components with each other and their environment. This broad definition applies to physical systems at every scale - from cosmological[2] to nanoscale[3], from economic markets[4] to biological systems[5, 6] to biocompatible materials[7] and robotic swarms[8, 9].

The focus of this thesis is on the thermodynamic self assembly of colloidal particles. Thermodynamic self-assembly specifies a subset of self assembly in which thermal fluctuations drive random particle motion and minimize the system's free-energy[1]. Colloids are particles of matter ranging from the nano- to microscale, often suspended in solution.

At the colloidal scale, there are relatively few types of interactions that participate in driving self assembly [10, 11]. The work presented in this thesis includes particles interacting via excluded-volume interactions (particles cannot occupy the same space), van der Waals interactions (an attractive force arising from fluctuating dipole moments in the particles), hydrophobic interaction (a chemical tendency for certain surfaces to avoid water, driving mutual attraction) and depletion (an imbalance of osmotic pressure that drives large particles in solution with smaller particles close together). Interactions of these types are generically described by an interaction potential

$$U = f(\vec{r}_1 \dots \vec{r}_N) \tag{1.1}$$

where f is an arbitrary function and \vec{r}_i is a coordinate vector describing all the degrees of freedom of particle i . In many cases this function is accurately described by a sum of pair-wise interactions, with three- and more-body interactions entering the equations as corrections [12].

$$U = \sum_{i \neq j} U_{pair}(\vec{r}_i, \vec{r}_j) + \dots \tag{1.2}$$

where U_{pair} describes the pair-wise interactions, such as excluded volume. The connection between particle interactions and bulk thermodynamic behavior and structures is described by statistical mechanics. For a system with N particles, fixed volume V and held at temperature $T = k_B/\beta$ (k_B is Boltzmann's constant), it can be shown that the probability of observing a state described by $\{\vec{r}_1 \dots \vec{r}_N\}$ is proportional to $\exp(-\beta U(\vec{r}_0 \dots \vec{r}_N))$ (Boltzmann

distribution). The partition function Z is a sum over all possible states; in classical physics, it becomes an integral.

$$Z = \int d\vec{r}_1 \dots \int d\vec{r}_N \exp \left(-\beta \sum_{i \neq j} \sum U_{pair}(\vec{r}_i, \vec{r}_j) \right) \quad (1.3)$$

where the sum is taken over all particle pairs. We connect to the microscopic picture of a system to the observable quantities through macrostates - sets of microstates for which a given observable A has some values A_0 . A system in thermal equilibrium will evolve to a macrostate (a collection of microstates $\{\vec{r}_1 \dots \vec{r}_N\}$) that minimize its free energy, defined as

$$F = -k_B \ln(Z) \quad (1.4)$$

For all but the simplest cases exact evaluation of the partition function is impossible, though there exist many perturbative treatments [12]. However, it is possible to sample thermodynamic systems that escape analytical description using computational techniques such as molecular dynamics (integrating particle dynamics with a modified form of Newton's equation to fix temperature and/or pressure), Monte Carlo methods (a statistical scheme for sampling microstates according to the appropriate Boltzmann distribution) or combinations of the two[13].

The work presented in this thesis employs both Monte Carlo and molecular dynamics methods in close connection to experimental work to understand the role of shape in the self assembly of anisotropic colloids. The last decade has seen tremendous growth

in the library of synthesizable colloids. Glotzer and Solomon [14] set forth anisotropy dimensions as a framework for describing the many different types of anisotropies that can be introduced to a colloid. Beginning with a spherical particle, the surface can be modified with, for example, a metallic coating [15], to make regions of the particle’s surface attractive. The extent and patterning of this surface modification is described by the ”patchiness” dimension. Similarly, particles may be faceted[16], branched[17] or stretched[18]. These dimensions introduce shape to the particle - which, in the context of the pair-wise interactions described above, is a volume exclusion interaction that depends both on particle orientation and position -

$$U_{shape}(\vec{r}_i, \vec{q}_i, \vec{r}_j, \vec{q}_j) = \begin{cases} \infty : \text{if overlap} \\ 0 : \text{else} \end{cases} \quad (1.5)$$

. where \vec{r} , and \vec{q} are the translational and rotational degrees of freedom, respectively. U_{shape} may be “softened” with an algebraic divergence as shapes begin to overlap, such as in the discrete-element method[19] - ”shape” encompasses short-range, anisotropic repulsion. In the following chapters, the role of the contribution of this term to the free energy and particle interactions is investigated for three different systems.

1.1 Entropic self-assembly

The work described in Chapter 1 is limited to systems with only interactions of the form of Eq. 1.5, the partition function reduces to a sum or integral over allowable configurations,

$$Z = \int_{\Omega_1^*} d\vec{r}_1 \dots \int_{\Omega_N^*} d\vec{r}_N \quad (1.6)$$

, where Ω_i is the domain of the integral over \vec{r}_i which produces no overlaps with any other particles. In this special case, we can think of the free energy of the system as completely dominated by the entropy S [20, 21, 22], defined as

$$S = k_B T \ln(\Omega) \quad (1.7)$$

where Ω is the number of microstates available to the system. In these systems, minimizing the free energy proceeds by maximizing entropy; the most probable macrostate minimizes the free energy. In systems of hard spheres, if 49.4% of the system volume is occupied by particles, the particles crystallize[23]; by providing an identical environment for all particles, the system maximizes the number of accessible, non-overlapping configurations.

As shown in many recent papers [24, 25, 26, 22, 16, 27, 28, 29, 30], colloidal particles with faceted shapes can thermodynamically stabilize a wide variety of crystal structures from entropy alone; hard tetrahedra even self assemble a quasicrystal [31]. In Chapter 2, we devise a method to design shapes to self assemble arbitrary crystal structures and by

studying the failings of this method, refine our understanding of how particle symmetry - and lack thereof - can modify the shape-entropy of the system.

1.2 Emergent attraction

In Chapters 3 and 4, we relax the constraint that all interactions have the form of Eq. 1.5 and study a system governed by volume exclusions between colloids and polymers, but consider the polymers to be mutually penetrable [32]. In this system, investigated both experimentally and *in silico*, we study oblate ellipsoid colloids of aspect ratio $\epsilon = 0.5$ in suspension with polymers at varying density. Surrounding each colloid is a layer that is impenetrable to the polymers that is on the order of their radius of gyration, R_G . As two colloids approach one another, the excluded halo surrounding each colloid begins to overlap. As a result, there is more accessible volume to each polymer - their Ω_i increases, yielding a net increase in system entropy. In such systems, the colloids are driven towards aggregation because as they aggregate, the entropy of the polymers to increases, lowering the overall free energy. Thus, there is a net attraction between the colloids which depends on the amount of overlapping volume of their excluded volume halos. This attraction is “emergent”; all components of the system are strictly repulsive, yet there is an effective attraction that arises from the thermodynamic behavior of the polymers.

The emergent attraction is analytically quantifiable if we model the polymers as ideal, penetrable hard spheres[33]; the polymers are represented as spheres of radius $\approx R_G$ that have an non-overlap interaction with the colloids, but do not interact with each other.

In this case we can factor the partition function thusly:

$$Z = \int_{\Omega_1^*} d\vec{r}_1 \dots \int_{\Omega_{N_{polymer}^*}} d\vec{r}_{N_{polymer}} \int_{\Omega_1^*} d\vec{r}_1 \dots \int_{\Omega_{N_{colloid}^*}} d\vec{r}_{N_{colloid}} \quad (1.8)$$

$$Z = V_{free}^{N_{polymer}} \int_{\Omega_1^*} d\vec{r}_1 \dots \int_{\Omega_{N_{colloid}^*}} d\vec{r}_{N_{colloid}}. \quad (1.9)$$

where V_{free} is the volume accessible to the polymers. In terms of free energy, this results in

$$F = -k_B T N_{polymer} \ln(V_{free}) - S_{colloid} + F_0 \quad (1.10)$$

where $S_{colloid}$ is the entropy of the colloids and F_0 is a constant offset. There is a competition between $S_{colloid}$, which at low densities promotes a disperse state, and maximizing V_{free} , which promotes colloidal aggregation. The impact of colloid shape in these systems is encoded in V_{free} - the amount of overlapping excluded volume depends on their relative position and orientation in anisotropic particles; V_{free} encodes an anisotropic, emergent attractive interaction between colloids.

In Chapter 3, image processing methods are developed to perform quantitative image processing of anisotropic particles in the spirit of [34], allowing for direct comparison between experimental and computational studies. These methods are then applied to a joint computational and experimental studies of oblate colloidal spheroids in Chapter 4. In this system, which undergoes arrest *en route* to thermodynamic equilibrium, the colloid shape

dictates the local structure of the arrested state.

1.3 Surface anisotropy and shape

In Chapter 6, attractive and long-range repulsive interactions are introduced in addition to shape. In a second joint computational and experimental study, nearly identical colloids to those studied in Chapter 4 are elongated into prolate spheroids rather than oblate spheroids and then additionally coated with an attractive layer of gold and chrome covering half the particle along their major axis. The particles are electrostatically charged as well; in solution, the range of this repulsion can be tuned by adding salt to solution.

Spherical patchy particles have been shown to assemble chiral strands[35], open lattices [36, 37], micelles [38] and bilayers [39] in thermal equilibrium. The surface modification of the elongated particles drives them to self assemble into one-dimensional fibers; as discussed in detail in Chapter 6, the curved surface of the particles promotes achiral, one-dimensional ordering and plays an important role in the kinetics and structure of their assembly.

Additionally, these particles are subjected to an external electric field. External fields can induce interesting behavior in patchy particle systems due to a heterogeneous response to the field (e.g. staggered chains[40], reconfigurable fibers[41] and self-propelled particles[42]). In Chapter 5, upon application of the field the particles reconfigure into elongated versions of their self assembled fiber. The spheroidal shape of the particles allows for the reversible, diffusionless elongation, creating a micro-actuator.

1.4 Summary

In the absence of all interactions, particle shape alone can produce a surprising diversity of ordered assemblies. This thesis presents a series of self assembly studies which gradually add interactions to systems of particles with anisotropic shapes; even as these interactions are introduced, shape plays a critical role in the self assembly processes and material function.

Chapter 2

Symmetry Considerations for the Targeted Assembly of Entropically Stabilized Colloidal Crystals via Voronoi Particles

The contents of this chapter are drawn from a manuscript coauthored with Pablo Damasceno, Michael Engel and Sharon Glotzer. All figure panels were jointly prepared by all authors; Benjamin Schultz is the primary author and conducted all simulations and data analysis.

2.1 Introduction

Once a scientific curiosity, the assembly of nanoparticle superlattices and colloidal crystals is well on its way to becoming an industry. To attain such a status, however, requires that targeted crystal structures can be assembled with high quality and yield from inexpensive, easy-to-make building blocks. Great strides in this direction have been made recently using DNA-programmable assembly[43, 44, 45, 46]. At the same time, entropically-stabilized superlattices of extraordinary complexity have been predicted[31, 47, 25, 24] and, occasionally, observed by exploiting particle shape [48, 16, 17]. Although our understanding of the relationship between particle shape and crystal structure is quickly advancing, it is still not possible to predict *a priori* the crystals that will form from any arbitrary set of building blocks, nor the complementary prediction of the set of building blocks that will best assemble a given target structure. This latter challenge is the focus of the present paper.

Here we approach the challenge of building block design via symmetry principles and entropic degeneracies. Despite recent advances in our understanding of the thermodynamics of hard particle systems [49, 30], little is known about the relationship, if any, between the symmetries of particles and the assemblies they form. In contrast, symmetry principles in atomic crystals state that (i) the arrangement of atoms tends towards the highest possible symmetry, and (ii) counteracting factors due to special properties of the atoms may prevent attainment of the highest possible symmetry[50]. It has been observed in recent papers that these symmetry "rules" also apply for hard particles. Structures of high sym-

metry are stabilized by entropy because such structures provide identical local environments for each particle, thereby maximizing the average free volume per particle and, thus, the system entropy (E.g. FCC and BCC are assembled by 41% of the polyhedra in Damasceno et al. [24]. The "counteracting factors" that result in more complex structures come from pronounced shape anisotropies). Locally, however, entropy favors disorder and asymmetry, and in clusters, symmetry factors in the rotational partition function can destabilize highly symmetric clusters of spheres in favor of clusters of lower symmetry, as shown recently for clusters of micron-sized PMMA spheres [51]. This competition between local and global preferred symmetries makes building block design difficult when short range interactions, or simply entropic interactions, are considered.

We do, however, have some predictive knowledge of the assembly behavior of hard particles based on shape parameters like the isoperimetric quotient ($IQ = \frac{36\pi V^2}{A^3}$), which quantifies the roundness of a particle, and the average coordination number of the dense fluid, which correlates with the number of large facets [24]. Recent work by van Anders, et al[52, 22] further quantifies the entropic valence associated with particle shape that explains the tendency for faceted particles to adopt face-to-face configurations, as observed in many studies[53, 24, 31, 54] . Facets can act as emergent attractive "entropic patches"[22] with strengths of several $k_B T$ at moderate pressures around the crystallization transition. At infinite pressure, the assembly problem becomes a packing problem; however, the relationship between the two problems remains an open question [55, 56, 57, 58, 24, 59]. Particles may assemble thermodynamically stable or metastable crystals away from infinite pressure that

are less dense than, but identical in structure to, that in which the shape packs most densely [25]. Conversely, particles may assemble different crystal structures unrelated to the densest packings, which become stable only at much higher pressures. For example, cubes readily self-assemble a cubic crystal[29] and spheres an FCC crystal at densities near $\phi_p = 0.5$, both of which also correspond to those shapes' respective densest packings. In contrast, tetrahedra self-assemble a quasicrystal at a $\phi_p \approx 0.50$ [31], not the densest packing (a dimer crystal[35, 57], which is not thermodynamically stable until $\phi_p = 0.847$ [28]).

In this work, we propose and test a design strategy based on construction of particles whose shapes are given by the Voronoi tessellation of a target crystal structure, where the centers of the Voronoi cells represent the centers of the particles. By construction, these "Voronoi particles" (VPs) are space-filling, and in the infinite pressure limit pack so that their centers reproduce the original target structure.

2.2 Background and approach

Previous studies of the thermodynamics of space-filling shapes have been limited to the most symmetric sets of polyhedra. In Agarwal and Escobedo [25], the melting (as opposed to assembly) behavior of six crystals of space-filling shapes was studied. In John et al. [60] the phase diagram of space filling tetragonal parallelepipeds was determined via melting studies. In Khadilkar and Escobedo [61], the assembly behavior of three different binary mixtures of binary space-filling polyhedra were studied, and it was reported that the space-filling crystals could be assembled only through the introduction of enthalpic patches. In

this work, we investigate a large set of space-filling polyhedra in order to observe trends and correlations with particle shape.

Like the construction of (often highly idealized) pair potentials guaranteed to produce the corresponding ideal crystal in the limit of zero temperature [62, 63], Voronoi particles are ideal shapes guaranteed to produce the target structure in the limit of zero pressure. In order for a VP to assemble its target structure, facets of the VP must "bond" selectively via entropy. Facets are known to produce directional entropic forces[22] that promote effective bonding upon crowding, thus we expect the facets to promote the assembly of the space-filling structure. As in the case of pair potentials, which may or may not produce the target structure at finite temperatures due to entropic effects, our shapes may not assemble the target structure away from infinite pressure, again due to entropy (we find nonselective bonding and packing degeneracies play an important role in our systems).

Our goal here is to understand under which conditions VPs will assemble their target structure, under which conditions they do not and develop strategies for design based on our findings. We evaluate our strategy by selecting 46 crystal structures whose Voronoi tessellations contain a single Wyckoff position and thus yield a single type of particle shape, and we conduct assembly simulations using Monte Carlo methods. We show that the majority (72%) of the VPs studied self-assemble an ordered structure, but only the simplest structures with the most symmetric VPs assemble their space filling, target structures at moderate densities. We show how particle asymmetries can thermodynamically stabilize non-space-filling structures due to orientational and occupational packing degeneracies, and

support our results with free energy calculations for the specific case of the hexagonal diamond structure assembled from its VP. To improve the utility of Voronoi particles, we demonstrate entropic assembly strategies (shape modification and field-directed assembly) that can successfully assemble target structures.

2.3 Results

Our results are presented as follows. We begin with the findings from the assembly simulations of the VP for all 46 target structures. We identify metrics that allow us to correlate the assembly propensity of each target structure with particle shape. To elucidate the role of particle symmetry and orientational entropic degeneracies, we present a detailed study of the hexagonal diamond VP. We comment on multi-component VP systems, showing an example of occupationally degenerate crystal. Finally, we use our results to modify selected VPs and their assembly pathways to promote assembly of target structures not achievable without modification.

2.3.1 General findings

We classify the VPs into three categories: VP that self-assembled into (i) their target structure (Table 2.1, (ii) an ordered structure that was not the target structure (Table 2.2), and (iii) no ordered structure on the timescale of our simulations (Table 2.5). In Figure 2.2a), we show a scatter plot of the rotation group symmetry (N_{ROT}) of the VP against the size of the crystal basis (N_B) that generated the VP. Because these metrics are discrete, several

VP map onto the same point; pie charts are drawn in these locations. Images on this plot correspond to the VPs and structures listed in Tables 2.1, 2.2 and 2.5.

From Figure 2.2a), we see that the highest symmetry VP, corresponding to the simplest structures ($N_B \leq 2$), are the most likely to assemble their space-filling structure at finite packing fractions. We find the VP of the FCC, BCC, cubic, body-centered tetragonal, hexagonal, HCP, diamond and β -Sn successfully assembled their target structure. Degenerate, dense local packings or "bonded" states that are incompatible with the assembly of space filling structures are a detriment to assembly propensity. The symmetry of the particle is anti-correlated with this quantity; the more symmetric the particle, the fewer unique ways it can be placed next to a neighbor. This trend is reflected in Figure 2.2a.

As crystal structures become more complex, crystal symmetries are broken; this is reflected in the negative correlation between VP symmetry and the basis size. For crystal structures of moderate complexity, we find many VP that assemble into structures other than their space filling, target structures. Particles with very low symmetry, generated by crystal structures with the largest bases, tended to be poor assemblers; these particles were the most "rock-like" (low symmetry and many different types of large facets, $N_{f \geq \mu}$).

Most of the crystallizing particles self-assembled into orientationally degenerate, rather than space-filling structures. An orientationally degenerate diamond crystal (ODD) assembled by the hexagonal diamond VP is shown in Figure 2.3. Several additional examples are shown in Figure 2.4: the VPs of γ -Se, monoclinic, CuTi_3 , and A14 VP assemble 12, 6, 3 and 8 fold degenerate crystals, respectively. The tetragonal parallelepiped (VP of

the orthorhombic lattice) also assembled into phases with a six-fold orientational degeneracy called a parquet phase [60]. Although the crystalline packing is argued from melting studies to be the thermodynamically preferred state for parallelepipeds above $\phi_p \approx 0.7$ [60], we find only columnar and parquet phases to be accessible by assembly from the fluid phase. We also observed the high pressure lithium VP order into a BCC lattice with no orientational order until it has passed its rotational jamming point (rotational dynamics arrest, as discussed for the VP of the hexagonal diamond structure in the following section).

In Figure 2.2b, we examine assembly behavior as a function of $N_{f \geq \mu}$, the number of large facets and $N_{f, \max}$, the multiplicity of the largest facet (see Methods), with the same color scheme as Figure 2.2a. From this figure we see that the particles that assemble their target structures have primarily one type of large facet, and the shape has many copies of this largest facet. Particles with many types of facets ($N_{f \geq \mu}$) suffer from non-selectivity of entropic bonds. Some particles with several such facets (higher symmetry, large $N_{f, \max}$) still crystallize, while particles with too many competing facets (large $N_{f \geq \mu}$) with small multiplicity ($N_{f, \max}$) are poor assemblers.

2.3.2 An example: hexagonal diamond Voronoi particle

The results above demonstrate that orientational degeneracies are capable of stabilizing non-space filling crystals. As an example, we consider the assembly behavior of the VP for the hexagonal diamond (HD, Wurzite) structure. This VP (C_{3v}) is a representative example of one that assembles a crystal other than its target structure (blue in Figure 2.2). This

particle shape has low symmetry (Figure 2.2a), and assembles a four-fold, orientationally degenerate diamond crystal (ODD) instead of HD. To account for the entropic contribution of the 4^N -fold degeneracy of the ODD structure, we shift the free energy by $-\ln(4)Nk_B T$ relative to the HD as discussed in Methods and in Appendix A.

ODD is related to HD as FCC is related to HCP; HD consists of tetrahedrally close-packed (TCP) layers with an AB stacking. Figure 2.3a shows a HD VP with its faces colored by facet shape. The VP is a truncated tetrahedron with three augmented tips, and thus the particle has a three-fold rotation axis. There are two large facet types (red, cyan). In the target structure (2.3c, top 3 layers), red facets are adjacent to one another and cyan facets are adjacent to one another; the particles pack in tetrahedrally close-packed layers. The bottom three layers of Figure 2.3c highlight the AB stacking.

At the onset of order ($\phi_p = 0.59$) we did not observe the selective red-red, cyan-cyan bonding of the HD structure. Instead, the VPs assembled TCP layers that stack in an ABC pattern (Figure 2.3b, bottom three layers) to assemble the ODD structure. The VPs bond non-selectively in this crystal structure (Figure 2.3b, top 3 layers). The VPs exhibit a four-fold orientational degeneracy at each lattice site.

In NVT simulations in which we initialize the system in a perfect HD crystal, we observed HD VP losing their orientational order at packing fractions around $\phi_p = 0.59$. In fluid-HD coexistence simulations, we observed the thermodynamic phase transition from HD to ODD, confirming that ODD is the thermodynamically stable structure at these packing fractions, rather than HD or any structure with stacking faults (Figure 2.7). In coexistence

simulations of HD and ODD phases, we observed HD losing orientational order, but the stacking of the TCP layers remained unchanged; the free energy penalty of a stacking fault is very low in these systems (Figure 2.8).

In both the HD and ODD structures, each VP is tetrahedrally coordinated; thus we expect the free volume of these two structures to be nearly identical at packing fractions just above the onset of order ($\phi_p = 0.59$). This suggests that ODD is stabilized solely by the free energy associated with the orientational degeneracy. Our calculations (Figure 2.3d) confirm this and we find that the orientational degeneracy stabilizes the ODD up to $\phi_p = 0.77$. Above $\phi_p = 0.77$, our free energy calculations predict that HD is the stable configuration until $\phi_p = 1.0$. We were unable to observe this crossover at $\phi_p = 0.77$ because at these high densities, the simulations (and likely experiments) become non-ergodic. Examination of the rotational dynamics of the hexagonal diamond VP near this crossover regime demonstrates this non-ergodicity, and justifies the explicit shifting of the ODD free energy curve. Figure 2.3e shows the rotational autocorrelation function ψ of the VPs in the HD phase. We observe that ψ at first decays and near $\phi_p = 0.67$, ψ plateaus to a constant value, indicating the dynamics have become frozen and the system non-ergodic.

To compare the magnitude of the thermodynamic driving force for crystallization into orientationally degenerate versus non-degenerate crystals, we note that in van Anders et al. [22]. The potential of mean force and torque (PMFT) is calculated for comparably truncated tetrahedra, which produces entropic bond strengths in ODD of $\approx 2.5k_B T$. Thus the entropic forces driving the assembly of the OD relative to the HDD ($\ln(4) = 1.4k_B T$)

are comparable to the emergent forces driving crystallization quantified by the PMFT. To stabilize HD over ODD at lower packing fractions would require additional interparticle interactions, as in Khadilkar and Escobedo [61], and the magnitude of the required interactions must overcome the entropy from orientational degeneracies. Figure 2.4 shows several other VPs that assemble orientationally degenerate structures, along with the magnitude of the free energy due to their degeneracies.

2.3.3 Beyond single component systems

Many crystals have two (or more) Wyckoff positions and thus generate two (or more) VP. Binary mixtures of hard particles may crystallize[64, 65], or phase separate[26]. We studied a limited set of two-VP target structures to provide examples of VP phase behavior unique to multi-component VP systems. We did not observe any shape mixtures that crystallized into their space-filling structure: we observed phase separation (in VPs of the PtS crystal), observed mixtures that did not crystallize on the timescale of our simulation and observed several that crystallized into a non-space filling crystal.

The VPs generated by the trigonal- ω crystal (Figure 2.5 a-g) crystalize into an occupationally and orientationally degenerate, non-space-filling crystal. The VPs corresponding the Zn and Nb atomic sites of the trigonal- ω crystal assembled into a BCC crystal in which the type of VP at each lattice site is random. This mixing entropy can be thought of in same manner as orientational degeneracy can be for single-component systems, with the exception that this form of degeneracy entropy can only occur in multi-component systems.

We consider, as in the case of orientationally degenerate crystals, the first-order contributions to free energy, we now have three terms: rattling free energy, orientational degeneracy and now an occupational degeneracy term equivalent to a lattice gas mixing entropy term. For a binary mixture of species fraction of f and $1 - f$, this term has the form

$$F_{mixing} = Nk_B T (f \ln f + (1 - f) \ln(1 - f)) \quad (2.1)$$

and contributes $0.64k_B T$ toward stabilizing the occupationally degenerate crystal relative to the space-filling target structure for $f = 2/3$ (for trigonal- ω). We only observed occupationally degeneracy in structures with orientational degeneracy (trigonal- ω) or disorder (β -Mn).

The VPs generated by the PtS crystal (Figure 2.5 h-n) phase separate at $\phi_p = 0.57$, with the VP corresponding to the sulfur atoms crystallizing while the platinum VPs remain fluid. This phase separation is particularly notable because the particles have a densest packing as a co-crystal and thus at some pressure there must be a solid-solid transition from a demixed state to a mixed crystalline state. At low density, these particles are in a mixed fluid state; thus there is a re-entrant mixing transition in this system upon increasing pressure. Any VP mixture exhibiting phase separation exhibits this reentrant behavior.

2.3.4 Assembly engineering via mesoblock assembly

Having shown that competing degenerate dense packings may be stabilized relative to space-filling structures away from infinite pressure, we next modify particle shapes and, through the use of external fields, their assembly pathways so as to disfavor degenerate packings and successfully assemble both the hexagonal diamond target structure examined above, and a carbon 4-ring target crystal structure (Figure 2.6e). We consider two general strategies motivated by our findings. In the first strategy, we construct mesoblocks that increase the symmetry of the VPs, thereby reducing the number of degenerate dense packings. When this is insufficient, we consider a second strategy and couple the particle orientations to an external field. A third strategy, not considered here, is to introduce explicit interparticle forces, e.g. through the use of attractive ligands, to further disfavor competing packings, as explored for other particle shapes in Millan et al. [66], Khadilkar and Escobedo [61].

To illustrate the first strategy, consider the carbon 4-ring crystal structure [67]. The VP of this system has the point group D_2 , $IQ = 0.45$ and has two large facet types ($N_{f \geq \mu}$, see Table 2.5). Due to its low symmetry and expected frustrated bonding between its largest facets (Figure 2.6), we expect, and confirm, that this particle is a poor assembler - it does not order on the timescale of our simulations. To improve the assembly propensity into the target structure, we construct a two-particle and a four-particle mesoblock. The mesoblock comprising two VPs has C_{2v} symmetry and 2 large facet types – not much improvement over the VP. The mesoblock comprising four VPs is convex, and has D_{4h} symmetry and a single large facet type – attributes consistent with particles observed to assemble their space-filling

structure (Figure 2.6g). The latter mesoblock incorporates all particles in the primitive unit cell of the original target structure.

We performed assembly experiments for the VP and the two mesoblocks and found that only the four-VP mesoblock (the most symmetric one of the three shapes) assembles the space filling structure, consistent with our expectations (Figure 2.6) based on the findings in Figure 2.2. This observation suggests that to self assemble some structures, it may be beneficial to incorporate some of the structural complexity into the building block (in this case, four scattering centers) and assemble these higher-symmetry mesoblocks for which there are fewer packing degeneracies.

To illustrate the second strategy, consider again the VP of hexagonal diamond. We constructed a convex mesoblock (D_3) of two HD VPs (C_{3v}), and find that these particles do not assemble any ordered phase. These mesoblocks are identical in shape to the $t = \frac{2}{3}$ particles studied in Haji-Akbari et al. [68]. In that work, this shape was found to be on the boundary between a fluid region and one that crystallizes into the space-filling structure. However, the crystallization of this particle was reported to be exceptionally difficult, and indeed we were unable to assemble this mesoblock here. The reason assembly is difficult for this shape can be observed by calculations of the PMFT arising from competing local packings or "entropically bonded arrangements" as pictured in Figure 2.6c. However, if we disfavor these local packings with the application of an aligning external field (as described in the Methods), we indeed find its space-filling structure as low as $\phi = 0.56$, shown in Figure 2.6d. Experimentally, we imagine that such alignment could possibly be achieved via shear

flow.

2.3.5 Discussion

The role of orientational and occupational packing degeneracies in VP assembly can be understood by considering the contributions to the free energy for such systems. The free energy consists, to first order, of a term from "vibrational" or "rattling" motion of the particles and a term from the degeneracy of their local arrangement (this simple picture misses some collective effects). Revisiting the relationships between entropy and symmetry, we find that entropy can simultaneously favor symmetry and asymmetry. Globally, entropy favors symmetry; even in orientationally degenerate crystals, the environments of each particle are approximately the same. Vibrational entropy is maximized through the translational symmetry of the lattice. Locally, however, entropy still favors asymmetry. In the single VP systems studied here systems, local asymmetry takes the form of orientational degeneracies; the system exploits the asymmetry of the particles to maximize entropy. If particles are sufficiently symmetric, then the system cannot make orientational degenerate configurations that are consistent with the global ordering being driven by thermodynamic assembly. We can further interpret the behavior of many shapes that do not crystallize within this framework; in these cases the entropy of the local, asymmetric packings overwhelms the driving force to maximize vibrational entropy via ordering.

2.4 Conclusions

Using the Voronoi tessellation, we constructed a set of hard, polyhedral particles (Voronoi particles), whose space-filling configuration is isostructural to atomic crystals. At infinite pressure, the thermodynamic ground state of a VP system is guaranteed to be the space-filling structure. We find that at finite pressures, the most symmetric VP and with uniform faceting assemble their target structure. Many VP assemble non-space-filling, crystal structures and that are stabilized with respect to the target structure by orientational (and, in the multi-component systems occupational) degeneracies. Based on our findings, we show how VP can be modified to enhance selective entropic bonding and thus assembly, and how mesoblocks of fused VP can enhance assembly by increasing the particle symmetry and limiting the number of degenerate packings.

From this study, we learn the limits of engineering of assembly structure by modifying particle shape alone. By breaking particle symmetries we can thermodynamically stabilize arbitrary structures at infinite pressures. However, at finite pressures/packing fractions crystal structures with orientational degeneracy are stabilized by the additional entropy from the degeneracy. From an engineering standpoint, we must design particles so that this degeneracy does not make the desired structure unstable. This could be accomplished with enthalpic patches, designing shapes for which the rattling entropy in competing structures suffers in OD configurations, by constructing mesoblocks that incorporate structural complexity into the building block or by modifying the assembly environment by imposing

external potentials.

2.5 Model and methods

2.5.1 Voronoi particle construction

Construction of Voronoi particles via tessellation of target structures is performed as shown for the arsenic (As) crystal in Figure 2.1a-c. Starting with the target structure, we computed the Voronoi tessellation (Figure 2.1b), which associates each point in space with the closest lattice site. The Voronoi tessellation divides space into a set of convex polyhedra given a set of points. Around each point p , a polyhedral Voronoi cell is constructed that contains all points in space closer to a point p than any other point. If the set of points are periodic, like those in a crystal, the Voronoi cells are identical at each crystal site and equivalent to the Wigner-Seitz cell or the first Brillouin zone of the reciprocal lattice.

In atomic crystals, each facet of the Voronoi cell corresponds a nearest neighbor bond. Each type of bond (length and angle) corresponds to a facet of a different shape; if particles have identical bonds, their Voronoi cells will contain duplicate facets. In Figure 2.1b-c), the facets of the Voronoi tessellation are colored by shape to highlight the types of bonds present in the crystal structure. In a Voronoi tessellation, all facets are flush with identical facets of the Voronoi cells of adjacent crystal positions. The Voronoi cell at point p has the same point group symmetries as the Wyckoff position of point p .

The shape(s) of the resulting Voronoi cells provide the shape for the particles.

We placed 2000 hard VPs (choosing a number commensurate with self-assembling their space filling structure away from density 1) in a periodic simulation box in a disordered initial configuration, and then conducted equilibrium Monte Carlo simulations as described below. Figure 2.1c) shows the structure targeted by this self-assembly process for the As VP; Figure 2.1d shows a non-space-filling crystal structure resulting from MC simulation. Tables 2.1, 2.2 and 2.5 list the structures from which the VPs were generated along with properties of the corresponding Voronoi polyhedra.

2.5.2 Properties of Voronoi particles

There are many metrics with which one can characterize polyhedron. One may characterize the roundness of a polyhedron with the isoperimetric quotient (IQ)

Where V is the volume of the polyhedron and A is its surface area. Spheres have an $IQ = 1$, all other shapes have an $0 \leq IQ \leq 1$. Space-filling shapes are furthered constrained by the Kelvin conjecture, which states that the shape that can partition space in to equal volume components with minimal volume is the truncated octahedral (Voronoi cell of the BCC lattice). While more optimal equal volume but not identical tessellations have been found, the truncated octahedral is still believed to be the roundest, space filling shape, with an $IQ = 0.753$.

By selecting target crystal structures with a single Wyckoff position, we created space filling tilings that divide space into identical polyhedral subunits. The problem of dividing space into equal volume polyhedra with minimal surface area is the subject of the

Kelvin conjecture; the minimal surface area structure for *identical* subunits is conjectured to be the truncated octahedra, the Voronoi cell of the BCC lattice. This places an upper bound on the isoperimetric quotient of each VP at $IQ = \frac{36A^3}{V^2} = 0.754$. In Damasceno et al. [24], it is predicted that polyhedra with a higher IQ will assemble crystals without orientational order; the shapes in this study have IQs ranging from 0.262 to 0.754 , and thus are predicted to order into crystals with orientational and positional order.

The symmetry of a polyhedron can be quantified in a number of ways. For physical motivations, we choose to use the order of the rotation group, N_{ROT} . A polyhedron's rotation group contains all rotation operations that map it onto itself. The largest rotation group possible for a space-filling polyhedron is the O group, of order 24.

A polyhedron can be further characterized by looking at the distribution of its facets' areas and shapes. We define $N_{f \geq \mu}$ to be the number of types of unique facets greater than or equal to the mean facet size. We define $N_{f,max}$ to be the multiplicity of the largest facet. We note that both of these quantities are positively correlated with the N_{ROT} but not entirely determined by it. For example, a six fold rotational axis may be centered in a hexagonal facet, or it may pass through a vertex about which six identical facets come together.

Due to the nature of the Voronoi tessellation, nearest neighbor bonds in the target structure are mapped to facets on the particles. Each type of bond (length, angle, etc) is mapped to a unique shape of facet. In the space-filling configuration, identical facets on adjacent Voronoi cells are in contact. It has been observed that large facets seem to have the

most significant impact on assembly structures; $N_{f \geq \mu}$ characterizes the types of misbonding that can occur between particles and $N_{f, max}$ characterizes the number of ways correct bonds can be made.

2.5.3 Monte Carlo simulations of self-assembly

Monte Carlo simulations were carried out as described in Haji-Akbari et al. [31] using in-house code. For each target structure, we conducted NVT simulations in a triclinic box (using methods described in Damasceno et al. [24]), commensurate with the target structure. We ran simulations from $\phi_p = 0.53 - 0.63$. Below this range, polyhedra rarely order because the fluid is thermodynamically stable relative to the crystal. Above this region, simulations are often kinetically arrested because the densities are too high to see appreciable particle motion on the timescale of the simulations. We also conducted NPT simulations for each of the 46 shapes in which the box dimensions and angles can fluctuate. Those simulations were conducted at reduced pressures that correspond to the densities at which assemblies were observed in the NVT runs (P^* between 10 and 18, depending on particle shape). All simulations were run for a minimum of 40 million MC sweeps, with as many as 100 million sweeps for systems that did not assemble their space-filling structure. We simulated several different lattice parameters where appropriate (e.g. triclinic Bravais lattices).

2.5.4 Field-directed self-assembly

We conducted several field-directed self-assembly simulations of the hexagonal diamond mesoparticle. In these simulations, we place a director on the 3-fold rotation axis of each particle i , \hat{n}_i . An external potential is added to our Monte Carlo simulations of the form

$$U_{field} = \sum_{i=0}^N \gamma |\hat{n}_i - \hat{z}|^2 \quad (2.2)$$

where γ is a spring constant and \hat{z} is the direction of the aligning field. This potential is evaluated with $\gamma = 10$ and trial moves were accepted according to the Metropolis criterion with a temperature $T = 1$.

2.5.5 Structural identification

To identify the assembled structure, we look at the positions of points at the centroids of the Voronoi particles. We can compute bond order diagrams and diffraction patterns, and compare these to known structures. Bond order diagrams are a histogram of bond angles projected onto the surface of a sphere; stereographic projections of the BODs are shown beside simulation snapshots (e.g., in Figure 2.4) to show the crystal structure. We say a particle self-assembles its space-filling structure if it can be compressed to a space-filling configuration by scaling their positions.

2.5.6 Free energy calculations

In select cases, we assessed the relative thermodynamic stability of the orientationally degenerate assembly structures and target, space-filling structures of VP. We computed the free energy difference between a hard particle crystal and an Einstein crystal using Frenkel Ladd thermodynamic integration as described in Haji-Akbari et al. [28]. Einstein crystal coordinates and orientations $\{\vec{r}_0\}$ and $\{\vec{q}_0\}$ for the target structures were computed directly from the perfect, space-filling tessellations.

Computing the coordinates of the Einstein crystal for the orientationally degenerate structure required additional care. Orientationally degenerate crystals have long-range translational order, but the orientation of each particle at each lattice site can be in one of N_{OD} orientations. While the environment of each particle is approximately identical, we found that generating OD crystal coordinates using the perfect crystal coordinates and rotations produced configurations with high local densities (e.g. corners of shapes nearly overlapping) that cause the thermodynamic integration to diverge.

To initialize an orientationally degenerate Einstein crystal, we take $\{\vec{r}_0\}$ from the assembly's perfect crystal structure and compute a set of N_{OD} -fold degenerate orientations observed in the assembly structure $\{\vec{q}_0\}$. We assume the structure is non-ergodic in the region near the thermodynamic transition to the space-filling structure. Each particle is then assigned an orientation at random from $\{\vec{q}_0\}$. At the high densities required to observe the order-order phase transitions, this procedure created locally dense regions that caused the Frenkel Ladd integration to diverge if exact values of $\{\vec{q}_{eq}\}$ were used. Instead, we generated

orientationally degenerate configurations at $\phi_p = 0.5$ and compressed to the densest possible packing fraction while performing small MC rotations. Once compacted, $\{\vec{r}_0\}$ were scaled to create the desired density. We verified that the results of our calculations do not depend on the particular instance of the orientationally degenerate crystal. In orientationally degenerate structures, there are N_{OD} orientations for each particle in which the vibrational free energy from translation and rotation is roughly equivalent. To account for this additional entropy, we shift the free energy of the OD structure by $-\ln(N_{OD})k_B T$ per particle. Similar shifts have been employed in free energy calculations of degenerate dimer crystals[69].

2.5.7 Calculation of VP orientational correlation function

We initialized a perfect hexagonal diamond (HD) crystal, placed a director on the largest facet and 3-fold rotation axis of the HD VP, and computed the rotational autocorrelation function of this vector over a minimum of 40×10^6 Monte Carlo sweeps for packing fractions between $\phi = 0.54 - 0.80$. We define the orientational correlation function as

$$\psi(t) = \langle \hat{n}(t)\hat{n}(0) \rangle \tag{2.3}$$

where \hat{n} is the particle director. A system for which the director remains parallel to its original orientation will have $\psi = 1$. A system for which the $\hat{n}(t)$ is uniformly distributed around the unit sphere, $\psi = 0$. We also note that in a system for which $\hat{n}(t)$ averaged time trajectory has tetrahedral symmetry, and $\hat{n}(0)$ intersects a three-fold rotation axis, $\psi = 0$. This is the case in the orientationally degenerate diamond crystal.

2.5.8 Coexistence simulations of hexagonal diamond VPs

Here, we report the results from coexistence simulations of the HD VP. In order to verify that the orientationally degenerate diamond (ODD) structure is the thermodynamically stable structure at the onset of crystallization. As shown in Figure 2.7, we initialize a system with half of the system in HD and half of the system as a disordered fluid at packing fractions $\phi = 0.54 - 0.60$ and run 25 million MC sweeps. We find that even when seeded with the HD structure the fluid crystallizes into ODD. For $\phi = 0.54 - 0.55$ we observe a melting of the HDD structure into the fluid and a recrystallization into ODD.

Figure 2.8 reports coexistence simulations of the ODD and HDD structures. We initialize a system with half of the system in HD and half the system in ODD at packing fractions from $\phi = 0.57 - 0.60$ and run for 25 million MC sweeps. We do not observe a solid-solid transition from HD to ODD; instead the HD phase becomes orientationally degenerate (see Figure 2.8d). This ODHD can be interpreted as an ODD phase with low-free energy stacking faults. We note the the ODD structure does not melt until below $\phi = 0.57$ due to hysteresis surrounding the phase transition.

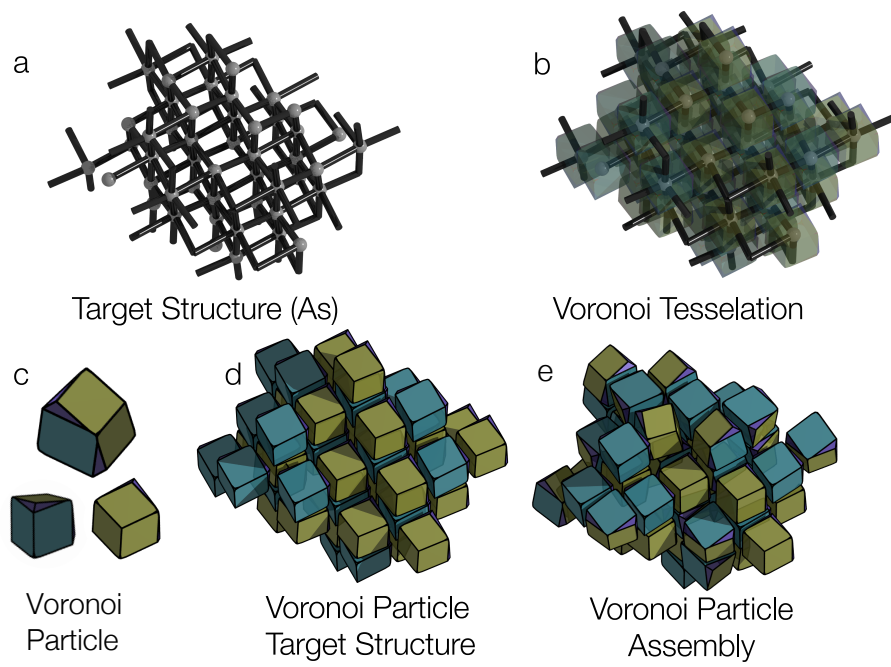


Figure 2.1: a) An example target crystal (arsenic). b), Computed Voronoi tessellation. c), Hexagonal diamond Voronoi particle from several views. d) Voronoi particles in their space-filling, target structure. e) Resulting equilibrium assembly from MC simulation.

Table 2.1: Table of Voronoi polyhedra that self assemble their space-filling structure









Number	Target Crystal	Image	Rotation Group	N_b	$N_{f \geq \mu}$	$N_{f, max}$	IQ
1	BCC		O_h	1	1	8	0.7530
2	β -Sn		D_{2d}	2	2	4	0.6515
3	Cubic		O_h	1	1	6	0.5240
4	Diamond		T	2	1	4	0.4617
5	FCC		O_h	1	1	12	0.7400
6	HCP		D_{3h}	2	2	6	0.7405
7	Hexagonal, $a = 1, c = 1$		D_{6h}	1	1	2	0.6046
8	Tetragonal BC $a = b = 1,$ $c = 2$		D_{4h}	1	1	4	0.6989

Table 2.2: Table of Voronoi polyhedra that self assemble a non-space-filling crystal instead of their target crystal






Number	Target Crystal	Assembled Crystal	Image	Rotation Group	N_B	$N_{f \geq \mu}$	$N_{f, max}$	IQ
9	A14	8-fold OD FCT		C_S	4	3	1	0.6828
10	As	6-fold OD Cubic		C_{3v}	2	2	3	0.5559
11	CuTi ₃	3-fold OD FCC		D_{4h}	4	1	8	0.7461
12	I ₂	12-fold OD BCC		C_{2v}	4	3	1	0.6828
13	Li cI16	Rotator BCC		C_3	8	3	3	0.7135
14	γ -Pu	12-fold OD FCC		D_2	2	3	4	0.7460
15	γ -Se	12-fold OD cubic		C_2	3	2	2	0.5745
16	Hexagonal $a = 1, c = 2$	Parquet (hexagonal coordination)		D_{6h}	1	1	6	0.5224
17	Hexagonal diamond	ODD Diamond		C_{3v}	4	2	1	0.4446

Table 2.3: Table 2.2, cont. (1)









Number	Target Crystal	Assembled Crystal	Image	Rotation Group	N_B	$N_{f \geq \mu}$	$N_{f, max}$	IQ
18	monoclinic $\alpha = 75^\circ$	6-fold OD Cubic		D_{2h}	1	2	2	0.5797
19	Base-centered monoclinic $\alpha = 85^\circ$	6-fold OD base-centered monoclinic		D_{1d}	1	3	4	0.6844
20	Base-centered Orthorhombic $a = 1, b = 2,$ $c = 4$	3-fold OD hexagonal		D_{2h}	2	1	2	0.4886
21	Face-centered Orthorhombic $a = 1, b = 2,$ $c = 4$	3-fold OD hexagonal		D_{2h}	1	2	2	0.5756
22	Body- centered Orthorhombic $a = 1, b = 2,$ $c = 4$	3-fold OD hexagonal		D_{2h}	1	2	2	0.5274
23	Tetragonal $a = b = 1,$ $c = 2$	Parquet		D_{4h}	1	1	4	0.4524
24	Tetragonal $a = b = 1,$ $c = 4$	Parquet		D_{4h}	1	1	4	0.3103
25	Tetragonal $a = b = 2,$ $c = 1$	Parquet		D_{4h}	1	1	2	0.4418

Table 2.4: Table 2.2, cont. (2)

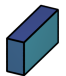




















Number	Target Crystal	Assembled Crystal	Image	Rotation Group	N_B	$N_{f \geq \mu}$	$N_{f, max}$	IQ
26	Orthorhombic $a = 1, b = 2,$ $c = 4$	Parquet		D_{2h}	1	1	2	0.3297
27	Tetragonal $a = b = 4$ $c = 1$	Parquet		D_{4h}	1	1	2	0.2618
28	Body-centered Tetragonal $a = b = 1,$ $c = 4$	Parquet		D_{4h}	1	1	4	0.5079
29	Body-centered Tetragonal $a = b = 4,$ $c = 1$	Parquet		D_{4h}	1	1	2	0.3912
30	Rhombohedral $\alpha = 65^\circ,$ $\beta = 85^\circ$	3-fold OD sheared Hexagonal		S_2	1	4	2	0.5826
30	Rhombohedral $\alpha = 75^\circ,$ $\beta = 85^\circ$	3-fold OD sheared Hexagonal		S_2	1	4	2	0.6818
32	Rhombic Graphite	2-fold OD Honeycomb		C_{3v}	2	1	3	0.3654
33	Triclinic $\alpha = 65^\circ,$ $\beta = 85^\circ$	Parquet		S_2	1	3	2	0.5534
34	Triclinic $\alpha = 75^\circ,$ $\beta = 85^\circ$	Parquet		S_2	1	2	2	0.5553

Table 2.5: Table of Voronoi polyhedra that do not self assemble a crystal

Number	Target Crystal	Image	Rotation Group	N_B	$N_{f \geq \mu}$	$N_{f, max}$	IQ
35	Si bct5		C_{4v}	2	2	1	0.5372
36	SiBC8		C_3	8	3	3	0.5791
37	Te High Pressure		C_1	4	5	1	0.6954
38	α -Ga		C_s	4	4	1	0.5935
39	α -N ₂		C_3	8	1	1	0.6327
40	α -O ₂		C_s	2	4	1	0.6238
41	α -U		C_s	2	2	2	0.5867
42	β -O ₂		C_3	2	2	1	0.6176
43	black P		C_s	4	4	2	0.6321
44	carbon 3 ring		C_{2v}	6	2	2	0.3307
45	carbon 4 ring		C_{2v}	4	2	2	0.4134
46	γ -N ₂		C_{2v}	4	2	1	0.5858

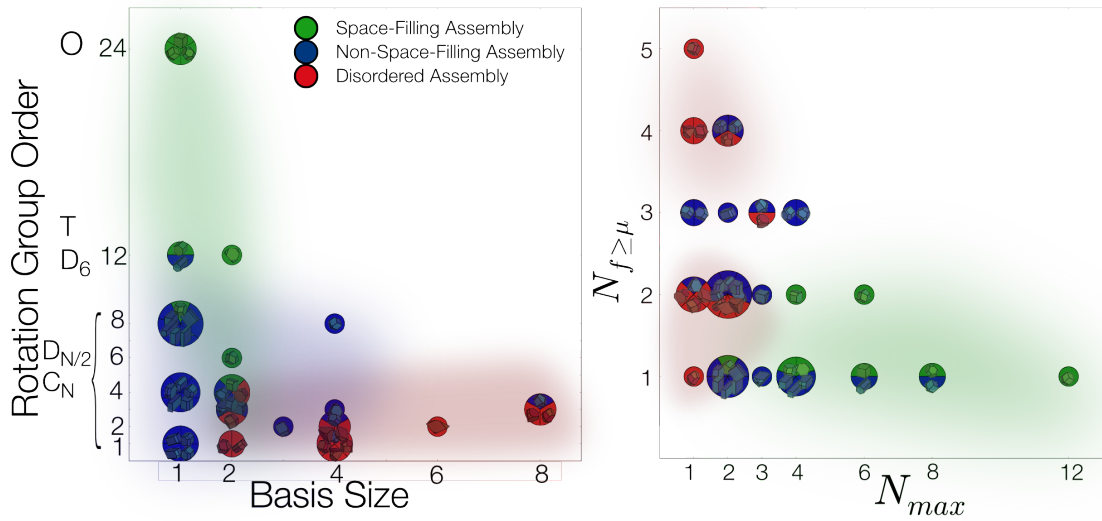


Figure 2.2: a) and b) Results from all single Voronoi particle assemblies. Green particles are VP that assemble their space filling structure (Table 2.1), blue particles are VP that form an ordered structure that is not space filling (Table 2.2), and red particles are VP that do not assemble an ordered structure (Table 2.5). Pie charts are placed where VP systems are mapped exactly onto the same parameters. a) Assembly behavior as a function of VP rotational symmetry and number of particles in the target structure’s primitive unit cell. b) Assembly behavior as a function of the number of large facet types with area greater than or equal to the mean facet area ($N_{f \geq \mu}$) versus the multiplicity of the largest facet (N_{max}).

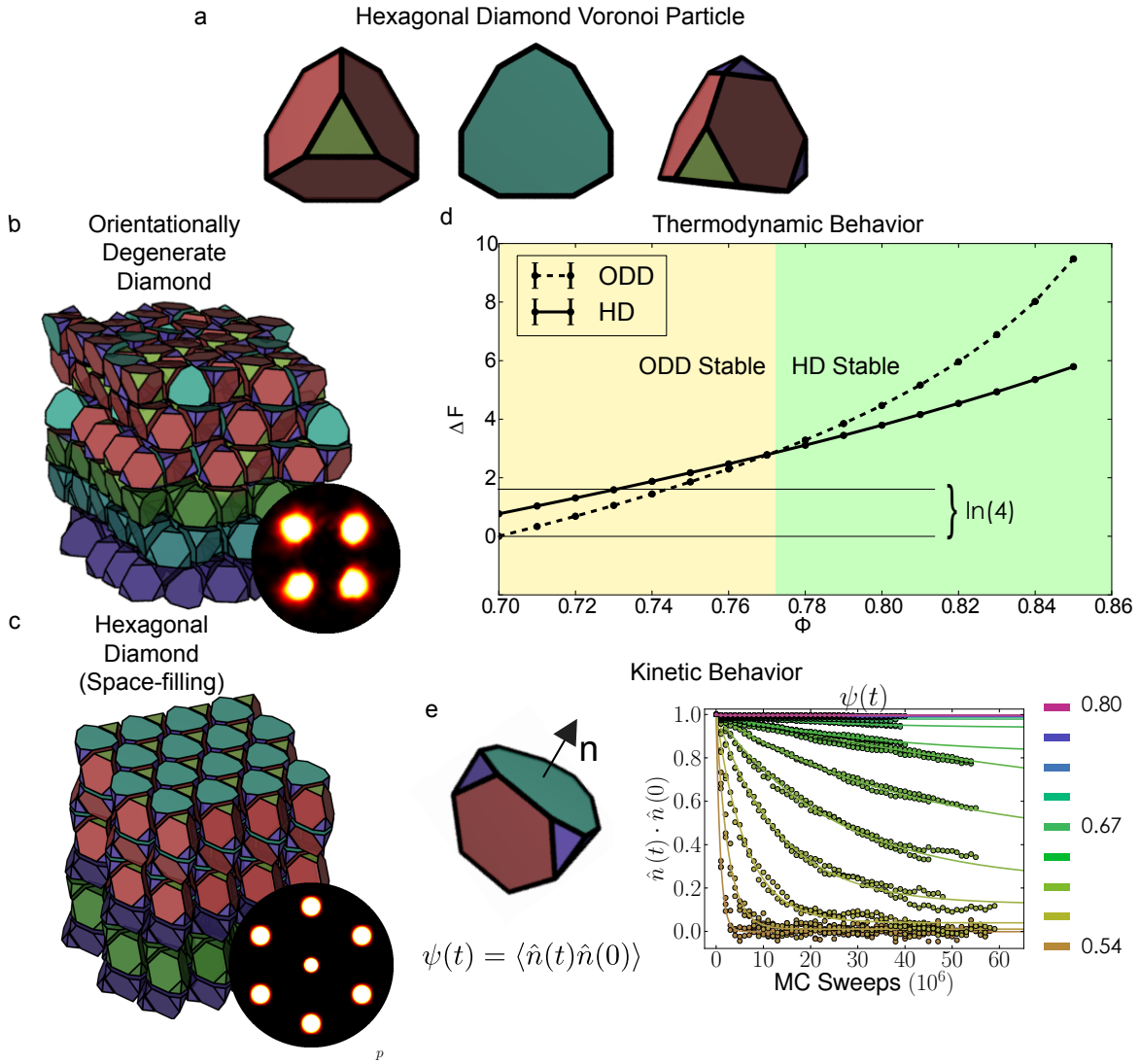


Figure 2.3: a) Colorized HD VP from several views. b) Assembly structure of the HD VP, orientationally degenerate diamond. This structure is composed of tetrahedrally closed packed layers in which the HD VP adopt one of four nominally equivalent orientations (shown in top three layers), and stack ABC (shown in bottom three layers). c) Space-filling target structure of the HD VP. The particles have no orientational degeneracy (shown in top three layers) and stack AB (shown in bottom three layers). d) Helmholtz free energy difference calculated between these two structures using the Frenkel-Ladd method. The orientational degeneracy stabilizes the non-space filling structure up to a $\phi_p = 0.77$. e) Orientational correlation function for packing fractions near the predicted thermodynamic transition. The HD VP is kinetically arrested before the thermodynamic ODD to HD phase transition.

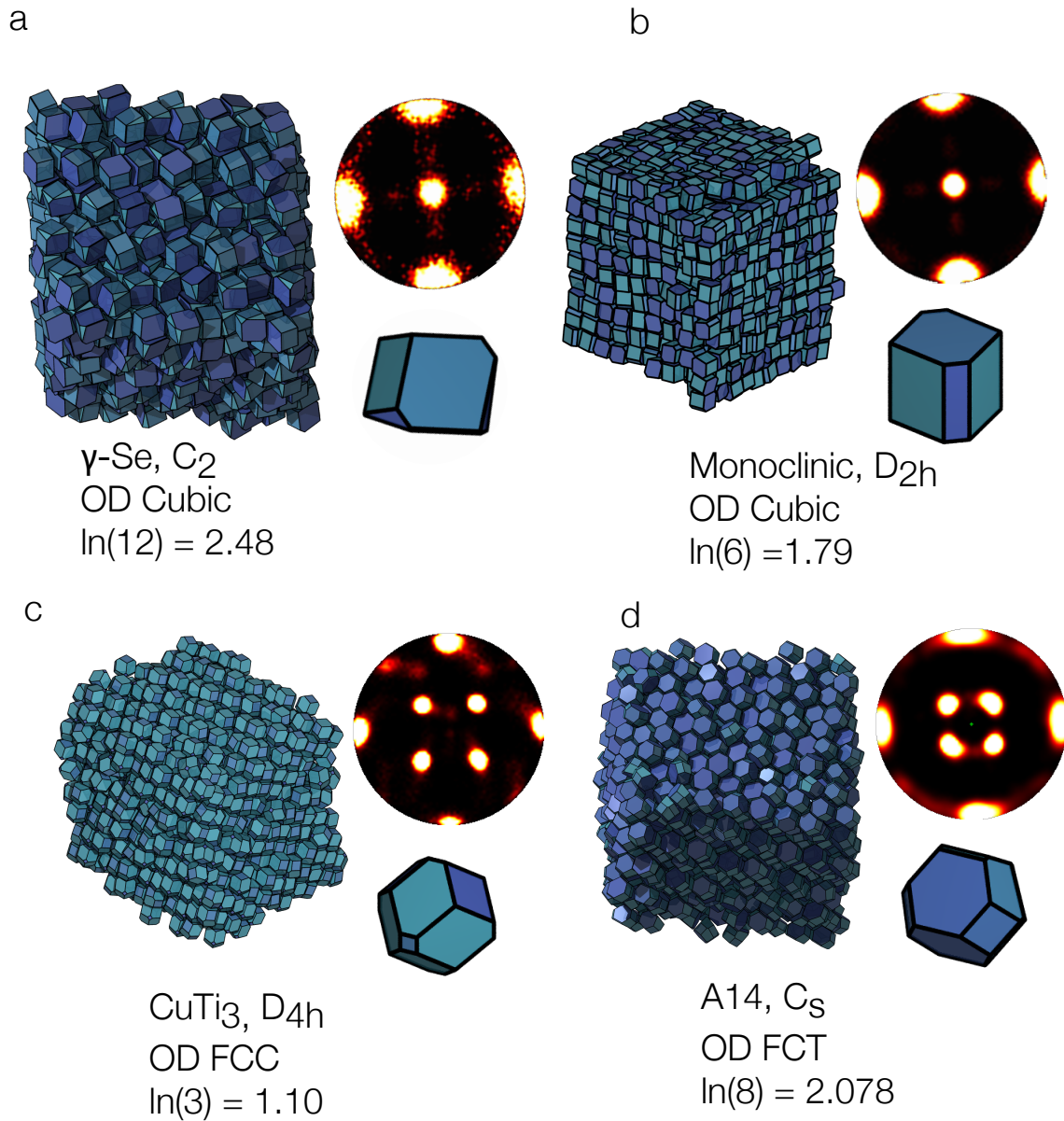


Figure 2.4: Simulation snapshots of four systems that do not assemble space-filling structures. They share the common feature that the crystals have full positional order and partial orientational order (orientationally degenerate). Under each snapshot, the name of the target structure is listed, followed by the point group of the Voronoi particle. The second line lists the assembled crystal. The third line lists the entropy per particle contributed to the stabilization of the orientationally degenerate structure relative to the space filling target structure.

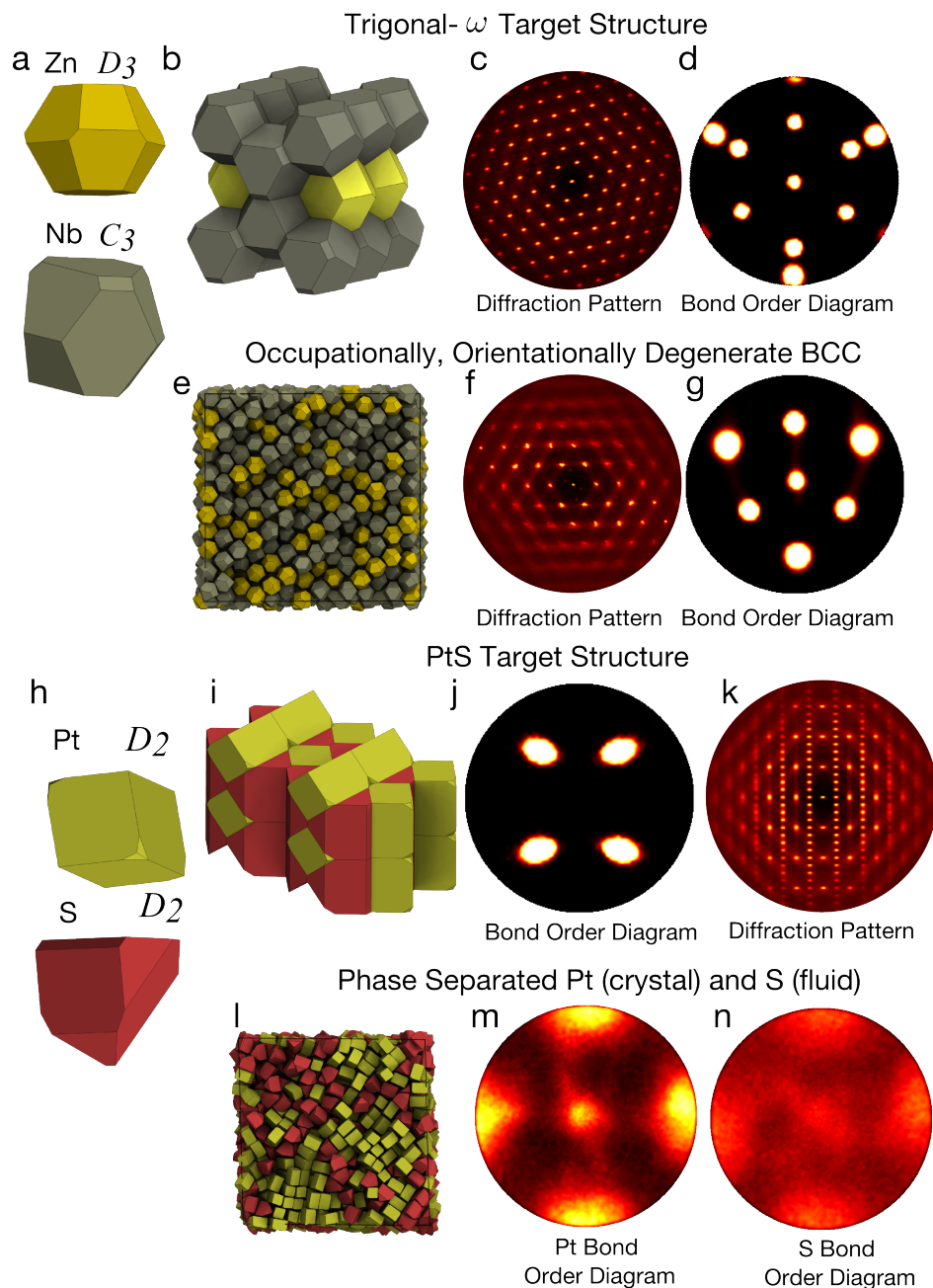


Figure 2.5: a) The two Voronoi particles generated by trigonal- ω (ZnNb_2) labelled by atom type. b-d) The target structure, its diffraction pattern and bond-order diagram respectively. e-f) The assembled structure (an occupationally degenerate BCC lattice), its diffraction pattern and bond-order diagram. h) The two Voronoi particles generated by PtS, labelled by atom type. i-k) The target structure, its bond-order diagram and its diffraction pattern respectively. l-n) The phase separated, assembly structure, the bond-order diagram of the Pt VPs and the bond-order diagram of the S VPs respectively.

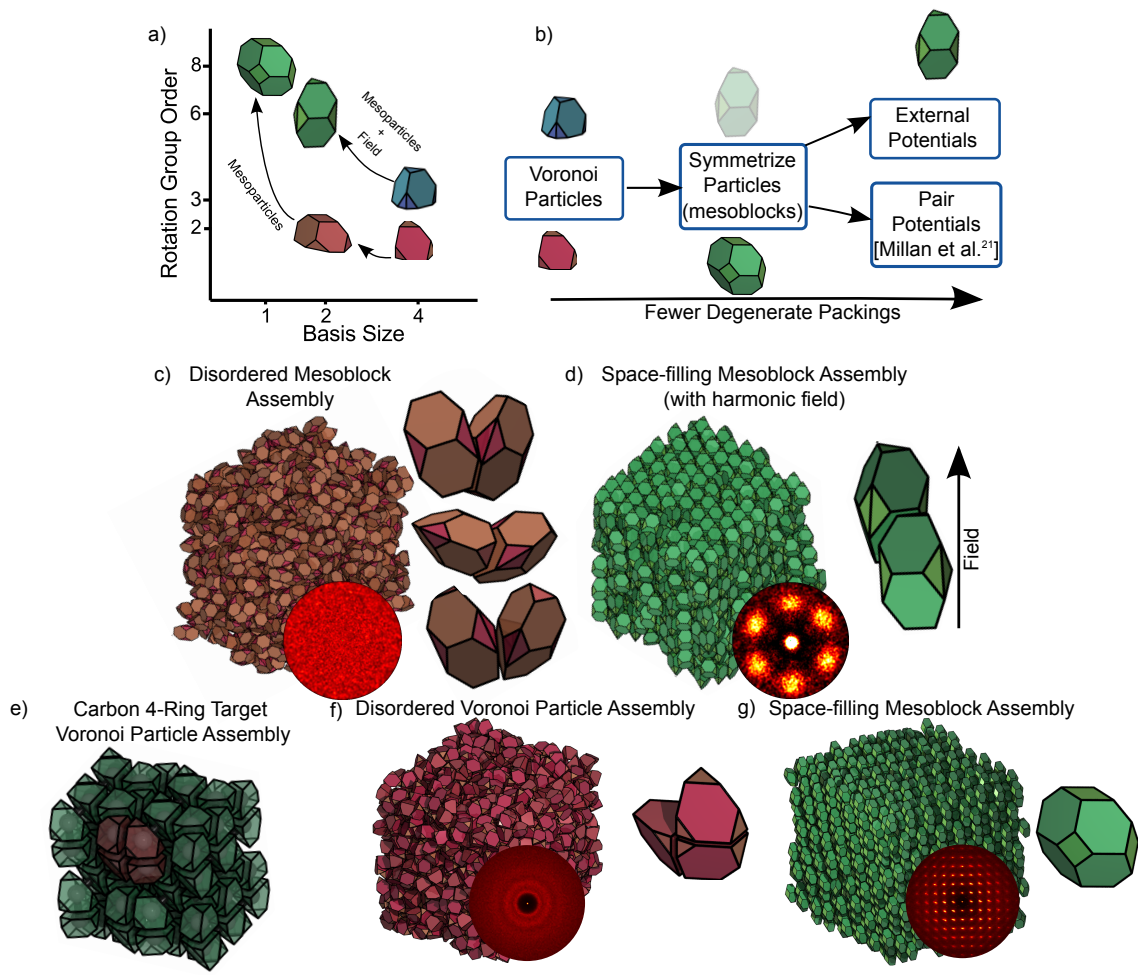


Figure 2.6: Two examples of engineering hard-particle building blocks using Voronoi particles as a basis for design. a) and b) Diagrammatic representations of our particle engineering. In a) representation of how constructing mesoblocks from Voronoi particle decrease the size of the effective basis and increases the symmetry of particles. In b) we outline how these assembly strategies reduce the number of degenerate packings that inhibit that assembly of space-filling structures. c) A first attempt to assemble the hexagonal diamond with a mesoparticle; although this mesoblock increases the symmetry of the basic particle, it also introduces several locally dense packings (shown on the right) that are inconsistent a crystal structure. d) An external field is introduced to disfavor these competing packings; this yields the assembly of the target space-filling structures. e) The Voronoi tessellation of the carbon 4-ring structure. The VP does not assemble the target structure (f), but by fusing several VP together, we can construct mesoblocks of higher symmetry that successfully assemble the target structure (g).

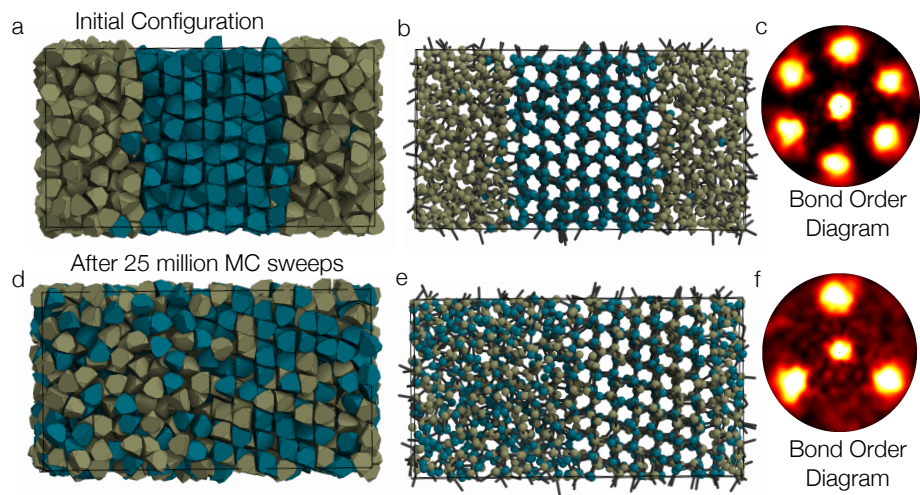


Figure 2.7: Phase coexistence simulations of HD VPs at $\phi = 0.54$. Particles initialized in the disordered phase are tan. Particles initialized in the HD phase are teal. a) Initial configuration. b) The particle centers and nearest neighbor bonds. c) Bond order diagram showing hexagonal order. d) The equilibrated configuration. e) Particle centers and bonds, showing the fluid and crystal regions. f) The tetrahedral order in the ODD crystal region.

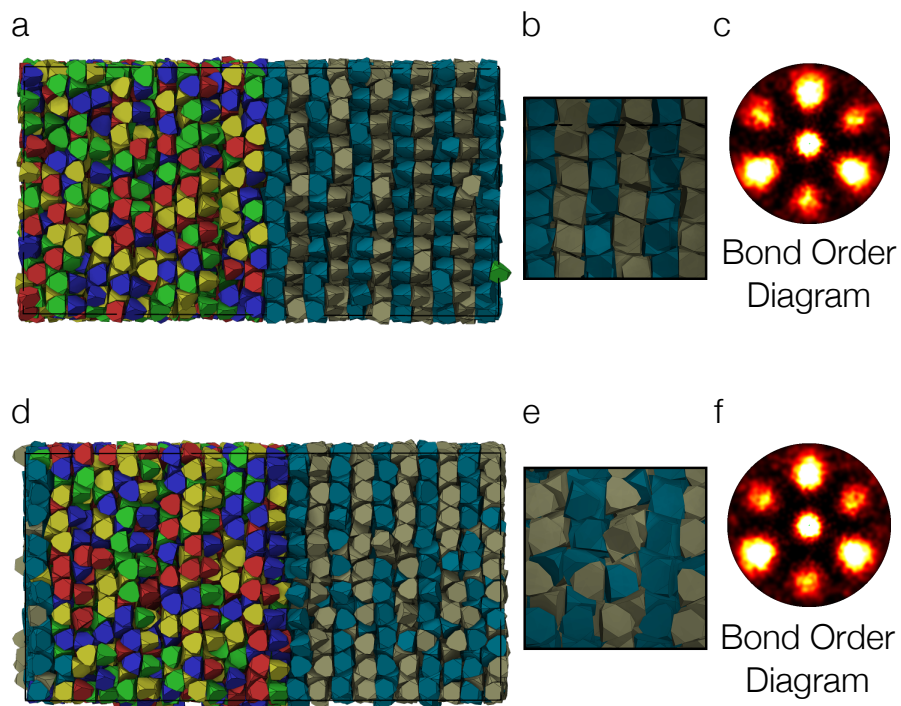


Figure 2.8: Phase coexistence simulations of HD VPs at $\phi = 0.59$. Particles initialized in the ODD phase are red, green, blue and yellow corresponding to their orientation. Particles initialized in the HD phase are teal and tan, according to their initial orientation. a) shows the initial configuration. b) shows a zoomed in section of the HD region. c) Bond order diagram showing a superposition of hexagonal order and tetrahedral order. d) shows the equilibrated configuration. e) shows a zoomed in section of the resulting ODHD region. Note the degenerate particle orientations. f) Bond order diagram showing the remaining superposition of hexagonal order and tetrahedral order.

Chapter 3

Image processing of confocal image volumes

This chapter reviews and describes a new method for the extraction of particle coordinates from three-dimensional image volumes, such as those attained by confocal microscopy. This method used to analyze confocal image volumes in chapter 4 and portions of this chapter are also included in the manuscript in preparation by co-authored with Lilian Hsiao, Jens Glaser, Michael Engel, Megan Szakasits, Sharon Glotzer and Michael Solomon.

3.1 3-dimensional images in self-assembly

One of the salient features of studying self-assembly and statistical mechanics at the colloidal scale is that the particles can be imaged with optical microscopes. In particular, colloidal particles in suspension can be density and index of refraction matched with the solution in

which they are suspended[34]. In this case, confocal laser-scanning microscopes (CLSM) can be used to capture full three-dimensional image volumes of the suspension by scanning the microscope’s focal plane through the sample (see Figure 3.1 for a schematic).

Once image volumes have been acquired, we wish to extract the coordinates of all particles in the volume for quantitative analysis. For spherical particles this procedure has existed for nearly two decades [34]; particle positions can also be linked together to compute per-particle trajectories. Once computed, these particle trajectories can be used for real space structure determination [70, 71] and to study defect dynamics [72], for example.

Recently, three-dimensional image volumes have become accessible to experimentalists working outside of the micron scale. Through tomographic reconstruction, millimeter scale (granular matter) experiments can be imaged with X-rays [73]. Nanoscale assembly experiments can be imaged using tomographic reconstructions of transmission electron micrographs [74]. These image volumes are not fundamentally different from those captured by a CLSM and the same fundamental image processing methods can be applied to all cases, though each microscopic technique has its own characteristic quirks.

3.2 Beyond monodisperse spheres

The image processing methods described in [34] have been extended in the past two decades to track particles in suspension beyond monodisperse spheres. The main difficulty in these more complicated cases is the particle identification; reconstructing particle trajectories can proceed in essentially the same manner for all particles. Particle identification is complicated

by extra degrees of freedom. Spherical particles may be polydisperse - Leocmach and Tanaka [75] developed methods for imaging polydisperse mixtures of spheres using a hierarchical difference-of-Gaussians approach that is capable of determining particle size and positions.

There are a number of methods that are designed for tracking anisotropic particles that have both translational and rotational degrees of freedom. For rod and prolate ellipsoidal particles, there exists methods for determining particle orientation from the the intensity backbone of the rod [76] which have recently been refined [77]. Elongated particles with surface anisotropy (breaking their cylindrical symmetry) can be identified by combined imaging of the reflection and fluorescence channels of the microscope (fluorescently tagged particles emit at a different wavelength than they are illuminated with) [78]. At the granular scale, there are several papers in which tetrahedral and ellipsoidal granular particles [79, 73] are imaged using methods based on the watershed cut, which has not been extensively applied to colloidal systems. Flexible, elongated objects have been identified and tracked using the Delanuay triangulation by Chen et al. [80].

While scientists have found success processing image volumes, most of the above methods rely on some particular assumptions about the system in order to identify particle positions and orientations. We seek a more general purpose approach and author an open-source software framework for extracting anisotropic particle coordinates.

3.3 A watershed segmentation approach to particle identification

The problem of detecting oblate colloidal spheroids (described in chapter 4) led us to consider particle detection methods that do not depend strongly on particle shape. This pursuit led us to select the watershed cut algorithm, which is a traditional method of image segmentation, as the work-horse of our algorithm. The work of [73] also employed the watershed cut while segmenting image volumes of granular systems; our work is the first to adapt this method to colloidal systems.

The watershed cut divides an image into catchment basins of local minima - pixels from which a steepest descent path leads to the same minimum are clustered together. The cut can be efficiently computed as described in Cousty et al. [81]; we summarize the algorithm here. We define our image I and an array containing basin labels ϕ . For each voxel, we launch a steepest descent path over the network of edges between voxels. The edges of this network are weighted by the difference between the intensity of voxels they connect ($\Delta I = I(i, j, k) - I(i', j', k')$); the steepest descent path is computed by traversing the network along maximally weighted edges until a minimum is reached. Once a putative minimum is reached (a voxel that is surrounded by voxels of equal or higher intensity), a breadth-first search is used to identify the full domain of the basin (minima are defined as sets of voxels that are surrounded by pixels of higher intensity). Once the identification of the minima is complete, all of the points visited along the descent path are given the same

label stored in ϕ . As this path is computed, the current label ϕ_0 is checked at each voxel; if any point has already been labelled, the process can be short-circuited and all points that are in the current path can be labelled ϕ_0 . This algorithm is inherently serial, however it still can be efficiently parallelized for images with small segments by taking steepest descent paths in different regions of the images and accessing ϕ with atomic operations.

The watershed cut method segments the image into bright regions; in confocal microscopy, fluorescent particles are bright regions separated by dark solution. Others have binarized the image volume and performed watershed cuts after performing an edge-distance transform [73]; we found this approach was not well suited for confocal images where particles where particle are usually poorly separated by a threshold. However, segmenting raw confocal image volumes leads to vast over-segmentation of the particles (Figure 3.2). Noise in image volumes can be suppressed with blurring; however in dense suspensions we found the amount of blurring required to suppress over segmentation resulted in under-segmentation as a result of loss of resolution.

This problem of over-segmentation can be overcome by pre-flooding the image as described in Figure 3.2. This algorithm requires the user to specify a depth δ by which to fill minima. Minima in the image are identified and the edges are searched for a lowest value. The extent of the minima is filled to match the minimum value of the edge. We then check the surrounding minima, checking if this minima has merged with adjacent minima, and the process is repeated until the minimum is no longer a minimum or has been filled to a depth δ . This process preserves more spatial resolution than blurring, but eliminates

many spurious minima that cause over-segmentation.

3.4 Position and orientation identification

Once the image segments are identified, we must compute their positions and orientations. For anisotropic particles (without tetrahedral symmetry) we can compute the covariance matrix M of the intensity of the segment and find the eigenvectors and eigenvalues to compute the orientation and size of the segment. First we compute the center of intensity \vec{r}_0

$$\vec{r}_0 = \frac{1}{I_{tot}} \sum_{\phi(ijk)=\phi_0} I(i, j, k) \vec{r}(i, j, k) \quad (3.1)$$

where ϕ_0 is the segment label of the current segment, $\vec{r}(i, j, k) = i\hat{x} + j\hat{y} + k\hat{z}$ and $I_{tot} = \sum_{\phi(ijk)=\phi_0} I(i, j, k)$. We then compute the covariance matrix about the center of intensity

$$\mathbf{M}_0 = \frac{1}{I_{tot}} \sum_{\phi(i,j,k)=\phi_0} I(i, j, k) (\vec{r}(i, j, k) - \vec{r}_0) \otimes (\vec{r}(i, j, k) - \vec{r}_0) \quad (3.2)$$

\mathbf{M} is closely related to the inertial tensor (if intensity instead represented mass). If we assume that ellipsoidal objects have an ellipsoidal Gaussian intensity profile

$$f(\vec{x}) = \exp((\vec{x} - \vec{x}_0)\mathbf{A}(\vec{x} - \vec{x}_0)) \quad (3.3)$$

with

$$\mathbf{A}^{-1} = \begin{pmatrix} a^2 & 0 & 0 \\ 0 & b^2 & 0 \\ 0 & 0 & c^2 \end{pmatrix}, \quad (3.4)$$

then \mathbf{M} can be computed analytically

$$\mathbf{M} = \begin{pmatrix} a^2/2 & 0 & 0 \\ 0 & b^2/2 & 0 \\ 0 & 0 & c^2/2 \end{pmatrix} \quad (3.5)$$

. Thus, \mathbf{M} and \mathbf{A}^{-1} are diagonal in the same basis and the associated eigenvalues of \mathbf{M} correspond to the extent of the ellipsoid. We comment that this feature is independent of the shape of the image segment; this approach can be used to determine the orientation of objects of any aspect ratio (Figure 3.6).

For the case of more symmetric bodies, the covariance matrix is proportional to the identity matrix. In the detection of such particles a numerical optimization must be performed to compute the orientation, as in Neudecker et al. [79]. We propose an efficient method that uses a spherical harmonic expansion of the segment intensity distribution.

First we compute the angular intensity distribution ψ

$$\psi(\theta, \phi) = \sum_{\Phi(i,j,k)=\Phi_0} I(i, j, k) (\vec{r}(i, j, k) - \vec{r}_0) \cdot \hat{r}(\theta, \phi). \quad (3.6)$$

We then compute the spherical harmonic expansion of ψ , and choose a value

of l that identifies a particle symmetry (e.g. $l = 4$ for tetrahedral symmetry,

$$\psi(\theta, \phi) = \sum_{m=-l}^l c_{lm} Y_l^m(\theta, \phi). \quad (3.7)$$

We also compute the coefficients of such an expansion for a reference particle for which we know the orientation, $\{c_{lm}^0\}$. Next, we perform a steepest descent optimization to minimize

$$\Delta = \sum_{m=-l}^l |c_{lm} - c_{lm}^0|. \quad (3.8)$$

The numerical derivatives in θ , ϕ and ψ (third Euler angle) can be calculated by applying rotation operations to the coefficients. For example, a rotation in ϕ of coefficient c_{lm} corresponds to a multiplication by $\exp(i\phi)$. Once this optimization is complete, the orientation is known from θ , ϕ , and ψ .

3.5 Implementation and verification

These processing filters, along with an efficient blurring and thresholding filters have been implemented in C++ and wrapped in a python interface that integrates with the standard numerical processing library, numpy. A similar set of filters is available in the the open source library scikit-image. Figure 3.3 compares the performance of this code and it is nearly twice as fast on a single core and nearly an order of magnitude factor faster on 4 cores. This

parallelized processing code could be run on even more cores and approach real-time particle identification - even at four cores, the entire image processing pipeline takes fewer than 20 seconds to process a $512 \times 512 \times 256$ image volume. This code is designed and documented so that the addition of filters written in C++ or python is straightforward. It will be available at <http://github.com/benjaminaschultz>.

A schematic of the entire processing pipeline is shown in Figure 3.5. Using the filters described in the previous section, our pipeline consists of the following steps. The original image volume is blurred by a Gaussian filter with a kernel of size $\sigma = 1$ pixel to smooth CCD noise. Next, we threshold the images, applying a global threshold τ_{global} and τ_{local} . Regions of image intensity $< \tau_{global}$ are set to 0. To compute the local threshold, a Gaussian blur of width $\sigma = 10$ pixels is applied to the original image I to produce $I_{background}$; pixels for which $I < \tau_{local} I_{background}$ are discarded. The image is then inverted.

The inverted image I_{inv} is then pre-flooded by a depth $d = 15$ and a watershed cut is performed. The mass and eccentricities of the segments are computed using the covariance matrix as described in the previous section. We define acceptable ranges of eccentricities $\epsilon_{0,min}$, $\epsilon_{0,max}$ and $\epsilon_{1,min}$, $\epsilon_{1,max}$ and of masses m_{min} , m_{max} . Segments that fall within these bounds are identified as particles. Regions that are smaller than m_{min} are merged with neighboring segments that are also undersized, and accepted as particles if they now fall within the bounds. Each basin is attempted to be merged with a single neighboring basin; the first merge that results in an acceptable particle is accepted. In regions for which $m \geq m_{max}$, the original image is pre-flooded by $d = 0.8 d_0$, then segmented and this

Number	Position (\parallel focal plane)	Position (\perp focal plane)	Position (total)	Orientation
$\pm 2\%$	$\pm 20\text{nm}$	$\pm 39\text{nm}$	$\pm 30\text{nm}$	$\pm 3.0^\circ$

Table 3.1: Standard deviations in particle number, positions and orientations from processing an arrested volume of oblate PMMA spheroids

procedure is repeated until $d = 1$ or no new particles are identified.

We verified the performance of this code using the intended experimental system of index of refraction and density matched oblate colloidal ellipsoids (described in chapter 4). An arrested sample of oblate spheroids was imaged in triplicate and processed as described above to identify particle position and orientation. The results of the variation in particle number, position and orientation are summarized in Table 3.1. We report a deviation in particle number of 2%, in particle position of 30nm and in particle orientation of 3°.

To further characterize the accuracy of this method, we generated two synthetic images volumes of ellipsoids at aspect ratios $\epsilon = \frac{1}{3}$ and 3 at a 30% volume fraction by replacing each particle with an ellipsoidal Gaussian. For each case, we process the image volume and compare the computed positions and orientations to the input values as we add noise. The results are shown in Figure 3.4.

3.6 Conclusions

The particle identification methods described in this chapter represent a novel approach to particle identification for anisotropic colloids in image volumes. The methods have been

efficiently and extensively implemented and verified. They are used to characterized the self-assembly of oblate ellipsoids in the following chapter. Moving forward, we seek to continue development, adding full support for particles with tetrahedral symmetry, additional filters and temporal tracking.

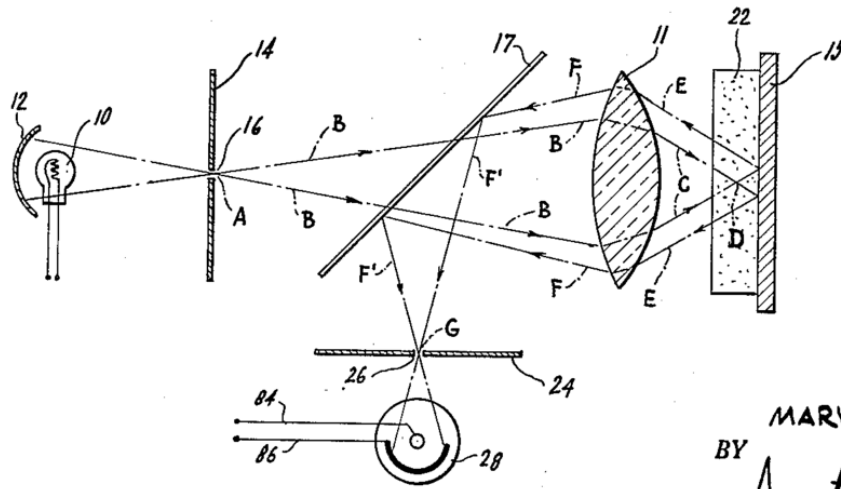


FIG. 3.

INVENTOR.
MARVIN MINSKY
 BY *Ameter & Levy*
 ATTORNEYS

Figure 3.1: Schematic of a confocal microscope. A light source (10) passes through an aperture (14), then beam splitter angle at 45° (17) and is focuses into the sample(11). A mirror (15) is placed at the focal plane, which the reflects light back to the beam-splitte (17) and is focused the the lens(11) onto a detector(28). In a laser-scanning microscope, the particles are fluoresce and a mirror is not placed at (15); instead, the particles fluoresce and the particles at the focal plain are imaged. Public Domain image from US Patent 3.013.467.

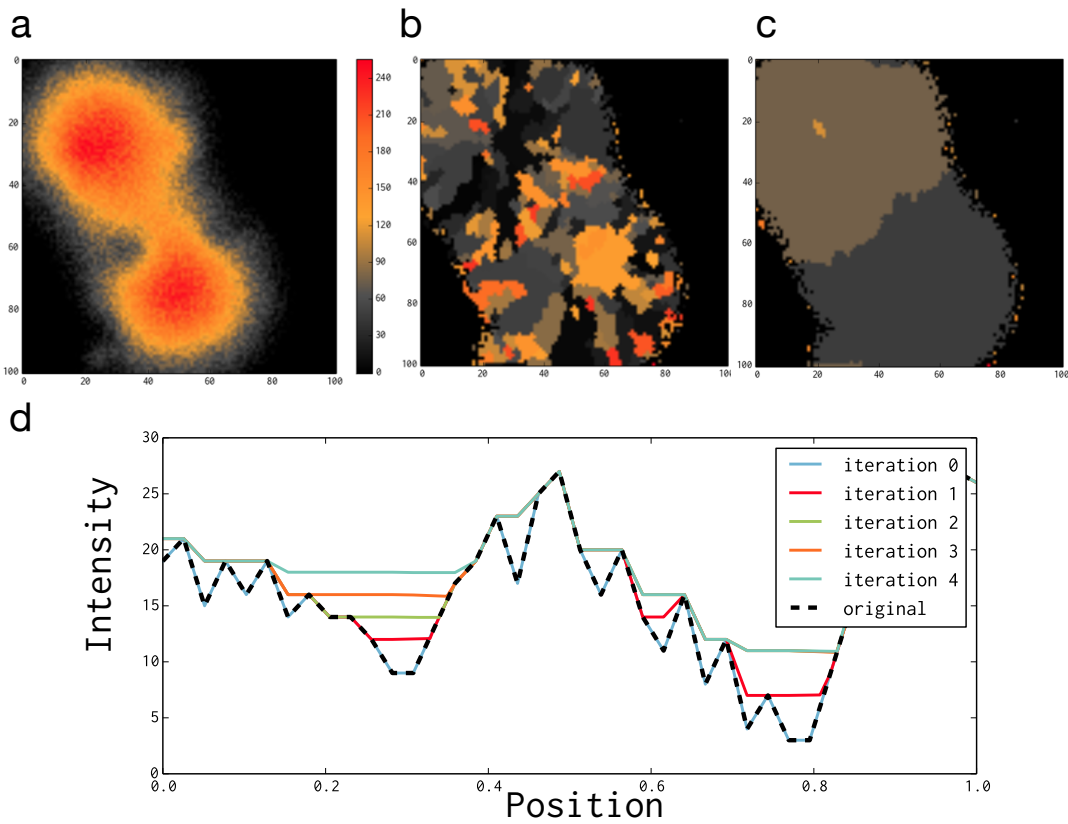


Figure 3.2: Example of the watershed cut with pre-flooding filter. 3.2a shows an example noisy image, with two particles. 3.2b shows a watershed cut performed with no pre-flooding, colored randomly by segment number. 3.2c shows a watershed cut performed after pre-flooding all minima by 10. 3.2d schematic of the pre-flooding filter. The original function is shown in black dotted lines; the color lines show successive iterations.

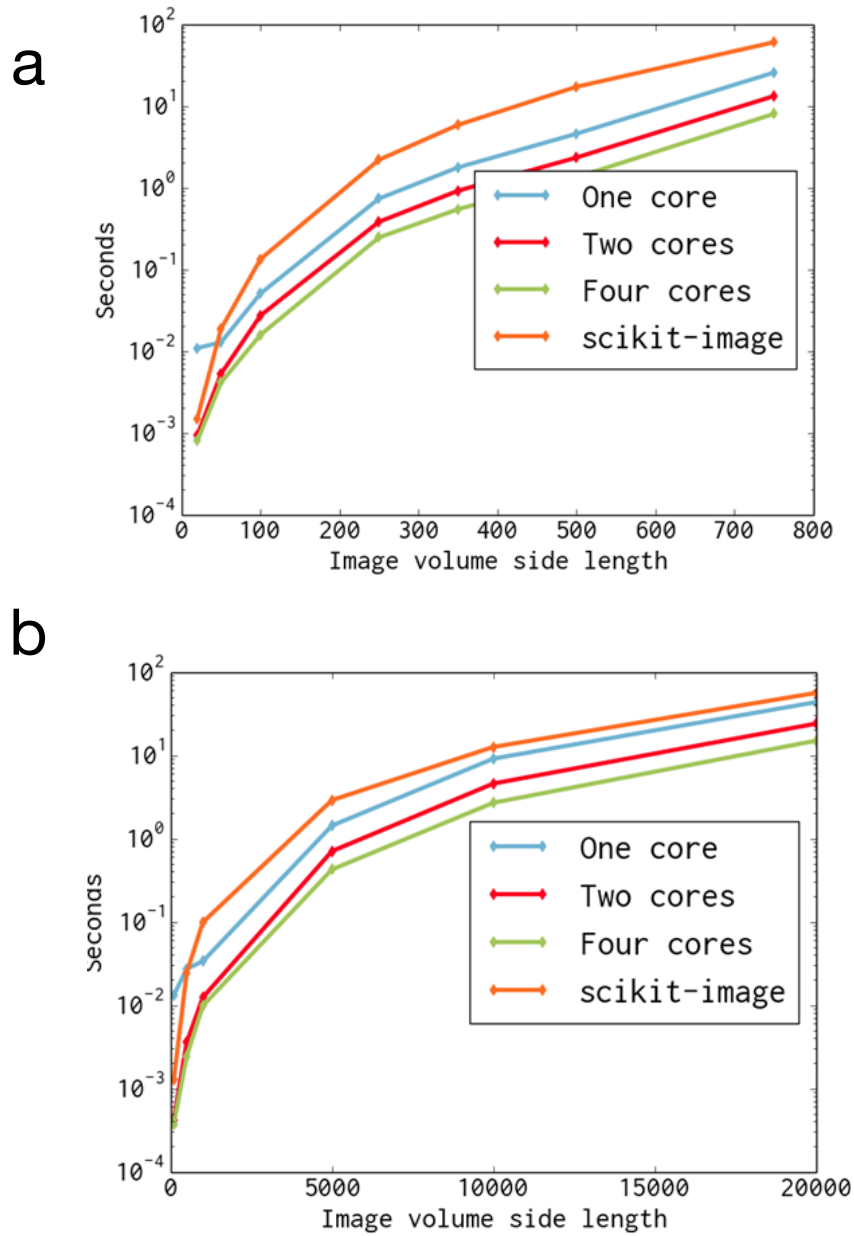


Figure 3.3: Benchmarks of the Gaussian blur filter, compared to `scikit-image`. (a) shows the performance of the 3-dimensional blurring filters, executing a blur with $\sigma = 10$ pixels. (b) show the performance of the 2-dimensional blurring filter, executing a blur with $\sigma = 10$ pixels.

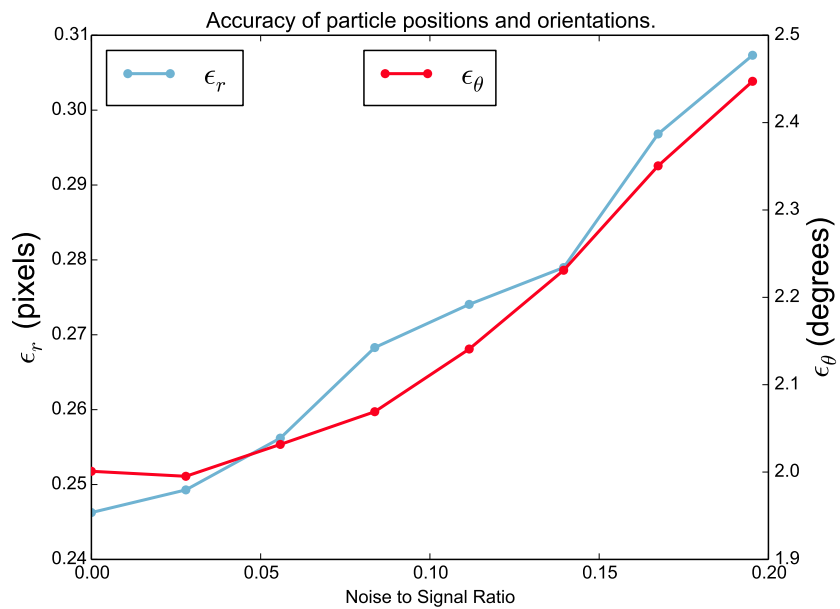


Figure 3.4: Error magnitude as a function of noise for particle identification. Noise was generated to a synthetically generated image volume. The RMS angular and translational deviations are plotted against signal-to-noise ratio.

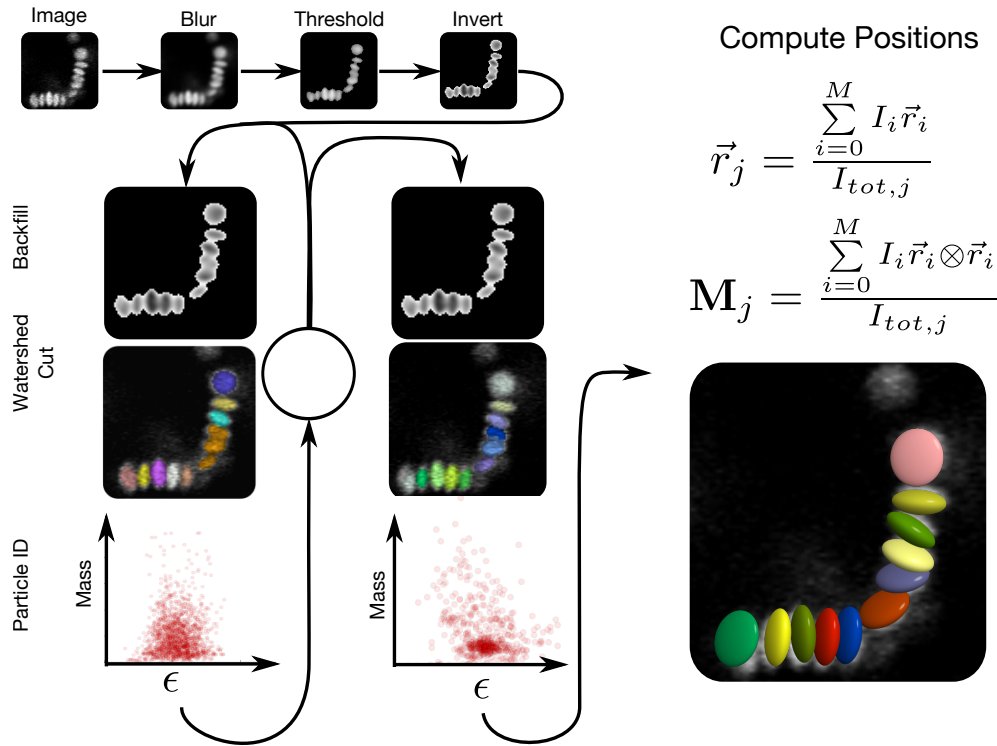


Figure 3.5: Flow diagram of ellipsoid particle identification. Images are blurred, thresholded and inverted. Minima are then backfilled by the maximum depth d . Segments size and eccentricity is calculated, and regions outside an acceptable region are backfilled by an amount 80% less deep and segmented. This process is repeated until all detectable ellipsoids have been detected. Positions are computed as the center of intensity of each segment. Orientations are computed from the eigenvectors of the covariance matrix computed about the center of intensity. CLSM micrographs provided by Lilian Hsiao.

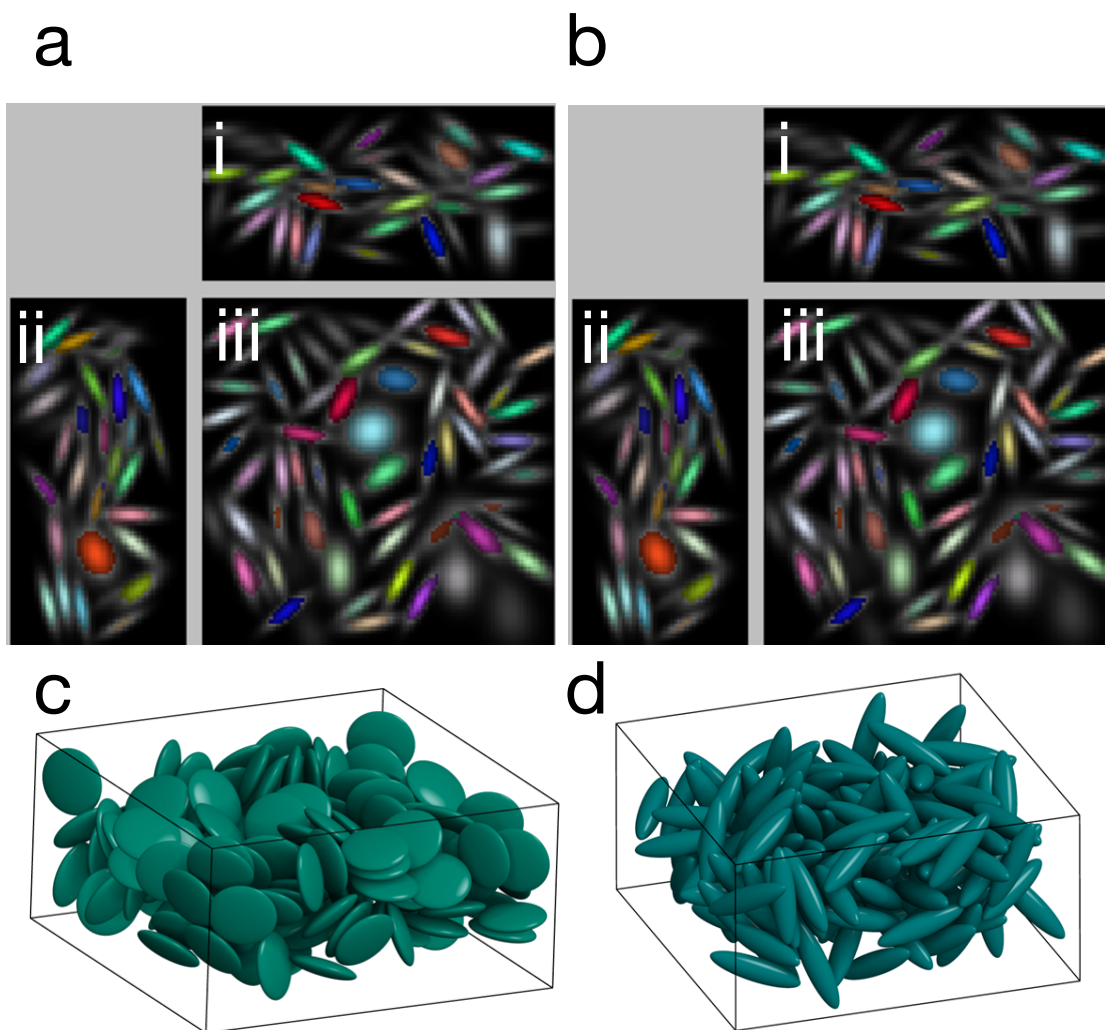


Figure 3.6: Image processing of prolate and oblate spheroids. a i-iii) x-z, y-z, and x-y slices of an oblate spheroid image volume. b i-iii) x-z, y-z, and x-y slices of a prolate spheroid image volume. c) Oblate spheroids extracted from a). d) Prolate spheroids extracted from b).

Chapter 4

Self-assembly of depleted, oblate colloidal ellipsoids

The text in this chapter is based on a manuscript in preparation, co-authored with Lilian Hsiao, Jens Glaser, Michael Engel, Megan Szakasits, Sharon Glotzer and Michael Solomon. All figure panels were jointly prepared by Lilian Hsiao, Benjamin Schultz, Sharon Glotzer and Michael Solomon; specific contributions from Lilian Hsiao are attributed in figure captions.

4.1 Introduction

Helical structures are commonly encountered in nature in the form of proteins[82], viruses[83], and DNA[84, 85]. Their ubiquity has inspired the development of man-made, macro-scale and nanoscale helical structures, which show great potential as mechanical [86] and optoelectronic materials [87, 88, 89]. Nevertheless, these structures are difficult to achieve

artificially without strong applied fields [90, 91, 92], extensive surface modification [15, 93], or pre-fabricated templates [94, 95]. An excellent candidate for creating helical colloidal microstructures with a simple, tunable attraction is the discotic (oblate) spheroid: the axial asymmetry of oblate spheroids promotes bottom-up self-assembly into tilted, columnar arrangements for attractions with ranges that are a few factors larger than the particle dimensions [96]. Thermodynamic simulations[97] and energy minimization calculations[98] show that tilted stack configurations can be a favorable state for some models oblate spheroids, resulting in twisted structures with long range orientational order.

Experiments to probe features of discotic assembly commonly utilize colloidal clay suspensions consisting of nanometer-sized platelets as model systems, due to the ease of synthesizing bulk quantities of these materials. Nematic ordering, in which platelets show orientational but no positional order, are frequently observed even given the polydispersity of these materials, suggesting that the axial anisotropy leads to strong face-to-face entropic forces [99, 100]. Wax disks tend to arrange in columnar stacks even at dilute concentrations [101]. The interaction anisotropy can also manifest as arrested liquids at exceedingly low particle loading[102], and a house-of-cards stress-bearing structure has been previously observed in shear flow [103]. Despite their scientific and technological importance, clay platelets are challenging model systems due to their polydispersity[104]. Their entropic preference for face-to-face ordering is eclipsed by the complex face-to-edge and face-to-face charged interactions [102, 105, 106]. Yet, few experimental methods are capable of generating high quality model colloidal oblate spheroids in bulk quantities; existing techniques utilize biaxial

stretching[107] and blown films[108]. We show that uniaxial thermo-compression is a reliable method to generate monodisperse colloidal PMMA oblate spheroids that can be suspended in refractive index and density-matched solvents.

In this chapter, we study the self-assembly of these monodisperse colloids with addition of polystyrene to suspensions of colloidal ellipsoids inducing a depletion attraction of tunable strength and range. Our experiments and simulations, spanning a wide range of packing fraction and attraction strength, show that aggregates with orientational order form with strong attractions. Analysis of the phase behavior and the kinetics of self-assembly (through quantification of aggregation and local ordering) shows that the development of orientational order in systems driven by long-ranged depletion attraction is accompanied by the arrested kinetics of phase separation. We further note the somewhat surprising lack of chiral bundles in experiments and show how particle shape leads to the production of a large population of achiral, single particle strands upon kinetic arrest.

4.2 Materials and methods

4.2.1 Colloidal synthesis, stability, and self-assembly of PMMA oblate spheroids

Colloidal oblate spheroids are obtained by uniaxial compression of spherical particles. We synthesize the precursor monodisperse poly(methyl methacrylate) (PMMA) spherical colloids (diameter $2a = 1.49 \mu\text{m} \pm 4\%$) stabilized by a grafted layer of poly(12-hydroxystearic

acid) (PHSA) and cross-linked with ethylene glycol dimethacrylate (EGDM) at a 0.5 wt % ratio to the monomer [109]. The steric layer has a thickness of 10 - 14 nm [110]. PMMA colloids are dyed with fluorescent Nile Red to allow for direct visualization with confocal microscopy [110]. The spheres are embedded at a 2.0 wt % concentration in a hydroxy-terminated poly(dimethyl siloxane) (PDMS) ($M_n \approx 110,000$, viscosity $\approx 50,000$ cSt) matrix, in which tin (II) ethylhexanoate and poly(dimethylsiloxane-co-methylhydrosiloxane) are added as a catalyst and a cross-linker respectively (Figure 4.1(a)). The PDMS matrix is heated to a temperature ($T = 150^\circ C$) above the glass transition temperature, T_g , of the PMMA. A uniaxial compression is applied at a pressure of 1144 kPa (starting thickness of film = 2.6 mm, final thickness = 0.6 mm, strain = 0.23) using two flat poly(tetrafluoroethylene) (PTFE) plates (Figure 4.1(b), (c)) to generate oblate spheroids of aspect ratio, $l = b/a = 0.46 \pm 0.09$, where a is the radius of the major axis and b is the radius of the minor axis. The thermomechanically pressed sample is allowed to cool under pressure to room temperature. A solution consisting of 0.75 wt % sodium methoxide dissolved in isopropyl alcohol and hexane is used to release the PMMA spheroids from the PDMS matrix. The complete removal of PDMS is critical for self-assembly experiments. Because this degradation process also removes the PHSA graft copolymer from the surface of the spheroid[111], we re-introduce the PHSA steric layer onto the spheroids through a 72-hour covalent bonding reaction catalyzed by 0.24 vol % dimethylaminoethanol at $T = 80^\circ C$. The reaction is performed at $T \ll T_g$ to avoid any change to the shape of the spheroids. The restabilized particles are cleaned by multiple washings with pure hexane and passed through a $11.0 \mu m$ nylon filter to remove residue.

Figure 4.1(d) and (e) show representative scanning electron microscopy (SEM) images of the precursor spheres and the oblate spheroids formed from thermomechanical compression. The value of a is measured from SEM images of dilute samples in which spheroids lie flat on the substrate and are far apart from each other. The value of b is obtained from the conservation of volume of the starting sphere (Figure 4.1(d)), using the relation $b = \frac{R^3}{a^2}$ [107]. These values are also independently verified during the image processing of confocal microscopy images. For the spheroids used in this study, $a = 1.07 \pm 0.06 \mu\text{m}$ and $b = 0.48 \pm 0.083 \mu\text{m}$ from SEM images.

Spheroids are suspended via solvent transfer in a refractive-index and density-matched solvent at a volume fraction varying from $\phi = 0.003 - 0.036$. The solvent is washed with deionized water and filtered prior to use, and consists of 81 vol % cyclohexylbromide (CHB) and 19 vol % decalin with 1 vol % PHSA and 3 μM tetrabutylammonium chloride (TBAC) to provide charge screening. From conductivity measurements, the Debye length is $\kappa^{-1} = 151 \text{ nm}$ and the ζ potential is estimated to be $\leq 10 \text{ mV}$ [21]. The solvent viscosity ($\eta = 2.5 \times 10^{-3} \text{ Pa}\cdot\text{s}$) is measured with a cone-and-plate geometry on a controlled stress rheometer (TA Instruments, AR-G2).

Single-particle dynamics from particle tracking show that the PMMA spheroids are stable in this solvent for approximately 4 days (Figure 4.1(f)). Specifically, the 1D mean-squared displacement of the spheroids as a function of the delay time, $\langle \Delta x^2(\Delta t) \rangle$, show that spheroids exhibit fully diffusive behavior where $\langle \Delta x^2(\Delta t) \rangle \propto \Delta t$ for measurements conducted at experimental wait times, $t_w \leq 192 \text{ hours}$ (Figure 4.6(a)). The measured orientationally-

averaged translational diffusivity of the dilute suspension is $D_T = 0.08 \pm 0.01 \mu\text{m}^2/s$. This value agrees with the theoretical prediction of the orientationally-averaged diffusivity calculated from parallel and perpendicular components of the Stokes-Einstein diffusivity, $D_{T,\parallel} = k_B T / \eta K_{s,\parallel}$ and $D_{T,\perp} = k_B T / \eta K_{s,\perp}$, to a relative error of 15%. $K_{s,\parallel}$ and $K_{s,\perp}$ are material constants that depend on the geometry of the oblate spheroids[112]. Here, $D_{T,\parallel} = 0.10 \mu\text{m}^2/s$ and $D_{T,\perp} = 0.10 \mu\text{m}^2/s$ (the orientationally averaged value is plotted as a dashed line in Figure 4.6(a)). The self-part of the 1D time-dependent van Hove correlation function characterizes the probability distribution of single-particle displacements. Figure 4.6(b) shows that the spheroids exhibit a Gaussian distribution in the van Hove correlation that is characteristic of a fluid suspension for $t_w \leq 192$ hours[113]. Non-Gaussian dynamics and aggregation begin to set in thereafter, and is seen as a sharp peak in Figure 4.6 (open purple circles).

Self-assembly of the spheroids is induced by addition of a polystyrene standard (molecular weight $M_w = 2.1 \times 10^7$ g/mol, radius of gyration $R_g = 194$ nm determined through static light scattering) at various concentrations ($1.1 \leq c/c^* \leq 5.3$, where c^* is the overlap concentration of the polystyrene) to the suspension. The value of $c^* = 1.12$ mg/ml for the solvent mixture used in this study is determined using the relation $c^* = \frac{3M_w}{4\pi R_g^3 N_A}$, where M_w is the molecular weight of the polymer and N_A is Avogadro's number[114]. The polystyrene molecule acts as a depleting agent and generates a long-ranged attraction (polymer-colloid size ratio, $q_a = R_g/a = 0.40$, $q_b = R_g/b = 0.18$) that favors phase separation and the formation of fluid-fluid equilibrium structure [115].

4.2.2 Confocal microscopy imaging

An inverted confocal microscope (Nikon A1Rsi) equipped with a resonant scanner head and a high-speed piezo stage is used to capture the 3D structure of the self-assembled structures. The spheroids are allowed to quiescently self-assemble for a minimum of $t_w = 120$ min, and images are captured at a distance of $z = 10 \mu\text{m}$ above the coverslip to avoid wall interactions. The image dimensions are $63.5 \times 63.5 \times 30.0 \mu\text{m}^3$, with voxel dimensions of $124 \times 124 \times 124 \text{ nm}^3$. The acquisition time for each image volume is 17 s. Three image volumes are obtained from independent locations within the same sample. In addition, we collect 3D image volumes of two select cases ($\phi = 0.018$, $c/c^* = 4.0$; $\phi = 0.023$, $c/c^* = 1.7$) at regular intervals from $t_w = 0$ to 120 minutes to study the kinetics of self-assembly. We collect images from three independently fabricated samples for these time series.

4.2.3 Image processing and quantification of cluster aggregation and orientational order

From the confocal microscopy image volumes, we compute the positions and orientations of the oblate spheroids with a watershed cut based algorithm described in the previous chapter. This method extends the identification of particle centroids based on the local brightness to arbitrary shapes [34, 76]. Briefly, images are segmented using watershed cuts, and the eigenvectors and eigenvalues of a covariance matrix of each segment is used to compute the shape and orientation of individual particles [116, 73]. Using the watershed-cut method,

we find that the aspect ratio of the oblate spheroids used in the self-assembly studies is $l = 0.50 \pm 0.01 \mu\text{m}$. This value is equivalent to the measurements obtained from scanning electron microscopy, to within experimental error. A photopolymerized sample is used to determine the static error in the particle positions and the orientational angle as described in the previous chapter, resulting in positional uncertainties of $\pm 30 \text{ nm}$ (0.24 voxel size) and angular uncertainties of $\pm 3^\circ$.

Particles are considered to be bonded when they are within a separation that is equivalent to the first minimum of the radial surface distribution function, computed using the elliptic contact function[117]. The fraction of particles in cluster aggregates is f_{clust} . Local orientation order is quantified using an additional angular criterion: particles in contact are considered to be orientationally aggregated if the difference between their orientational vectors and center-to-center separation vector, θ , is ≤ 45 . This gives us the fraction of particles in oriented clusters, $f_{ordered}$. We examine changes in f_{clust} and $f_{ordered}$ as a function of the cumulative number of particles in clusters containing s particles. High values of f_{clust} indicate a large subpopulation of particles that reside within large clusters. Assemblies with high degree of orientational ordering are expected to have higher values of $f_{ordered}$ compared to less oriented assemblies because of the existence of longer thread-like structures within the sample.

4.2.4 Monte Carlo simulations of depletion-induced aggregation

We also conduct Monte-Carlo (MC) simulations of hard ellipsoids using a plugin to HOOMD-blue [118]. We use a penetrable-hard sphere model for the polystyrene depletant. In simulation units, the ellipsoidal colloids have a major axis of 1 and a minor axis of 0.5; the depletant has a diameter of 0.2. We sample colloid volume fractions of 1%, 5% and 10% and depletant concentrations of $c/c^* = 0.2 - 1.4$ by increments of 0.2 to capture condensation and $c/c^* = 1.4 - 4.0$ by 0.35 increments to capture the arrested solid phase. We note the depletant-colloid size ratio ($q = 0.3$) and high concentrations push the boundaries of the validity of the Asakura-Oosaka model[32]. This simplified model will overestimate the net attraction induced by the polymer depletants in this regime due to polymer self-exclusion[33].

Each MC sweep, colloids are either rotated or translated and the move is accepted with the standard Metropolis acceptance probability

$$P_{a \rightarrow b} = \min\{1, \exp(-\beta(U_a - U_b))\}. \quad (4.1)$$

In this system of hard particles U , is either zero (no overlaps) or infinite (if there are any overlaps between colloids with other colloids or depletants have been created by a trial move).

We leverage the idealized depletants to dramatically accelerate our MC sampling scheme.

Rather than explicitly tracking the positions of the depletants, we sample a grand-canonical ensemble of the penetrable hard spheres (PHS) and place a decorrelated set of depletants in the simulation during every colloid trial move[119].

In the original configuration, there are no overlaps between colloids and depletants. Upon moving a colloid, we check for new colloid - depletant overlaps by inserting m depletants uniformly and randomly in a sphere of radius $R = R_{col} + R_{dep}$ centered on the newly moved particle, where R_{col} and R_{dep} are the circumsphere radii of the colloid and depletant respectively. Depletant placements that overlap with the colloid in its original position or other colloids are rejected. The number of depletants m is drawn from a Poisson distribution

$$P(m, \lambda) = \frac{\lambda^m}{m!} \exp(-\lambda), \quad (4.2)$$

with $\lambda = \frac{4\pi R^3}{3} \rho_{dep}$, with ρ_{dep} as the depletant number density. This scheme samples an ideal gas of depletants occupying the colloid system's free volume. If any depletants overlap only with a colloid in its new position, the trial colloid move is rejected. Colloid step sizes were tuned for a 20% acceptance ratio.

4.2.5 Analytic ellipsoid-ellipsoid overlap check

The detection of ellipsoid overlaps and the computation of the distance of closest approach is surprisingly difficult and has generate and interesting body of work. An efficient, analytic scheme to detect ellipsoids in three dimensions follows, described in Wang et al. [120] and in Alfano and Greer [121] (another, iterative algorithm is described in Zheng et al. [122] is capable to detecting overlaps and computing the distance of closest approach). The implementation described was originally implemented by Elizabeth Chen and Michael Engel, and was numerically stabilized by the author. An ellipsoid of arbitrary orientation can be

written $Ax^2 + By^2 + Cz^2 + Dxy + Eyz + Fxz + Gx + Hy + Jz + K = 0$. This can be written as a 4×4 matrix equation $\vec{x}\mathbf{M}\vec{x}$,

$$\begin{pmatrix} x & y & z & 1 \end{pmatrix} \frac{1}{2} \begin{pmatrix} 2A & D & F & G \\ D & 2B & E & H \\ F & E & 2C & J \\ G & H & J & 2K \end{pmatrix} \begin{pmatrix} x \\ y \\ z \\ 1 \end{pmatrix} = 0. \quad (4.3)$$

We can choose the origin to be at the center of ellipsoid A. Ellipsoid B is translated a distance $\{x_0, y_0, z_0\}$, by first computing the appropriate matrix \mathbf{M} about its center and translating it by multiplying by \mathbf{T} defined as

$$T = \begin{pmatrix} 1 & 0 & 0 & 0 \\ 0 & 1 & 0 & 0 \\ 0 & 0 & 1 & 0 \\ -x_0 & -y_0 & -z_0 & 1 \end{pmatrix}. \quad (4.4)$$

Matrices for ellipsoids A and B are thus $\mathbf{A} = \mathbf{M}_A$ and $\mathbf{B} = \mathbf{T}^T \mathbf{M}_B \mathbf{T}$. To detect separation between ellipsoids, one invokes the theorem proved by Wang et al. [120] that the two ellipsoids overlap if and only if the f , defined as

$$f(\lambda) = \det(\lambda \mathbf{A} + \mathbf{B}) = 0, \quad (4.5)$$

has two positive roots. The number of roots of this equation is checked using Sturm’s theorem [123]. The values in the Sturm chain can be directly calculated from the coefficients of $f(\lambda)$ - a direct implementation was numerically unstable due to round-off errors. By exploiting the identity

$$\det(\lambda\mathbf{A} + \mathbf{B}) = \lambda^{-5} \det(\mathbf{A} + \lambda\mathbf{B}), \quad (4.6)$$

we are able to compute the Sturm chain for both determinants efficiently and use the chain with the smallest round-off errors to detect overlaps. The current implementation in HPMC, the hard-particle Monte-Carlo plugin for HOOMD-blue, passes a stress test of over 100 pathological configurations.

4.3 Results

4.3.1 Phase behavior of self-assembled oblate spheroids

We perform a systematic study of the effect of c/c^* and ϕ on the self-assembly behavior of colloidal oblate spheroids (Figure 4.2). The clustering and orientational tendencies of the self-assembled structures are visually apparent in the confocal microscopy images as shown in Figure 4.1 (k) and (l). Figure 4.2 shows the assembly behavior of the spheroids as a function of c/c^* and ϕ . Figure 4.2a shows the fraction of particles in cluster that are larger than 2 (f_{clust}), for each simulation (triangle) and experiment (circles) performed. Both the simulations and experimental data points were sampled in triplicate; horizontal error bars are the standard deviation of the packing fraction. The black line connects the first sampled

points for which $f_{clust} > 0.2$; this delineates a region where phase separation of the colloids and depletants occurs (roughly $\phi \geq 0.01$ and $c/c^* \geq \approx 0.6$).

Figure 4.2b shows $f_{ordered}$ as a function of c/c^* and ϕ . We remark that $f_{ordered}$ lacks a sharp transition as observed for f_{clust} . Instead we see a gradual increase of $f_{ordered}$ with c/c^* for packing fractions larger than $\phi = 0.01$. The nature of this gradual increase as c/c^* - and thus interaction strength - is increased, suggests that the observed configurations are kinetically arrested.

Figures 4.2c-n shows simulation snapshots for c/c^* and ϕ . The lowest $c/c^* = 0.2$ shown at $\phi = 0.01, 0.05, 0.10$ in Figures 4.2 l-n; the colloids never phase separate at this depletant concentration. Figures 4.2 i-k show $c/c^* = 0.6$ and 2.05 respectively for the same values of ϕ . At these depletant concentrations, the colloids phase separate into compact droplets. The smaller droplets at low concentrations would likely condense into a single droplet for all ϕ if we ran the simulations for infinite MC sweeps and were fully equilibrated. Large clusters with little orientational order are observed at highest ϕ probed as well ($\phi = 0.038, f_{clust} = 0.70, f_{ordered} = 0.04$). This type of structure is reminiscent of cluster-like gels formed with weak, short-ranged attractions [124, 114]. As the depletant concentration increases, we note an increase in the local orientational order of the clusters, as can be observed by the increasing $f_{ordered}$ in Figure 4.2b.

Figure 4.2c-e show assemblies for $\phi = 0.01, 0.05$ and 0.10 at $c/c^* = 4.0$; these structures are highly arrested and exhibit a high-degree of local ordering, with the highest values $f_{ordered} \approx 0.6$. The colloids tend to arrest in linear threads. These threads were also

observed experimentally at $c/c^* = 4.0$ (Figure 4.3a-f). We note the absence of large chiral bundles of threads, as observed in Prybytak et al. [97]; in this system, threads only appear when both the experiments and simulations under arrested into ≈ 1 particle wide threads.

4.3.2 Kinetics of orientational self-assembly

To better understand the relationship between orientational ordering and cluster aggregation, we study the growth kinetics of systems for which a distinct transition from orientational to non-orientational aggregation is observed as c/c^* is reduced. Figure 4.3a-f show the time-dependent evolution of assembled structures for a system a propensity to form sample with local orientation ($\phi = 0.018$, $c/c^* = 4.0$, $f_{clust} = 0.89$, $f_{ordered} = 0.34$). At $t_w = 5$ min (Figure 4.3a), the system is comprised of mostly free, mobile spheroids along with short chains of oriented fluid clusters. Between $t_w = 10$ min (Figure 4.3b) and 30 min (Figure 4.3c), there is an increase in the population of oriented clusters, which connect to form longer structures. These structures continue to combine and grow in a linear manner until orientational order ($f_{ordered} = 0.34$) is reached at $t_w = 120$ min (Figure 4.3d-f). Figure 4.3g shows a close-up of a representative oriented cluster of size $s = 6$ found at $t_w = 120$ min.

In contrast, there is no sustained, long-ranged orientational assembly for a similar system with reduced attraction strength. Figure 4.3h-m show the structural evolution for a system with low orientational order ($\phi = 0.023$, $c/c^* = 1.7$, $f_{clust} = 0.95$, $f_{ordered} = 0.08$). Figure 4.3h shows that the structure initializes in a similar manner to Figure 4(a) at $t_w = 5$ min. At $t_w = 10$ min, Figure 4.3i shows that larger fluid clusters with reduced orientational

order compared to Figure 4.3b begin to appear. At $t_w = 30$ min, the clusters aggregate into larger clusters in which little orientational order is observed (Figure 4.3j). From this point onwards until $t_w = 120$ min, the clusters coalesce continuously until heterogeneous regions of dense clusters and large voids are formed (Figure 4.3k-m). Figure 4.3o shows a region in which a high concentration of particles with little orientational order with respect to each other are seen.

We observe similar qualitative trends in our simulations, although the idealized potential yields different plateau values. However, simulations provide a more detailed picture of the particle dynamics than were captured experimentally. Figures 4.4a-c set of particles that assemble into the same cluster after 40×10^6 MC sweeps with $c/c^* = 0.8$ and $\phi = 0.05$ at 1, 10 and 40 million MC sweeps. Between 4.4a and 4.4b, a majority of the particles form an elongated thread-like cluster which then collapses into a compact droplet in 4.4c. Figures 4.4d-f show snapshots from a cluster with $c/c^* = 4.0$ and $\phi = 0.05$ at 1, 10 and 40 million MC sweeps. As in Figure 4.4a-b, extended, thread-like structures form, but now are metastable and persist for the duration of the simulation. This is clear evidence the thread-like clusters are a result of kinetic arrest at high depletion concentration.

The absence of large chiral bundles from simulations and experiments begs the question - in the absence of kinetic arrest, would we observe chiral bundles of oblate spheroids? We initialized 3, 4 and 7 thread bundles; with each thread comprising 10 particles each (Figures 4.4g-i). These bundles are obviously lower free energy than the configurations assembled in simulation - adjacent threads open more free-volume to the depletant than

isolated threads. These bundles are then relaxed for an additional 20×10^6 MC sweeps. The results for $c/c^* = 4.0$ are shown in Figures 4.4j-l. The 3- (Figure 4.4l) and 7- (Figure 4.4j) thread bundles both buckle into twisted bundles; the 4-thread bundle remains achiral. At $c/c^* = 2.0$, all the bundles buckle into chiral structures and continue to evolve toward compact droplets with moderate orientational order; this process only proceeds faster at lower c/c^* . At high depletant concentrations, where threads are metastable, we observe some chiral bundles; however, from random initial conditions the threads arrest before assembling bundles. Our results at lower c/c^* show that these chiral bundles are likely metastable relative towards more compact droplet configurations.

4.4 Discussion

We note the onset of stable threads in our simulations and experiments is coincident with kinetic arrest. The stabilization of these threads inhibits the assembly of the chiral bundles discussed in the introduction. Even still, in systems with a balance of isotropic short-range attraction and long-range repulsion (promoting growth of elongated aggregates) that undergo kinetic arrest [125, 126] the particles form gels made of Bernal spirals, or tetrahelices. We observe that the shape of our colloids yields mechanically stable clusters with only one bond per particle, precluding the formation of spiral structures.

A pair of spheroids i and j have 4 degrees of freedom - $|\vec{r}_{ij}|, \hat{r}_{ij} \cdot \hat{n}_i, \hat{r}_{ij} \cdot \hat{n}_j, \hat{n}_i \cdot \hat{n}_j$.

As per Maxwell's stability condition, in order to be mechanically stable a system needs to have at least as many constraints as degrees of freedom. The effective interaction between

a pair of colloids is computed in Figure 4.5. Figure 4.5a shows the stability of face-to-face colloid minima with respect to $|r_{ij}|$, Figure 4.5b shows the stability relative to changes in particle orientation. A single pair-bond thus provides four constraints corresponding to the four scalars, thus a minimum of 1.25 bonds/particle are required for a mechanically stable structure; in fact the cylindrical symmetry of a linear chain yields a mechanically stable minima with a single bond/particle. In contrast, spherical particles need a minimum of 3 bonds for mechanical stability - the radially symmetric interaction potential provides no dihedral stiffness. As both systems undergo kinetic arrest, the system evolves to a mechanically stable minimum. For oblate spheroids, single particle strands can be present in these minima; for spherical particles, tetrahelices are present in the mechanically stable, potential energy minima with the fewest bonds[127].

We simulate a system of spheres with the same volume at identical depletant concentrations to compare the structures assembled by spheres and spheroids. The valence, or contact, distribution at $c/c^* = 4.0$ is shown in Figure 4.4p. The ellipsoids have a markedly lower valence, with particles with one or two bonds and a peak centered at 4 bonds. By contrast, no spheres have fewer than 3 bonds, and there is a peak at 6 bonds, corresponding to tetrahedrally coordinated structures. Figure 4.4q shows the dependence of the mean valence for spheres and spheroids as a function of c/c^* . Both systems condense at $c/c^*0.6$ - in fact the spheres crystalize into FCC (with 12 contacts). As c/c^* increases, the system begins to arrest and the valence decreases. From $c/c^* = 0.8 - 2.5$, the spheroids have a larger valence than the spheres. Spheres have an geometric limit of twelve contacts, which

spheroids can have more; in compact droplets spheroids have more contacts. As arrest sets in, the sphere system approaches an average contact number of six, while the anisotropic potential can support lower valence, tending toward an average valence of four as $c/c^* \rightarrow 4$.

In cases where we wish to capture the thermodynamic behavior of a system, particularly systems in which particles interact via short-ranged, attractive potentials at low densities, it is common to include cluster MC moves [128, 129, 130].

In this work, we use a single-particle-move MC algorithm and purposely sample arrested configurations of colloids. We observe arrested states that are visually similar to those observed in experiments (Figure 4.2 and Figure 4.3), and show how the form of the potential stabilizes low-valence clusters like those observed experimentally. Our systems are sufficiently dense that the observed arrest in our MC simulations proceeds similarly to the physical kinetic arrest without cluster moves (at least locally), as both relax into the configurations dominated by thread-like clusters. Furthermore, we conduct simulations in which we initialize particle threads next to one another (in Figure 4.4 g-o), and confirm that thermodynamically, these thread-like clusters are disfavored, as we observe threads collapsing into more compact configurations that provide more free volume for the depletant.

The resulting gels and arrested clusters are similar to gels of shape-anisotropic particles[131, 132] with a high degree of local orientational order. These arrested structures result directly from the particle shape driving the formation of thread-like fibers upon arrest into surprisingly low-valence structures. Assembling the chiral structures observed in Prybytak et al. [97], for example, is preempted by kinetic arrest for $\epsilon = 0.5$ aspect ratio spheroids

with depletants. A potential with longer range, and more directionality (to promote the hierarchical assembly of threads) is required - lower aspect ratio colloids with even larger depletant may produce these desirable structures.

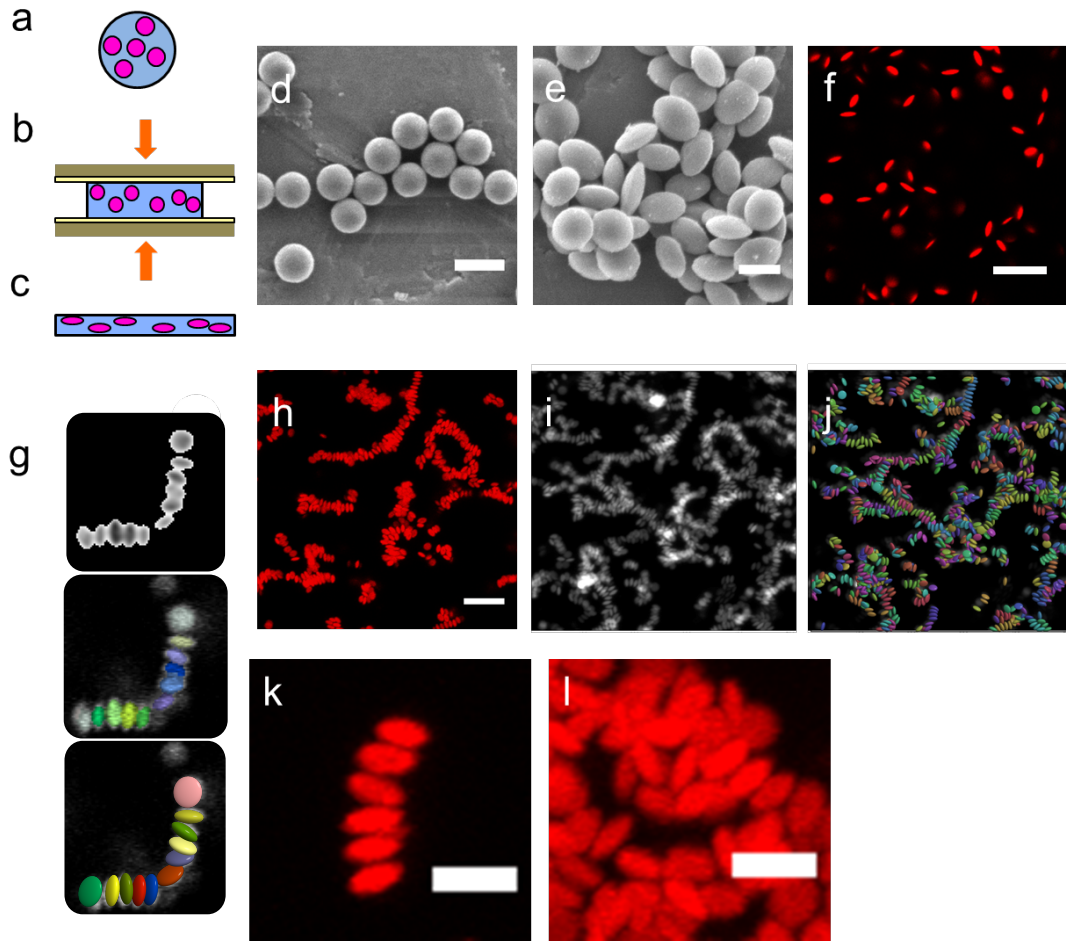


Figure 4.1: Synthesis and stability of PMMA oblate spheroids. Monodisperse PMMA oblate spheroids are generated by (a) embedding PMMA spherical colloids in a PDMS matrix, (b) applying a uniaxial compression at $T < T_g$, and (c) cooling under pressure to room temperature. (d) Representative SEM image of the PMMA spheres prior to thermomechanical compression and (e) representative SEM image of oblate spheroids used in this study, with aspect ratio $l = b/a = 0.46$. (f) Representative confocal image of a dilute suspension ($\phi = 0.010$) of covalently stabilized spheroids (scale bar represents $15 \mu\text{m}$). (g) Schematic of watershed-cut image processing particle shape identification method for oblate and prolate spheroids. Performance of the image processing is demonstrated using: (h) a raw 3D confocal image volume for a sample at $\phi = 0.018$, $c/c^* = 4.0$ (scale bar represents $10 \mu\text{m}$); (i) the same image after thresholding; (j) Renderings of the identified oblate spheroids overlaid on the thresholded image. In (j), clusters are identified by surface-to-surface distance. (k, l), Close-ups of self-assembled structures displaying high degree of orientational order (k) and low degree of orientational order (l); scale bars represent $5 \mu\text{m}$. Particle fabrication, and microscopy by Lilian Hsiao. Image analysis by Benjamin Schultz.

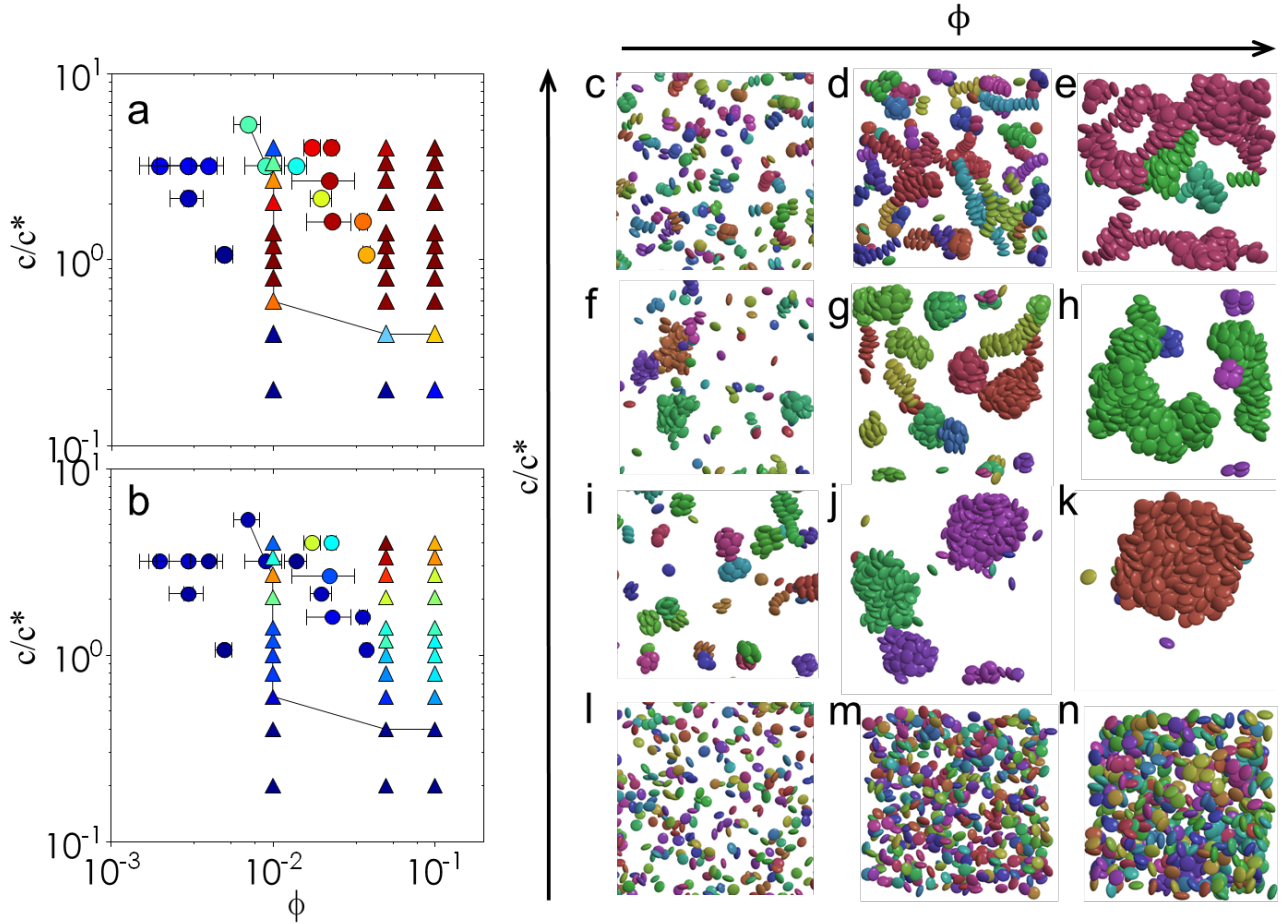


Figure 4.2: Phase behavior of colloidal oblate spheroids as a function of attraction strength (c/c^*) and packing fraction (ϕ). In (a), the degree of clustering based on surface-to-surface separation in the self-assembled structures (quantified by f_{clust}) is shown. In (b), the degree of clustering based on an additional orientational order criterion (quantified by $f_{ordered}$) is shown. In (a) and (b), the solid line demarcates samples with $f_{clust} < 0.2$. Experimental samples are marked as solid circles and simulated structures are marked as solid triangles. Error bars on experimental samples represent standard deviation in ϕ . (c-n), Representative renderings of simulated structures: (c) $c/c^* = 4.00, \phi = 0.01$, (d) $c/c^* = 4.00, \phi = 0.05$ (e) $c/c^* = 4.00, \phi = 0.10$; (f) $c/c^* = 2.05, \phi = 0.01$, (g) $c/c^* = 2.05, \phi = 0.05$, (h) $c/c^* = 2.05, \phi = 0.10$; (i) $c/c^* = 0.60, \phi = 0.01$, (j) $c/c^* = 0.60, \phi = 0.05$, (k) $c/c^* = 0.60, \phi = 0.10$; (l) $c/c^* = 0.20, \phi = 0.01$, (m) $c/c^* = 0.20, \phi = 0.05$, and (n) $c/c^* = 0.20, \phi = 0.10$. Particles are colored by clusters defined by their surface-to-surface separation. Assembly experiments conducted by Lilian Hsiao. Simulations and image analysis conducted by Benjamin Schultz.

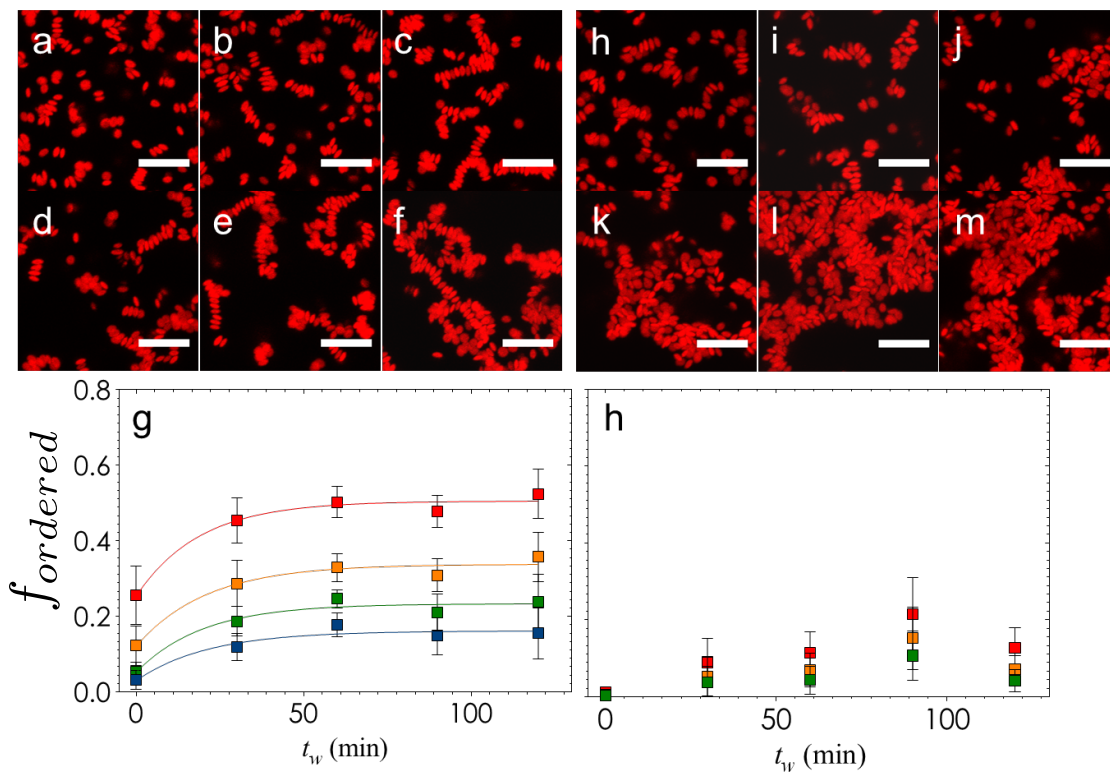


Figure 4.3: Kinetics of oriented and non-oriented self-assembly. a-f) CLSM images of assembly at $c/c^* = 4.0$. h-f) CLSM images of assembly at $c/c^* = 1.7$. Images are taken at $t_w=0, 10, 30, 60, 90, 120$. Scale bars are $10\mu\text{m}$. g) f_{clust} for $s=2$ (red), $s=3$ (orange), $s=4$ (green) and $s=5$ (blue) at $c/c^* = 4.0$. h) f_{clust} for $s=2$ (red), $s=3$ (orange) at $s=4$ (green) at $c/c^* = 1.7$. Experiments and trajectory analysis performed by Lilian Hsiao. Image analysis and trajectory analysis performed by Benjamin Schultz.

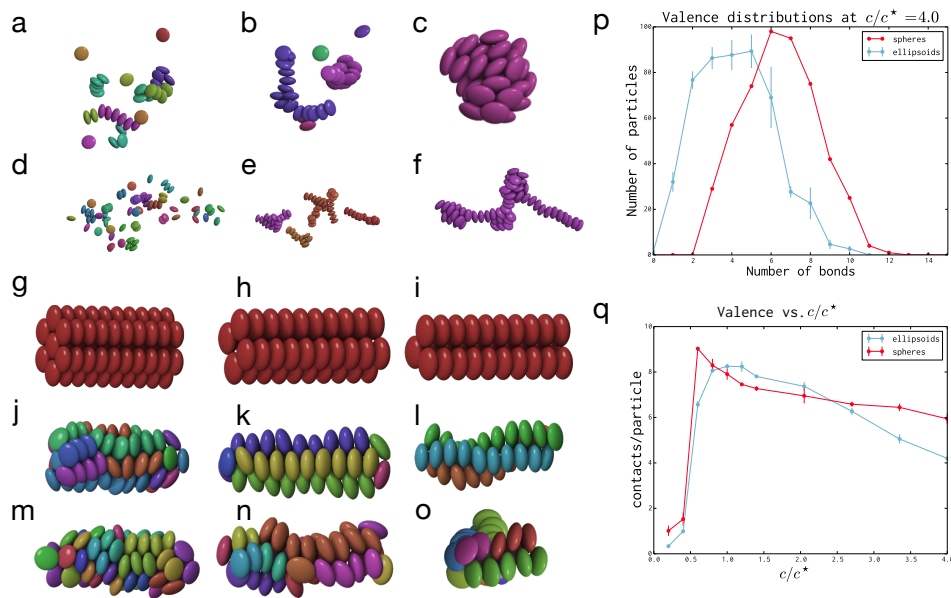


Figure 4.4: Valence of spheres and ellipsoids suspensions in simulation. a-c) Simulation snapshots of an extracted cluster at 1, 10, and 40 million MC sweeps for $c/c^* = 0.8$. d-f) Simulation snapshots of an extracted cluster at 1, 10, and 40 million MC sweeps for $c/c^* = 4.0$. g-i) Initial configurations for thread bundles. j-k) Thread bundles after 20 million MC sweeps, $c/c^* = 4.0$. m-o) Thread bundles after 20 million MC sweeps, $c/c^* = 0.8$. p) Contact distribution of a spheres and spheroids at $c/c^* = 4.0$. q) Mean contact number for spheres and spheroids as a function of c/c^* .

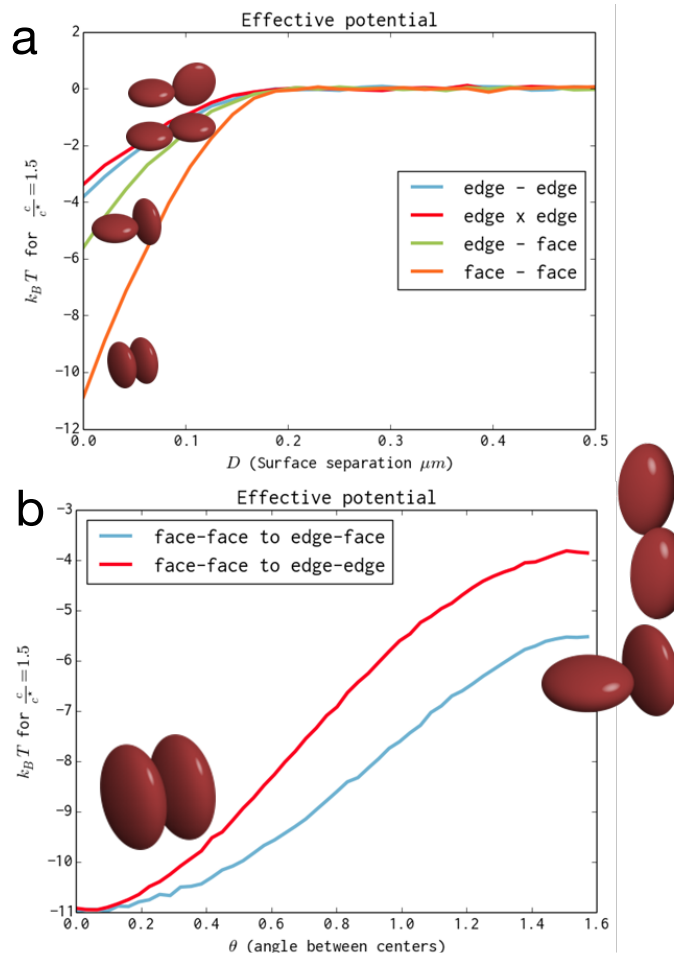


Figure 4.5: Effective interaction potential between two oblate ellipsoids. The potential is plotted as a function of surface separation in (a) for face-face, edge-face, edge-edge and crossed edge configurations. (b) shows the effective as a function of angle between the particle centers while keeping the surfaces in contact. The magnitude of the potential is shown for $c/c^* = 1.5$

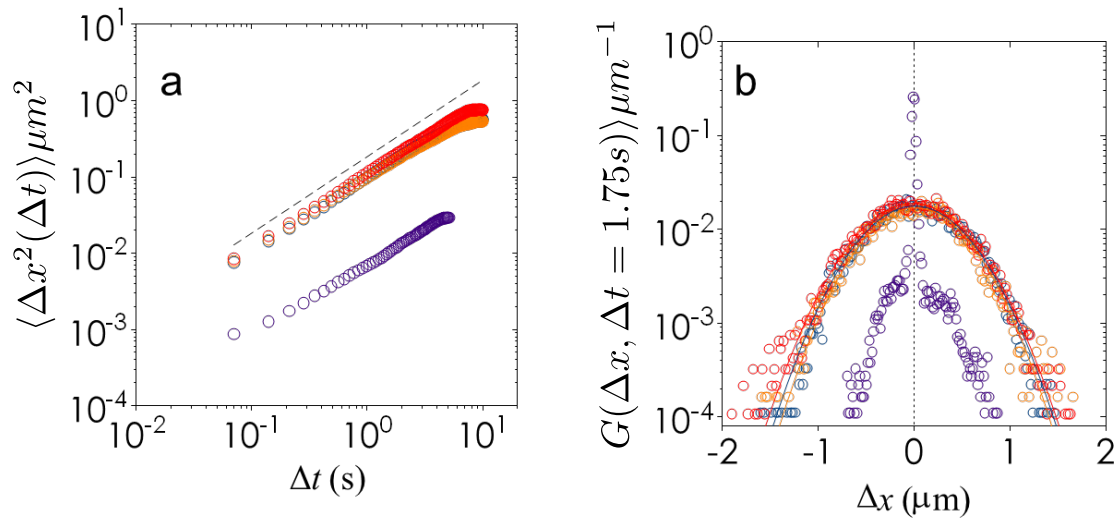


Figure 4.6: Stability of colloidal oblate spheroids without added depletant. (a) The 1D mean-squared displacement as a function of lag time and (b) the single-particle van Hove correlation function for $t_w = 48$ hours (red), 60 hours (orange), 96 hours (blue), and 168 hours (purple). Dashed line in (a) represents the orientation-averaged Stokes-Einstein translational diffusivity. Both (a) and (b) are generated from the dilute suspension shown in Figure 1(f). Experiments and particle tracking performed by Lilian Hsiao.

Chapter 5

Actuation of shape-memory colloidal fibers of Janus ellipsoids

The text in this chapter is drawn in large part from a manuscript co-authored with Aayush Shah, Wenjia Zhang, Sharon Glotzer and Michael Solomon published in Nature Materials [133]. All figure panels were jointly prepared by Aayush Shah, Benjamin Schultz, Sharon Glotzer and Michael Solomon; specific contributions from Aayush Shah and Wenjia Zhang are attributed in figure captions.

5.1 Introduction

The equilibrium self-assembly of patchy particles[93, 134, 135] with anisotropic interactions[14] has shown great versatility in the assembly of structures useful for photonics[136], catalysis[37] and drug delivery[7]. Recent studies have shown that the assembly of shape-anisotropic

patchy particles can lead to the generation of liquid crystal phases with orientational order [137, 78, 138]. We find that Janus ellipsoids, whose geometry is distinct from the more commonly studied case of spherocylinders[139, 140], self-assemble into orientationally and positionally ordered, one-dimensional, self-limiting fibers. The unique positional and orientational order of the Janus ellipsoid self-assembly, a consequence of the curved, quadratic surface of the ellipsoids, is instrumental in facilitating sliding motion upon actuation by AC electric fields. AC electric fields have been widely used to create 1D chain-like structures and close-packed 2D assemblies from simple colloidal particles[141, 142] as well as to assemble patchy spherical colloids into staggered and zig-zag chain structures[40, 41]. AC electric fields have also been used in conjunction with self-assembly to promote order-order martensitic reconfiguration of bulk colloidal crystals made from both spherical[143] and dumb-bell shaped colloids[144]. Here, we show that application of AC electric fields to pre-self-assembled fibers leads to reconfiguration of the ellipsoids through a sliding mechanism. The assemblies are thus shape-memory [145] in the sense that the relaxed assembly, as produced by equilibrium assembly, is deformed into an ordered, elongated structure by application of an external stress, as produced by an AC electric field. When this elongation is reversed by release of the AC electric field, the assemblies regain their original self-assembled ordering.

5.2 Janus ellipsoid self-assembly

Figure 5.1 reports the equilibrium assembly of Janus ellipsoids of aspect ratio (r) given by major axis length ($2a$) / minor axis diameter (D) = 5.0 ± 0.4). The inset of Figure 5.1a

shows the scanning electron microscopy (SEM) image of one such Janus ellipsoid. Figure 5.1a reports the ordered fiber (OrF) equilibrium phase of sulfate-stabilized Janus ellipsoids, observed after 20 hours of self-assembly in a 5mM sodium chloride (NaCl) aqueous solution. The particles were synthesized by the sequential deposition of 7.5 nm of chrome and 15 nm of gold on a monolayer of ellipsoidal particles (see Methods)[78]. Two-channel reflection and fluorescence confocal laser-scanning microscopy (CLSM) was used to identify each half of the Janus particle in the assembled phases[78]. In Figure 5.1b-e, we show a close-up image of one self-assembled fiber. Figure 5.1b shows the fluorescence channel (red) that identifies the uncoated polymer half of the particle, and Figure 5.1c shows the reflection channel (green) that identifies the metallic half of the particle. The composite image (Figure 5.1d) as well as its rendering (Figure 5.1e) shows that the gold faces are preferentially bonded, while the particles are aligned and offset due to the Janus balance and ellipsoidal shape of the particle. We further discuss the positional and orientational symmetry of these fibers in Figure 5.2. Figure 5.1 also shows that the structure of the self-assembled phase is a sensitive function of the pair interactions between the Janus ellipsoids. In pure deionized (DI) water, the Debye layer thickness and thus electrostatic repulsion is sufficiently large that Janus ellipsoids are free particles due to minimal gold-gold binding (free particle (FP) phase, Figure 5.1f). The inset images of Figure 5.1f show the fluorescence, reflection and composite channel for one such particle. At low salt concentrations (1mM), there is sufficient reduction in electrostatic repulsion that gold-gold binding leads to the assembly of Janus ellipsoid clusters (called the close packed cluster (CIC) phase, Figure 5.1g). Janus ellipsoid

clusters are predominantly trimers or tetramers for this specific aspect ratio ($r = 5.0$). The inset image shows the fluorescence, reflection, and composite channel for one such tetramer. At intermediate salt concentrations (2-5 mM), electrostatic repulsion is further reduced, leading to an increased propensity for gold-gold binding. Resultant assemblies are fibers that are positionally and orientationally ordered (OrF phase) as described earlier in Figure 5.1a-e. At even higher salt concentrations (10mM), assembled fibers have neither positional nor orientational order (called the disordered fiber (DiF) phase) because the strong gold-gold attractive force ($\approx 30k_B T$, Figure 5.8) does not permit reorientation of Janus ellipsoid particles on bonding. This kinetic trapping leads to numerous defects in the main chain. There is therefore no internal order in the DiF phase and the DiF structure is likely a non-equilibrium one. The inset images show a close-up view of the fluorescence, reflection and composite channel of one such fiber. In Figure 5.1i, we plot the dimensionless fiber length (l) (length of fiber (μm) / major axis length of Janus ellipsoid (μm)) as a function of the salt concentration for $r = 5.0$. CLSM images of the assembly experiments are shown in Figure 5.11. Janus ellipsoids and observe that the longest fibers ($l \approx 9$) are assembled at a salt concentration of 5mM (as in Figure 5.1a-e). The standard deviations for l are large because the fiber lengths are not uniform due to the stochastic mechanism of fiber formation, which we address later. The OrF phase is unique to Janus ellipsoids and we focus on understanding this phase and exploiting its properties in this chapter.

5.3 Phase diagram and mechanism of Janus ellipsoid self assembly

Figure 5.2a-c reports the OrF phase for aspect ratio $r = 4.1, 5.0$ and 6.8 respectively. As is evident in the inset images, while the lattice constants of the ordered fibers are dependent on the dimensions of the particle, the OrF symmetry is repeated along the fiber for different aspect ratios. Figure 5.2d reports a phase diagram of the experimentally assembled phases observed (FP, CIC, DiF and OrF phases) at different aspect ratios. We note that the OrF phase is observed at different salt concentrations, but only for $r > 3.5$. Thus, this phase seems to require shape anisotropy in addition to Janus functionality, an observation we next investigate through simulations. We conducted molecular dynamics (MD) simulations for $r = 5.0$ using HOOMD-Blue, a GPU accelerated MD code[118, 146]. We model the Janus ellipsoids with ten overlapping beads packed inside an ellipsoidal shell. These beads interact via three potentials: a shifted Weeks-Chandler-Andersen (WCA) potential to account for volume exclusion, an angularly modulated, shifted Lennard-Jones potential to model the van der Waals attraction between gold patches, and a Yukawa potential to model the screened electrostatic repulsion between particles due to surface charges (Figures 5.6 and 5.7)). We choose a rigid body comprised of beads because of its computational simplicity and the ease with which we can model salt screening effects. Our simulations reproduce the observed phases for Janus ellipsoids by varying the Debye layer thickness (κ^{-1}) (equivalent to varying salt concentrations in experiments). Figure 5.2e shows a snapshot of a 1000-ellipsoid simula-

tion assembling from disordered initial conditions into the OrF phase. A fiber extracted from this simulation is shown. Its detailed structure matches the ordering observed in the experiments, as shown in Figure 5.2a-c. The simulations also reproduce the other experimentally observed phases (FP, ClC and DiF phases) as shown in the Figure 5.13. Phase diagrams are shown in for patch coverage in Figure 5.14 and patch sharpness in Figure 5.15. The OrF phase consists of fibers that are composed of four strands of aligned particles, touching end-to-end. The strands lie on the vertices of a rhomb with ellipsoids in adjacent strands shifted by one half-particle length and rotated 90 degrees about the fiber axis (Figure 5.2f). Figure 5.2f(ii,iii) shows the contact network of the ordered fibers. The blue ellipsoids lie on the minor axis of this rhomb and have five contacts and $\approx 30k_B T$ of bonding energy in our simulations. The yellow ellipsoids lie on the major axis of the rhomb and have four contacts. Unlike the blue ellipsoids they do not make contact with the partner ellipsoids across the fiber. The yellow particles are bound by $\approx 20k_B T$ in our simulations. Even with this strong bonding, the strands can still slide along each other with just a small energy penalty ($\approx 3k_B T$, Figure 5.8); thus the amount of shift between adjacent strands can fluctuate significantly and particles are very mobile along the fiber axis. This energy landscape, generated by the particle shape and Janus balance, is therefore the origin of the ability for reconfiguration. It contrasts with the assembly of cylindrical rod, for which ribbon-like assemblies that grow perpendicular to the major axis are predicted[137]. The ellipsoid system therefore differs in two respects - the potential favors alignment of the particles to maximize gold-gold interactions, rather than just contact, and the tapered ends of the ellipsoids allow maximal

contact area when the particles are in fibers rather than ribbons. While the OrF motif is predominant, Figure 5.2g shows the two most common types of defects, observed in both simulations and experiment. On the left, an extra particle is inserted into the four-particle motif while on the right, a particle is missing from the four-particle motif. These defects necessarily destroy the long-range order in the fibers. However, the fibers observed in experiment and simulation has well defined ordered motifs that persist across many unit cells; fibers rarely contain more than one defect. Figures 5.2h(i-iii) report the growth mechanism of an ordered fiber. First, the particles form clusters containing between three and five particles. These clusters diffuse and coalesce into larger clusters (Figure 5.2h(ii)). Clusters of more than five particles are elongated, but do not possess the same four-particle motif observed in the OrF structure due to end effects. The Janus particles try to maximize the contact area of their gold patches; these elongated clusters tend to terminate in trimers rather than dimers. These elongated clusters continue to diffuse and coalesce with other clusters when their ends, which have the most exposed gold patch, come in contact (Figure 5.2h(ii)). Once the fibers have reached an l greater than 4 (≈ 16 Janus ellipsoids in a fiber), the particles rearrange into their equilibrium, OrF structure (Figure 5.2h(iii)). We attribute this ability to rearrange to the low potential energy changes for sliding along the gold patches of neighboring ellipsoids ($< 3k_B T$) relative to bonding strengths in the OrF structure ($\approx 30k_B T$) (Figure 5.6). We believe the growth of these fibers is comparable to a step-growth polymerization of the four-particle unit cell components; however, the internal rearrangement of the unit cell upon bonding complicates modeling of the average equilibrium length of the fibers[147]. Our

simulations thus describe the self-limiting, one-dimensional growth mechanism of the OrF structure and shows that the symmetry of this structure is a result of the particle geometry and torsional potential.

5.4 Simulations of Janus ellipsoid equilibrium assembly

We simulated the self-assembly of Janus ellipsoids using HOOMD-Blue Brownian dynamics at constant volume and temperature. We present simulations representative of two salt concentrations (1mM NaCl and 2.5mM NaCl) for Janus ellipsoids of an aspect ratio of 5.0 run for 500 million time steps. The rigid bodies are constructed from 10 overlapping spheres, equally spaced along the major axis with diameters such that they touch the surface of the ellipsoidal particles they represent. Acting at each sphere is a shifted, angularly modulated Lennard Jones potential, a shifted WCA potential and a Yukawa potential.

Volume exclusion is modeled by a shifted WCA pair potential of the form

$$U_{SWCA} = -4\epsilon \left(\left(\frac{\sigma}{r - \Delta} \right)^6 - \left(\frac{\sigma}{r - \Delta} \right)^{12} \right) \quad (5.1)$$

where $\sigma = 1.0$ is the scale of the repulsion, $\epsilon = 0.5$ is the strength of the repulsion and $\Delta = 1 + \frac{d_i + d_j}{2}$ (d_i is the diameter of bead i) is the shift parameter for beads i and j . We truncate and shift the potential at $r = \delta + 2.0^{1/6}\sigma$. We model the van der Waals attraction between gold patches with an angularly modulated, shifted Lennard-Jones

potential of the form

$$U_{SAMJL} = -4\epsilon \left(\left(\frac{\sigma}{r - \Delta} \right)^6 - \left(\frac{\sigma}{r - \Delta} \right)^{12} \right) \Theta(w(\hat{n}_i \cdot \hat{r}_{ij} - \chi)) \Theta(w(\hat{n}_j \cdot \hat{r}_{ji} - \chi)) \quad (5.2)$$

where \hat{n}_i and \hat{n}_j are the Janus patch unit directors of particles i and j , \hat{r}_{ij} is the center-to-center separation unit vector, $\chi = 0$ is the Janus balance, $w = 3$ is the angular sharpness. Θ is a smoothed step function of the form

$$\Theta(x) = \frac{1}{1 + \exp(-x)}. \quad (5.3)$$

$\chi = \cos \frac{\theta}{2}$, where θ is the angular coverage of the attractive patch and can range from -1 (patch covers entire particle) to 1 (no patch). w can range from 0 (for which there is no angle modulation) to infinity, where this potential is identical to the angular modulation of the Kern-Frenkel potential. Finally we account for the particle charge and electrostatic screening with a Yukawa potential of the form

$$U_{yuk} = \frac{\epsilon \exp(-\kappa r)}{r}, \quad (5.4)$$

where κ is the inverse Debye screening length. We obtained estimates of the parameters for these potentials by conducting DVLO calculations for the gold patch. Parameters used in the simulations are tabulated in 5.1. Simulations were run at a reduced temperature of

	AMSLJ: ϵ	σ	w	χ	SWCA: ϵ	σ	Y: ϵ	κ
2.5 mM NaCl	0.5	1.0	3.0	0	0.5	1.0	50.0	0.15
1.0 mM NaCl	0.5	1.0	3.0	0	0.5	1.0	50.0	0.45

Table 5.1: Table of Janus ellipsoid potential parameters

$T = 0.2111$ and a density $\phi = 0.04$. Figure 5.13a. shows a comparison the 2.5 mM and the 1.0 mM potentials. The sphere bead diameters are the diameters in the shifted WCA and Janus LJ potentials, not energy isosurfaces. The blue halo represents the strength of the electrostatic repulsion from the Yukawa potential. The interaction energy between two ellipsoids is plotted for two parallel ellipsoids as they move across one another. These plots show that the potential is to several percent of $k_B T$, despite the bumpy appearance of the shifted-diameter bead representation. At 1.0 NaCl salt concentration, electrostatic repulsion at the tips of the ellipsoid overwhelms the LJ attraction, focusing the attractive patch be the ellipsoids around the center to the ellipsoids. At 2.5 mM NaCl, the LJ attraction overcomes the electrostatic repulsion and the ellipsoids are attractive along the entirety of their patch.

Figure 5.13b. shows the fluctuation of the potential of a particle in the ordered fiber configuration as it slides along the axis of the fiber. The total binding energy is $\approx 30k_B T$, but the energy to slide along the fiber axis is less than $2k_B T$; the particle is very mobile along the fiber axis enable equilibration of the 1D structure and reconfiguration.

5.4.0.1 Computational phase diagram: fluid and horizontal fiber phase

Fluid fibers occur in a region where attractions are weak, and the screening length is short; the attractive interactions are not strong enough to drive ordering, but the clusters extend

beyond just 3-5 particles clusters and are not ordered (Figure 5.13). They are distinct from the disordered fibers, which have fallen out of equilibrium; these clusters break up and re-form.

The horizontal fiber phase occurs at very low temperatures and moderate screening lengths (Figure 5.13). The repulsion from the Yukawa potential overwhelms the attraction at the ellipsoid ends. Instead of growing parallel to the long axis, the attractive centers of the ellipsoids drive growth perpendicular to the director.

5.4.0.2 Janus balance and sharpness effects

In the phase diagram (Figure 5.14 and 5.15), we observe bilayer clusters when $\chi < -0.09$ and $w \geq 7.37$. These are essentially bilayer clusters with all of the ellipsoids aligned along their major axis. The ordered fibers are described in the previous sections. The trimer fibers ($0.15 < \chi < 0.21$) result from shrinking the angle of the patch so that the bonds no longer support the contact network of the OrF phase; as in previous work on spherocylinders[137] the fibers in this narrower patch regime are disordered chains of bundles of 3 particles strands. Above $\chi = 0.24$, no elongated clusters or fibers form, only clusters. The narrow angular patch coupled with the particles' geometry prevents the growth of extended structures.

5.5 Directed assembly of Janus ellipsoids by AC electric fields

Application of AC electric fields reconfigures the equilibrium assembly phases of the Janus ellipsoids, as reported in Figures 5.3. Figure 5.3a shows a schematic of the coplanar AC electric field device used for these experiments (see Methods). A constant root mean square (RMS) voltage of 10 V and frequencies ranging from 1 kHz to 10 MHz were applied across the 1 mm gap and the resulting structures are visualized by CLSM. Figure 5.3b reports the phase diagram of the assembly phases observed for Janus ellipsoids at different salt concentrations and varying frequencies. At low frequencies, the main effect of the AC electric field is to align the self-assembled Janus ellipsoid phases (see phase diagram, Figure 5.2) in the direction of the electric field lines. Thus, as a function of salt concentration we observe aligned free particle (AFP), aligned close packed cluster (ACIC) and aligned ordered fiber (AOrF) phases (Figure 5.12). At higher frequencies, however, additional ordered phases are observed. The attractive force of the induced dipole causes the AFP and ACIC phases to combine into a staggered chain (SC) phase. This ordered phase, observed previously for Janus spheres 15, is shown in Figures 5.3d and, in close up, in Figures 5.3e. After image processing, the coordinates of the chains are rendered as in Figures 5.3f. Janus ellipsoids are bonded by their tips on the gold half of the particle to two other particles and the ball and stick diagram shows the various bonds between the Janus ellipsoid particles in the SC configuration (Figures 5.3g). At salt concentrations at which the OrF phase arises, application of an AC electric

field leads to generation of a new chain-link (CL) phase that resembles the symmetry of common jewelry chains (Figure 5.3h). A close up view of the assembled fiber along with a ball and stick diagram that depicts particle-particle contact bonds is shown in Figures 5.3i (3D rendering, Figure 5.3j). The symmetry of the repeated unit cell of the CL phase is a four-particle motif of two pairs of ellipsoids, with each pair oriented 180° relative to each other. Each pair is connected at the tip to an adjacent pair oriented 90° relative to it. Thus, each Janus ellipsoid in this assembly has four contact bonds with adjacent Janus ellipsoid particles. This phase, a reconfiguration of the equilibrium OrF phase, has no analog in the case of Janus spheres. The existence of the SC phase is expected for Janus particles[40]. In the appropriate frequency ranges, the electric dipole moment of the Janus ellipsoid moves away from the ellipsoid center of mass toward the extremities of the Janus gold half of the particle (Figure 5.3c). These dipoles chains create a staggered chain to minimize electrostatic energy. Simulations show that the SC structure is observed for particles that interact with a pair potential that forms clusters at equilibrium when an additional field-induced dipole is added at the ends of the gold half of the particle. This result is consistent with experimental observations (c.f. Figures 5.3d). In contrast, the origin of the CL structure is an emergent, unexpected outcome of the application of AC electric fields to Janus ellipsoids self-assembled into OrF fibers. Often, AC electric field structures can be explained by treating each particle as an individual, induced dipole. In that case, the CL structure would have pairs of dipoles parallel to each other, which is energetically unfavorable. Hence, one would expect the CL structure to be suppressed in favor of energetically favorable SC structures. However, the

SC structure is not observed on application of an AC electric field to self-assembled Janus ellipsoid particles. We note parallel pair configurations of elongated Janus particles in AC electric fields have also been observed [148]. The mechanism driving the elongation of the OrF structure into the CL structure is not fully understood. Previously, chaining in AC fields has been modeled as the balance of a field-induced energy that favors extension and a surface tension contribution that favors contraction[149]. Several microscopic mechanisms that may drive the OrF to CL transition were furthermore evaluated . Competition between offset induced dipole moments and the monopole moments of the Janus ellipsoids is a potential mechanism for the reconfiguration. If the induced dipole moment is sufficiently offset and small (Figure 5.10), we predict that the CL structure is stable relative to the SC structure at high salt concentrations. Additionally, electrophoretic forces acting on separated charges could drive the transition. Finally, constrictive inductive forces could contribute to fiber elongation (Figure 5.9), but the required current may dissipate too much power given the resistivity of thin-film gold. Resolving among these mechanisms with recently developed methods [150] is a potential direction for future study.

5.5.1 Simulations of Janus ellipsoid configurations in AC field

We used COMSOL's AC Field module to calculate behavior of a Janus ellipsoid in an AC electric field. We divide our 3 dimensional domains into 4 regions and integrate the total electromagnetic energy density[151]. The polystyrene ellipsoid is modeled as a permittivity of 5.0. A 30 nm gold coating is modeled by a conducting shell using a floating potential

boundary condition. We model the bulk ionic solution with permittivity $\epsilon = 78$ and conductivity $\sigma = 10^{-2}S/M$ and a place and 100nm double layer with permittivity $\epsilon = 78$ and conductivity $\sigma = 0.2S/M$ around the entire ellipsoid. The qualitative results are insensitive to changes to geometry and parameters. However, we were unsuccessful in finding the CL structure as an energy minimizing structure, indicating additional physics may be required to explain its formation.

5.6 Actuation of Janus ellipsoid fibers by AC electric fields

The OrF phase can be rapidly and reversibly reconfigured into the CL phase upon the application of an external AC field. Figure 5.4 reports the short-time actuation of one-dimensional assemblies by switching between the self-assembled OrF phase and directed assembly CL phase upon application of AC electric fields (10 V_{rms}, 1 MHz). Figure 5.4a reports a close-up view of carboxylate-stabilized Janus ellipsoids self-assembled into an OrF phase fiber (2 mM NaCl in DI water, see Methods). The AC electric field rapidly reconfigures the OrF phase fiber into the CL phase (Figure 5.4b). This reconfiguration elongates the fiber due to the difference in lattice parameter between the OrF and the CL phase. Elongation of the fiber length is maintained as long as the AC electric field is applied, as shown in Figure 5.4c. Removal of the AC electric field leads to reconfiguration of the fibers from the CL phase to the OrF phase, and a concomitant reduction in the length of the assembly (Figure

5.4d). This structure is now identical to the initial, equilibrium assembly shown in Figure 5.4a (self-assembled OrF phase). This elongation in fiber length is quantified as a function of time by processing CLSM images taken at a rate of 30 frames per second (fps, Figure 5.4e). The reconfiguration in fiber length is rapid: full extension of the fiber occurs within 1.5 seconds, while relaxation of the fiber occurs within 3.5 seconds. This process can be reversibly repeated multiple times on switching the AC electric field as noted in Figure 5.4f. The extension in fiber length is measured to be $36 \pm 7\%$ and we note that this extensional strain is independent of the initial fiber length as shown in Figure 5.4g (based on analysis of 30 fibers). The assembly goes out of frame for certain time periods and hence Figure 5.4 e,f do not show data points at all time intervals. We add a dotted line to the graph to show the approximate fiber length for those time intervals. The amount of extension and contraction induced by the reconfiguration is consistent with the self-assembled and emergent structures. In the OrF phase, the unit cell has a rhombic cross-section comprised of four Janus ellipsoids, only two of which are in contact (Figure 5.4h,i). The two ellipsoids not in contact slide until they come into contact with each other due to both magnetic compression and electrostatic extension (compare Figure 5.4i and Figure 5.4k). This leads to an extension of the fiber into the CL phase (Figure 5.4j). These geometric considerations yield a net predicted strain of 41.4% in the unit cell (Figure 5.4j). Accounting for the finite size of the fibers and the average length of the fibers in our experimental measurements, we predict the strain to be 33.1% from geometric considerations, (Figure 5.4j) which is within the error bars of the 36% strain amplitude measured experimentally for the shape-memory OrF to CL transition. The

simulations furthermore suggest that the CL structure, although weak relative to biological actuators, could support measurable forces. Specifically, a lower bound on the force to extend from the OrF to CL conformation is estimated to be 0.1 pN/particle. Given that the average chain contains about 50 particles (Figure 5.5f) and that the CL cross sectional area is $1 \mu\text{m}^2$, the force to extend is ≈ 5 pN and the force per unit area is ≈ 5 Pa. This force to extend is comparable to the stall force of molecular motors[152]. The force per unit area is much weaker than biological actuators such as myofibrils[153] and actin networks[154].

5.7 Control of Janus ellipsoid fiber length

Traditionally, external fields have been used to accelerate self-assembly[155, 156], but also more rarely to create defect-free, higher quality assemblies[157]. Over long-time scales, the unique, emergent response of the OrF phase on micro-actuation by the AC electric field permits the formation of longer, more uniform fibers as reported in Figure 5.5. Figure 5.5a shows the initial equilibrium phase of carboxylate-stabilized Janus ellipsoids (assembled at 2.5 mM salt). Application of a 10 Vrms 2 MHz AC square wave electric field leads to reconfiguration of the OrF phase to the CL phase (c.f. Figures 5.3). The fiber ends of assembled fibers in the CL phase are attractive due to dipoles induced by the AC electric fields. A close-up view (Figure 5.5b,c) shows that smaller fibers not only combine to form larger fibers (as depicted by arrows in Figure 5.5c), but also align in the direction of the AC electric field. Subsequent removal of the AC electric field leads to reconfiguration of the CL phase fibers back to self-assembled OrF phase fibers, but while still maintaining the

length of the fibers achieved through application of the AC electric field. This change is evident in the dramatic increase in fiber length of the self-assembled fibers immediately after application of the AC electric field for 30 minutes (Figure 5.5d). The chains are thus not self-limited in length in AC electric fields. We note that the fibers are not only longer but also more uniformly ordered, consistent with results of simulations (Figure 5.2), which show that long self-assembled Janus ellipsoid fibers promote internal particle motion that leads to increased uniformity in self-assembled fibers. Thus, the application of AC electric fields promotes "annealing" of fibers and improves the uniformity of fibers. Over time, we note that Brownian fluctuations cause the fibers to lose orientational alignment along the AC field direction, break and attain their equilibrium length. However, there is a net increase (Figure 5.5e) of a factor of 2.5 in the dimensionless fiber length (Figure 5.5f) at 24 hours after removal of the AC electric field relative to the original self-assembly. This increase in length occurs because at higher salt concentrations, fibers become kinetically trapped during self-assembly. Application of AC electric fields permits the assembled fibers to escape this kinetic trap and achieve an equilibrium fiber length, just as in the annealing of other materials with slow kinetics. This net increase in fiber length is, however, not observed for Janus ellipsoids assembled at 2mM salt concentration (Figure 5.5f) because at this lower salt concentration, fibers were not kinetically trapped during self-assembly and hence the equilibrium fiber lengths obtained after application of the AC electric field are similar to self-assembled fiber length distribution. Thus, the AC electric fields, applied in the long term, modify the kinetic pathways for assembly and can therefore be used as a tool to control the

length of the shape-memory colloidal assemblies

5.8 Experimental methods

5.8.1 Janus ellipsoid synthesis

Janus ellipsoids were synthesized using methods described in Shah et al. [158]. Here, we synthesize carboxylate stabilized ellipsoids (F-8820, Invitrogen Inc) as well as sulfate stabilized ellipsoids (F-8851, Invitrogen Inc) using the same procedure. The zeta potential of the ellipsoids in DI water is measured to be ≈ 38.2 mV. Briefly, $300\mu\text{L}$ of a 2-wt% PS spherical particle solution is homogenized with 7.5 mL of a 10-wt% aqueous PVA solution. This solution is poured into Omni trays. The solution is allowed to dry overnight to form uniform $\approx 40\mu\text{m}$ thick films. This film is then cut into strips and placed in a custom made uniaxial mechanical stretching device built in an oven. The strips are first heated above the glass transition temperature of PS ($\approx 120^\circ\text{C}$) and then uniaxially stretched using the stretching device. The aspect ratio of the ellipsoidal particle can be controlled by the strain applied on the PVA strips. The strips are then allowed to cool at room temperature and dissolved in water. This step releases ellipsoidal particles that are centrifuged at 5000g and redispersed in ultrapure deionized (DI) water (Life Technologies) at least five times. Next, we use spin coating to create a monolayer of the ellipsoidal particles. A microscope glass slide (Fisher Scientific) is first placed in a base bath (30-40 g potassium hydroxide pellets (Sigma Aldrich) dissolved in 100mL water and 400mL isopropanol (Sigma Aldrich)) for ≈ 30 minutes. The

glass slide is then thoroughly rinsed with water. The uniform ellipsoids synthesized earlier are also redispersed in 300 μL of ethanol. This solution is then spin coated onto the treated microscope glass slide to create a uniform monolayer of ellipsoidal particles. Finally, the glass slide with the monolayer of ellipsoidal particles is placed in an e-beam evaporator. Vertical deposition of 7.5 nm chrome and 15 nm gold onto the glass slide leads to preferential deposition of chrome and gold on one half of the ellipsoids to create Janus ellipsoidal particles. These Janus ellipsoidal particles are then swept off the substrate and dispersed in water. These particles are then centrifuged (1000g) and redispersed in ultrapure DI water at least 5 times to remove impurities from the solution. Finally, the particles are dispersed in ≈ 2.5 mL of ultrapure DI water to create a stock solution.

5.8.2 Chamber for AC electric field device

Glass spacers are first created by drilling a 0.5 cm hole in a microscope glass slide and cutting into 2 cm by 2 cm squares. The glass spacer is stuck to the coplanar electrode coverslip using an imaging spacer (Grace Bio-Labs imaging spacers, GBL654002). We also drill 35 x 50 mm coverslips with a 1 mm hole. This slide is attached to the glass spacer using another imaging spacer. We ensure that the hole in the cover slip is positioned above the hole in the glass spacer. This leads to the creation of a chamber with an inlet for the colloidal suspension. The colloidal suspension is subsequently pipetted into the chamber and used for experiments.

5.8.3 Synthesis of ellipsoids with varying aspect ratios

Ellipsoids are synthesized using methods described in the main text. The aspect ratio of the colloidal particles is controlled by the strain applied during the uniaxial extension of the PVA strips. We synthesize aspect ratio 2.1 ± 0.2 , 3.2 ± 0.2 , 5.0 ± 0.4 and 6.8 ± 0.9 ellipsoids on application of strains of 0.45, 0.9, 1.4 and 4.2 respectively to the PVA strips using the uniaxial stretching device.

5.8.4 Self-Assembly of Janus ellipsoids

A 2.5 mL stock solution of the Janus ellipsoid particles is created using methods described in the previous section. The particles in the stock solution are dispersed using a horn sonicator (Cole-Palmer Instruments) for 30 seconds. A variety of sodium chloride salt concentrations are created in ultrapure DI water (1 mM to 10 mM). 300 μ L of the stock solution is then centrifuged and the supernatant is replaced by 300 μ L of the required salt concentration. Janus ellipsoids in the salt solution are sonicated using the horn sonicator for 30 seconds and placed in one of the wells of an 8-well Lab-Tek II chambered #1.5 German coverglass system (Fisher Scientific). This holder was previously treated in the base bath for at least two hours, and thoroughly rinsed with water before addition of the Janus ellipsoid solution. The particles are then allowed to sediment and self-assemble for 20 hours before imaging with a confocal laser-scanning microscope (CLSM, Nikon A1r).

5.8.5 Self-assembly of carboxylate-stabilized Janus ellipsoid particles

Figure 5.1 reports the self-assembly of sulfate-stabilized Janus ellipsoids (aspect ratio) at different salt concentrations. We demonstrate the assembly of similar structures from particles with different surface stabilizing groups. Here, we demonstrate the assembly of carboxylate-stabilized Janus ellipsoid particles. Carboxylate-stabilized Janus ellipsoids are synthesized from $1.1\mu\text{m}$ diameter spherical particles (F-8820, Invitrogen Inc) using methods described in the main text. These particles are then self-assembled at different salt concentrations and results are depicted in Figure SI-5. The free particles (FP) phase is observed at 0 mM salt. Addition of 1 mM salt leads to formation of a cluster phase (ClC). Ordered fiber (OrF) phases are observed at 2 mM and 2.5 mM. Disordered fiber (DiF) phases are observed at higher salt concentrations (3 mM and 5 mM). We note that these phases are similar to the ones observed for sulfate-stabilized Janus ellipsoid particles. However, ordered fibers are formed at lower salt concentrations as compared to the sulfate-stabilized particles. The transition between the OrF and DiF phase also occurs at lower salt concentrations. We attribute this change to the variation in surface charge of the sulfate-stabilized and carboxylate-stabilized particles. We however note that the assembly structures are similar to those observed for the sulfate-stabilized Janus ellipsoidal particles (Figure 5.2 main text).

5.8.6 AC field assembly of Janus ellipsoids

AC field assembly of Janus ellipsoids is performed in a device with coplanar electrodes for easy visualization with a CLSM 13 15. Coplanar electrodes are created by depositing 7.5 nm chrome and 15 nm gold on a coverslip (35 x 50 cm, Fisher Scientific) that has a 1mm thick (50 cm long) masking tape placed in the center of the slide. After deposition of the metal, the masking tape is removed to create a 1 mm gap between the two coplanar electrodes. This coverslip with the coplanar electrodes is then placed in the base bath for ≈ 1 hour before use. After thoroughly rinsing the coverslip with water, a chamber is constructed to hold the colloidal suspension. T2 thermocouple wires (0.5 mm diameter, Goodfellow Inc) are glued to each of the coplanar electrodes using silver epoxy (MG Chemicals). The colloidal suspension is then allowed to sediment and self-assemble for ≈ 20 hours. The wires are subsequently connected to an AC field generator (Rigol DG 1022). The AC field generator is used to apply a 10 Vrms square waveform at different frequencies across the colloidal suspension.

5.9 Hypotheses: mechanisms driving elongation of chains in AC electric fields

We consider three potential mechanisms responsible for driving the transition from the Ordered fiber (OrF) to the Chain Link (CL) structures: the electrostatic energies of configurations of the field induced dipoles and monopoles, electrophoretic forces acting on charges in the fibers separated by the field and constrictive forces from currents running through the

fibers.

5.9.1 Competition between induced dipoles and electrostatic monopoles

We consider the induced electric dipoles on the ellipsoids (q_1) and the particle charge (q_0) (Figure 5.10). Simply replacing each particle with a dipole, the aligned pairs of particles in the CL structure are energetically disfavored. However, if the dipoles are sufficiently off center, such that the particle geometry results in an interaction strength of ϵ_1 between bonded particles in both the candidate CL and SC structures, then the CL structure may be energetically stable ($U_{CL} \approx 2\epsilon_0 - 2\epsilon_1 + \epsilon_2$ and $U_{SC} = \epsilon_1$). For this mechanism to be plausible the magnitude of the induced dipole must be as large as the particle charge, q_1 . We estimate the total amount of charge q_0 on the ellipsoids from the zeta-potential[159] measurements of the uncoated ellipsoids and find that each ellipsoid contains a net -10^{-14}C of excess charge. To estimate an upper bound of the magnitude of q_1 we compute the amount of mobile charges on the gold patch of an ellipsoid. We find $4.3 \times 10^{-10}\text{C}$ of mobile electrons per ellipsoid, with each gold atom contributing 1 free electron. Thus, the induced charge can compete with monopole repulsion, and can dominate it.

The position of the particles' net dipole could be shifted out from the particle center of mass as a function of frequency and salt concentration due to double layer polarization being out of phase with the field [160]. In such a scenario, the dipole would be closer to the center of mass at lower salt concentrations and stabilize the SC structure while a larger double layer polarization could shift the dipole moment further off-center and stabilize the

CL structure.

5.9.2 Force driven compression of Janus ellipsoid chains

We modeled the AC-field assembly behavior with Brownian dynamics by including coarse grain terms to model proposed mechanisms for chain elongation. We apply an aligning torque of 8.0 in reduced units to simulate the alignment of the ellipsoids with the external field. We model the polarization of the Janus ellipsoids with two Gaussian patches of depth $\epsilon = 10$. To model magnetic compression, an ordered fiber is axially compressed by a force of magnitude 40 (2pN per particle), causing the chain to extend. To model the chain stretching by charge accumulation at the ends of chains, an external force of magnitude 10pN is applied to each ellipsoid at the end of the ordered fiber. Both the radial compression and axial stretching induced actuation of OrF into CL structures at $\kappa^{-1} = 0.15$ and $T = 0.211$ (Figure 5.9). With only field-dipole interactions and dipole-dipole interactions, we observed the SC structure to be stable at $\kappa^{-1} = 0.45$ and $T = 0.211$.

5.9.2.1 Current induced compressive forces

We note that there exists a conducting channel through the center of the fibers in the self-assembled OrF phase as all the gold patches are in contact. As the field oscillates, current is driven through the experimental chamber and through the fibers. The current flowing through the wire will constrict the fiber. An axial compression of roughly 2pN units applied to each particle was sufficient to produce elongation in simulations. We approximate the

order of magnitude of current required to produce this force by crudely modeling a 5-link ordered fiber as two parallel wires, $l = 15\mu\text{m}$ in length, and separated by $d = 0.5\mu\text{m}$. The current required to produce a force $F = 10\text{ pN}$ between these two wires is

$$I = V \frac{\rho \mu F d}{\mu_0 L} \quad (5.5)$$

yielding $I \approx 1\text{mA}$. Within the experimental cell, the D-field is 10kV/m . We estimate the potential difference across the wire as $\delta\phi = lD = 0.15\text{V}$. Computing the resistance of the fibers using the bulk conductivity of gold ($\sigma = 2.44 \times 10^{-8}\text{S/m}$) and the dimension of the particle coatings ($30\text{nm} \times 0.5\mu\text{m}$) we find that a $15\mu\text{m}$ fiber could carry a current of $\approx 1\text{mA}$. Thus, it is plausible that the AC current running through the wire may contribute to its elongation. However, estimates of the geometry of the gold coating and the interfaces between ellipsoids may significantly affect the resistance³⁶ and the amount of heat dissipated make this an unlikely primary mechanism.

5.9.2.2 Electrophoretic forces of elongation

Finally, we estimate the magnitude of the electric charge excess that would be required to elongate the fibers. In this scenario, we consider electrophoretic forces acting on the mobile charges from the gold coating that separated along the length of fibers by the applied field. From simulations, we know that adding a force of equivalent to 10 pN that pulls the fiber ends is sufficient to elongate the fibers. We hypothesize that the chains reach their extended length when the electrophoretic force acting on the surplus accumulated charge equals the

restoring force. In a field of $D=10\text{kV/m}$, a force of this magnitude requires that $10^{-13}C$ of charge has accumulated on the end ellipsoids[159]. Each ellipsoid has the $4.3 \times 10^{-10}C$ that can separate and is thus an upper bound on q_1 . Thus, this mechanism is plausible in the parameters of this experiment.

5.10 Outlook

The self-assembly of one-dimensional, ordered and self-limiting colloidal fibers from Janus ellipsoid patchy particles that can be reconfigured rapidly on application of AC electric fields thus results in the formation of functional shape-memory colloidal assemblies. Self-assembled structures that can be actuated by external stimuli, such as shown here, could find use as colloidal actuators with muscle-like function, for applications such as soft robotics. These experiments also show the possibility of generating unique, functional structures in other colloidal systems by exploiting the interplay between self-assembly forces and external fields for a new set of functional colloidal materials.

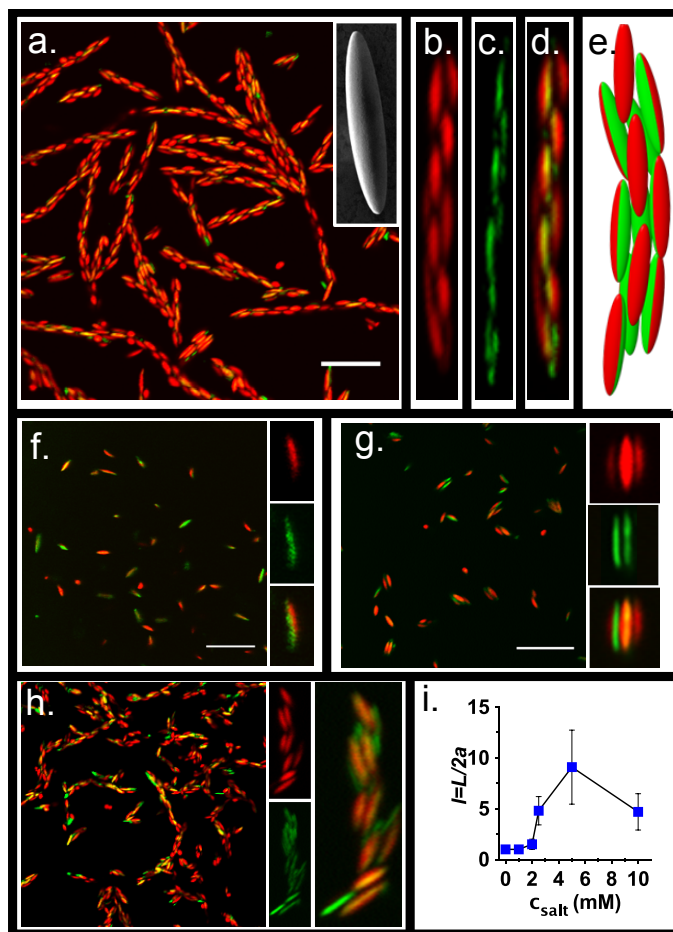


Figure 5.1: Janus ellipsoid self-assembly at different NaCl concentrations. a. CLSM image of Janus ellipsoids (aspect ratio $r = 5$) suspended in 5 mM NaCl in DI water. Scale bar: $10\mu\text{m}$. Inset scanning electron microscopy (SEM) of a Janus ellipsoid. Scale bar: $0.5\mu\text{m}$. b. Close-up of the fluorescence-imaging channel for one assembled Janus ellipsoid fiber. c. Close-up of the reflection-imaging channel for one assembled Janus ellipsoid fiber. d. Composite channel that combines both the fluorescence and reflection channels. Red is the uncoated, fluorescent polymer half of the particle. Green is the gold and chrome coated part of the particle. e. Computer generated rendering of Janus ellipsoid assembled fiber. f. CLSM image of Janus ellipsoids (aspect ratio $r = 5$) suspended in DI water without salt. Scale bar: $10\mu\text{m}$. Inset shows the fluorescence, reflection and composite channels of one such Janus ellipsoid. g. CLSM image of Janus ellipsoids (aspect ratio $r = 5$) suspended in 1 mM NaCl salt in DI water. Scale bar: $10\mu\text{m}$. Inset shows the fluorescence, reflection and composite channels of one Janus ellipsoid cluster. h. CLSM image of Janus ellipsoids (aspect ratio $r = 5$) suspended in 10 mM NaCl salt in DI water. Scale bar: $10\mu\text{m}$. Inset shows the fluorescence, reflection and composite channels of one such disordered fiber. i. The dimensionless fiber length (l) as a function of salt concentration (c_{salt}) is reported for Janus ellipsoids (aspect ratio $r = 5$). Experiments, microscopy and image analysis conducted by Aayush Shah and Wenjia Zhang; renderings and image analysis by Benjamin Schultz.

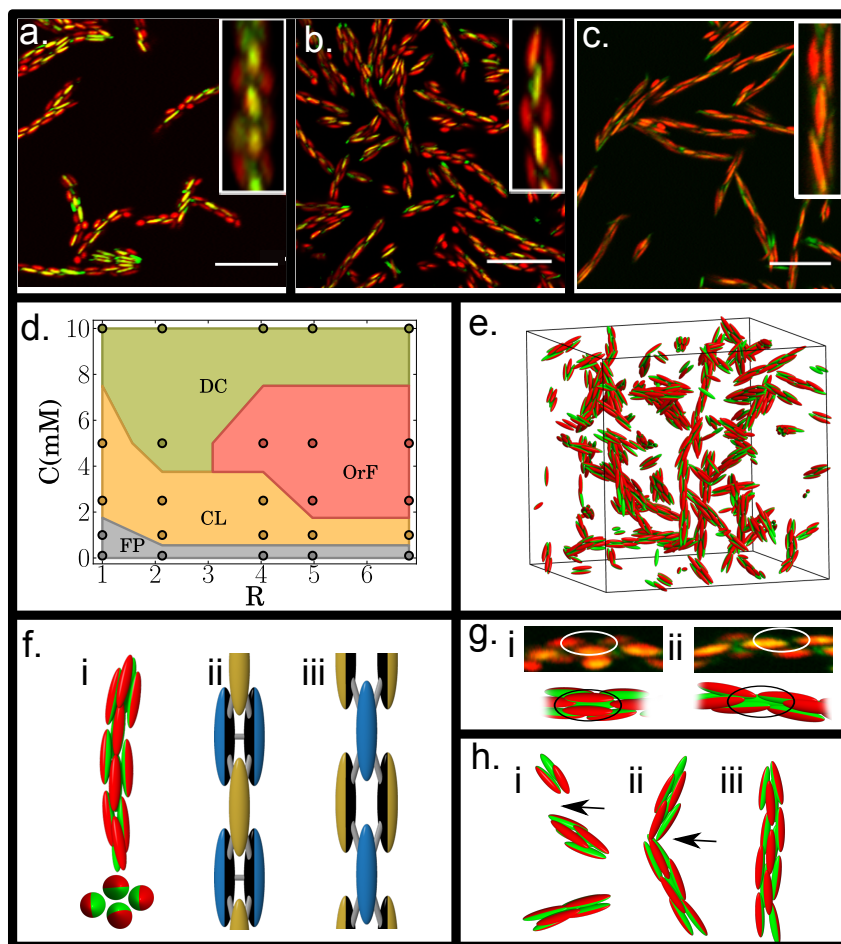


Figure 5.2: Phase diagram of Janus self-ellipsoid assembly and mechanism of Janus ellipsoid assembly. a., b., c. CLSM image of an ordered fiber (OrF) for aspect ratio $r = 4.1$, 5.0 and 6.8 Janus ellipsoids respectively. Scale bar: $10\mu m$. Inset image reports the close-up view of one such fiber. d. Phase diagram of assembled phases of Janus ellipsoids as a function of their aspect ratio and salt concentrations. Disordered fibers (DiF) Close-packed cluster (CLC), free particles (FP) and ordered fibers (OrF) e. Simulation study of the assembly of 1000 ellipsoids into the OrF ordered phase. f. i) shows a close-up view of an ordered fiber and its cross section. ii) and iii) show the contact network in this one dimensional structure. g. Two primary defect types, including the addition of an extra particle and the displacement of a particle from the unit cell are observed in experiments (CLSM images) and simulations (renderings). h. Kinetics of fiber formation by the combination of clusters is depicted through simulation snapshots. Experiments and microscopy conducted by Aayush Shah and Wenjia Zhang. Simulations were conducted by Benjamin Schultz. Structural analysis of experimental and simulation data by Benjamin Schultz and Aayush Shah.

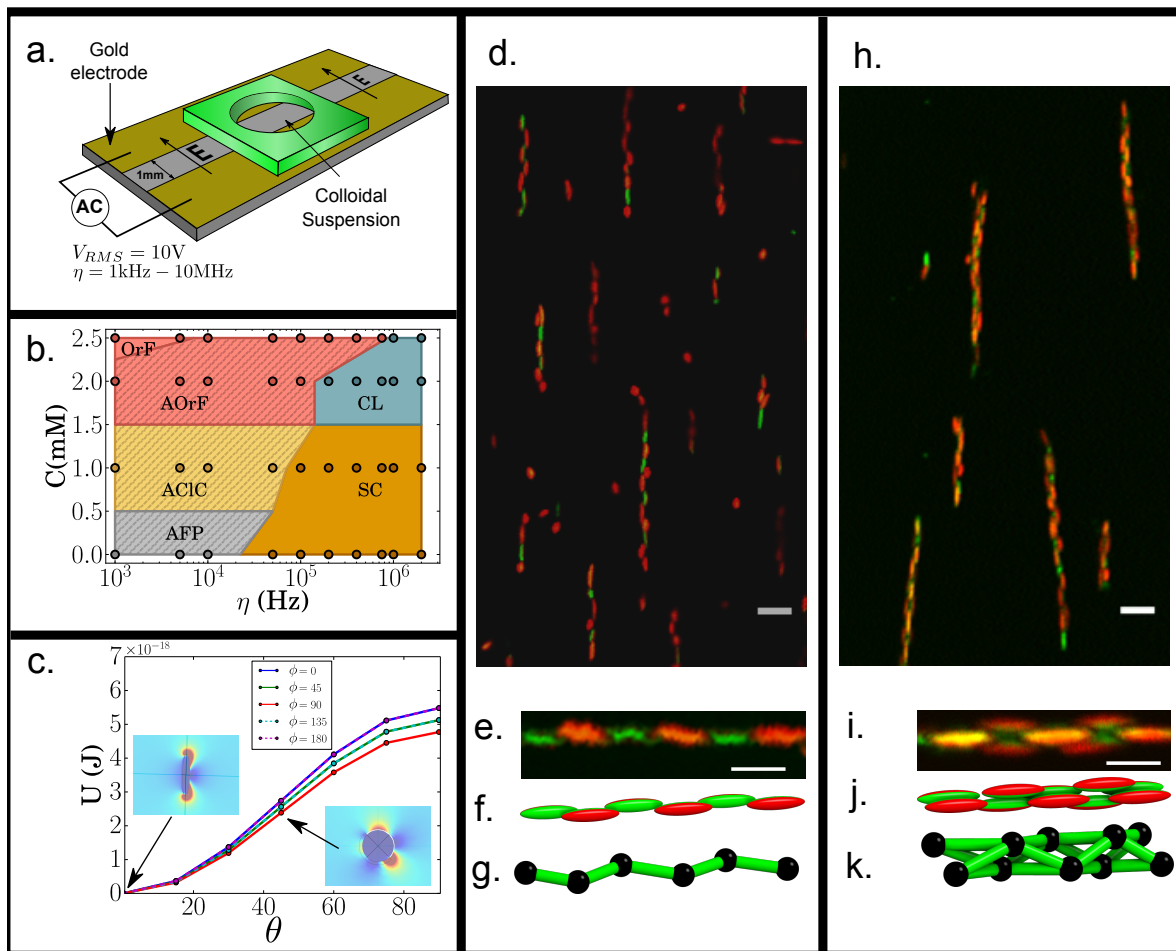


Figure 5.3: AC electric field assisted assembly of Janus ellipsoids. a. Schematic of AC electric field device. b. Phase diagram of assembly phases of Janus ellipsoids upon application of 10 V_{rms} AC electric field as a function of salt concentration and frequency. c. COMSOL simulations of a single Janus ellipsoid for polar angle ϕ and azimuthal angle θ , showing their tendency to align with an external field. d. Zoomed-out CLSM image of staggered chain (SC) assembly structure. Scale bar: $5\mu\text{m}$. A close-up view of one of the chains (Scale bar: $3\mu\text{m}$) along with the corresponding rendering and the ball-stick bond diagram are also shown. e. Zoomed-out CLSM image of stretched chain-link (CL) assembly structure. Scale bar: $5\mu\text{m}$. A close-up view of one of the fibers (Scale bar: $3\mu\text{m}$) along with the corresponding rendering and the ball-stick bond diagram are also shown. Experiments, microscopy and image analysis conducted by Aayush Shah and Wenjia Zhang; FEA calculations, renderings and image analysis by Benjamin Schultz.

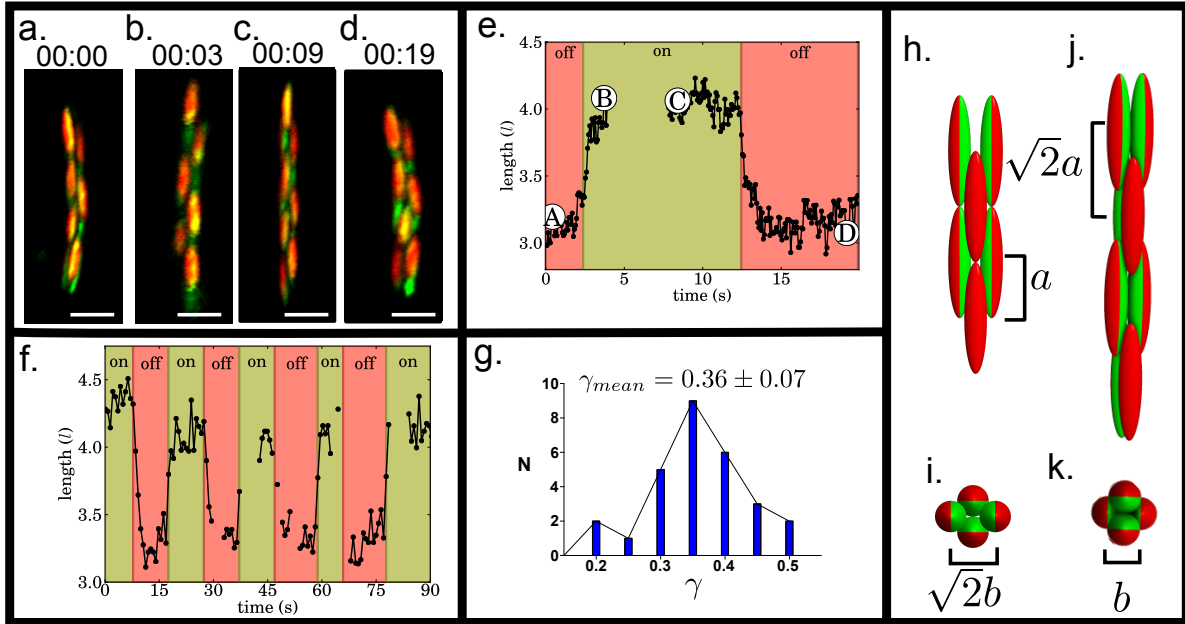


Figure 5.4: Actuation of Janus ellipsoid fibers using AC electric fields. Close-up view of Janus ellipsoid fibers a. Ordered fiber before application of AC electric field (Scale Bar: $3\mu m$). b.,c. Chain link (CL) structure upon during application of AC electric field. (10 Vrms, 1 MHz) d. Ordered fiber after application of AC electric field. e. Dimensionless fiber length (l) as a function of time on application of AC electric fields. f. Dimensionless fiber length (l) as a function of time on switching the AC electric field on - off. g. Distribution of the strain in the fiber length on application of AC electric fields for a number of fibers with varied lengths. h.-i. Rendering of the OrF structure and its rhombic cross section respectively. j.-k. Rendering of the CL structure and its square cross section respectively, showing the maximal strain possible under geometric constraints. Experiments and microscopy conducted by Aayush Shah and Wenjia Zhang; structural analysis by Benjamin Schultz.

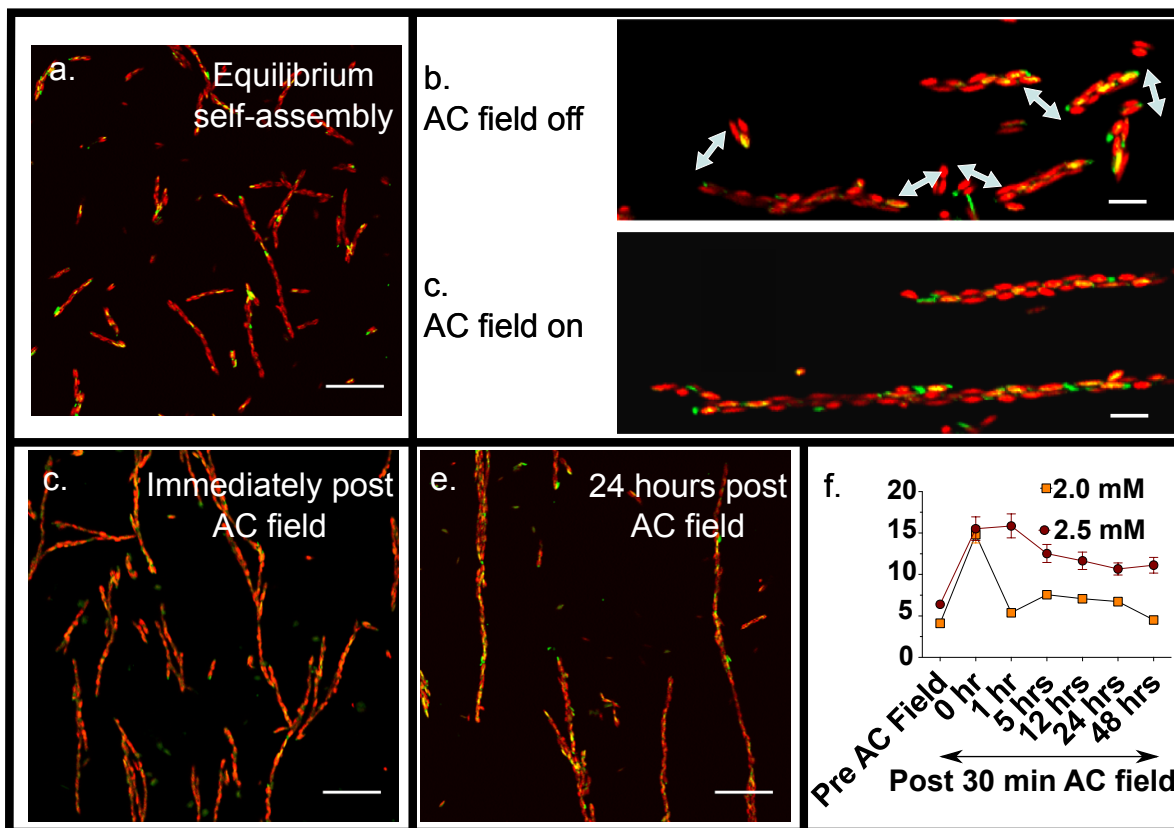


Figure 5.5: Changes in Janus fiber length by AC electric fields. a. CLSM image of Janus ellipsoids of aspect ratio five suspended in 2.5 mM NaCl in DI water. Scale bar: $20\mu m$. b., c. Close-up view of Janus ellipsoid assembly before and during application of AC electric fields, respectively. d. CLSM image immediately after application of AC electric fields for 30 mins. e. CLSM image 24 hours after application of AC electric fields. f. Dimensionless fiber length of Janus ellipsoid assemblies at 2 mM and 2.5 mM salt concentrations as a function of time. Experiments and microscopy conducted by Aayush Shah and Wenjia Zhang.

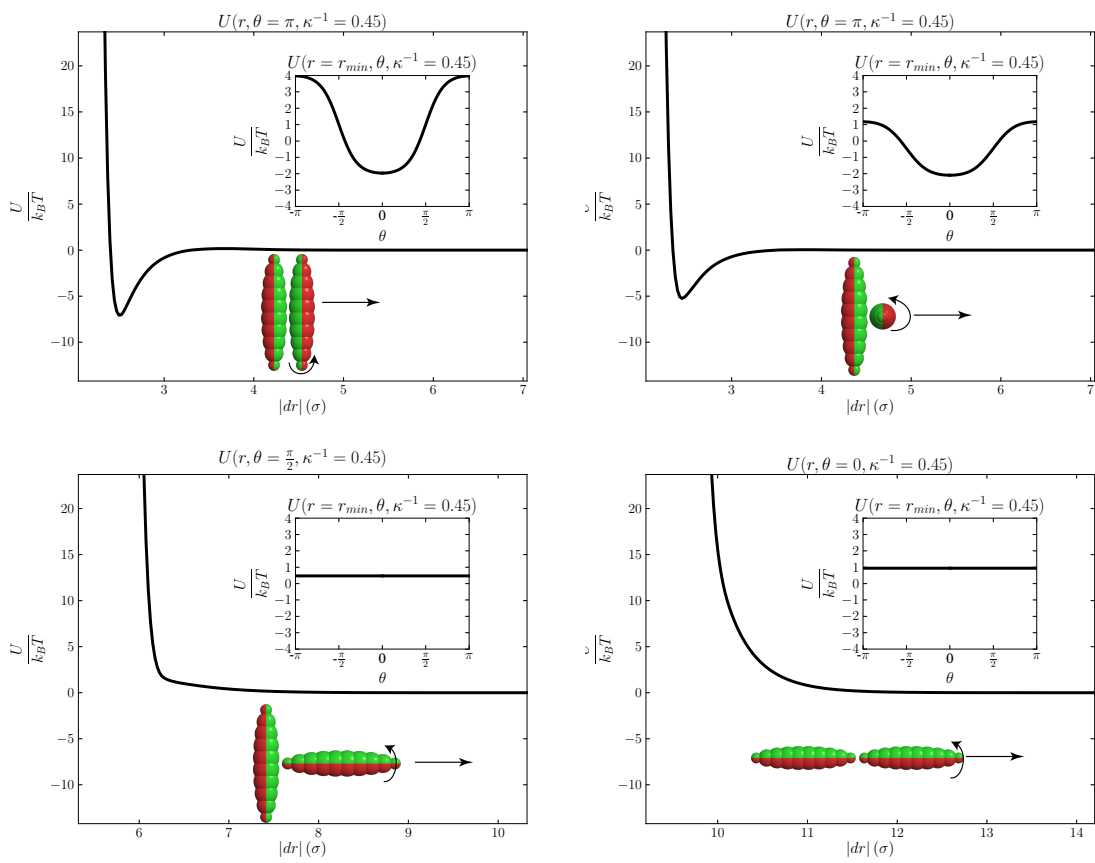


Figure 5.6: Plots of the anisotropic potential used for simulations at 1.0 mM NaCl.

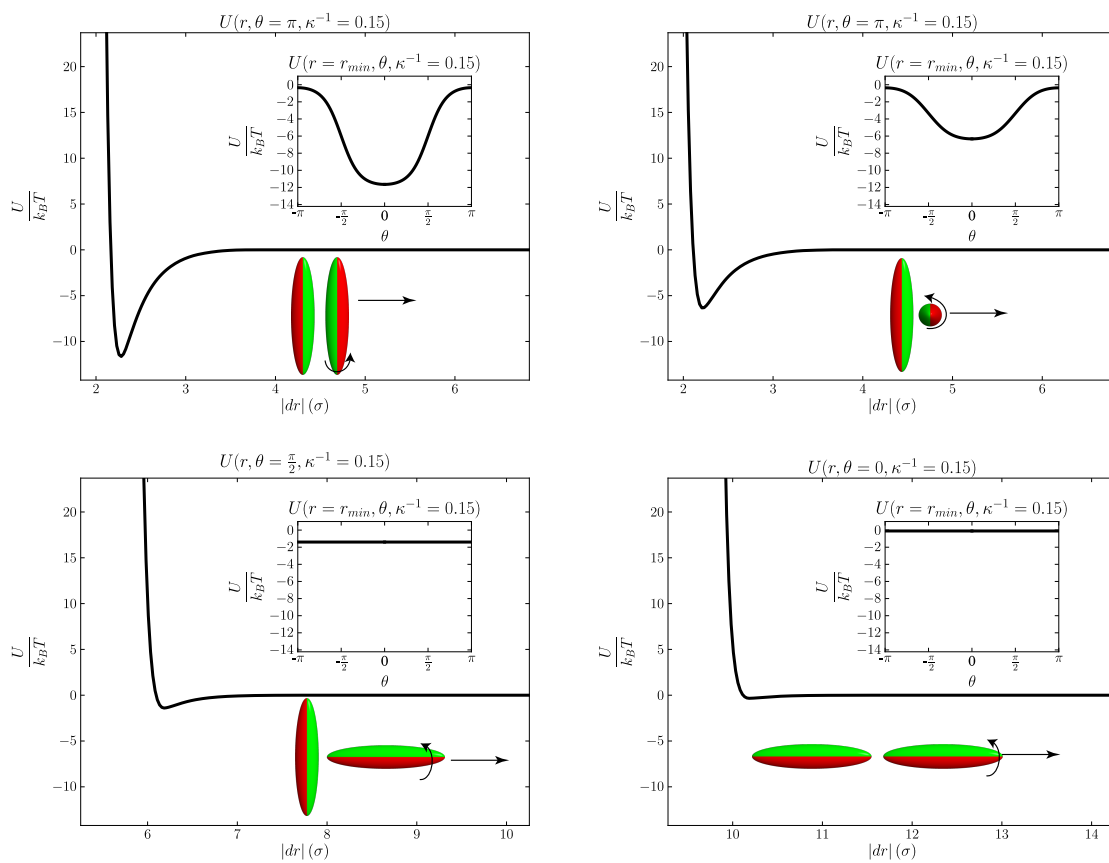


Figure 5.7: Plots of the anisotropic potential used for simulations at 2.5 mM NaCl.

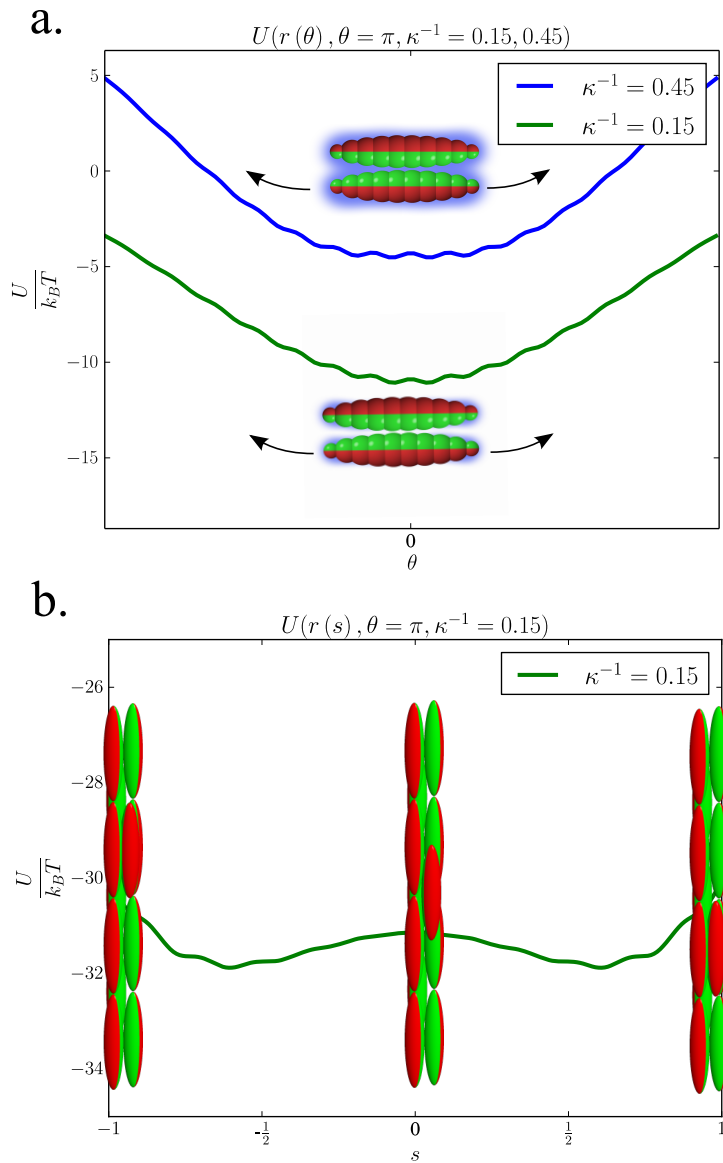


Figure 5.8: Plot of the interaction energies for (a.) parallel particles as a function of offset angle and (b.) along the axis of an ordered fiber.

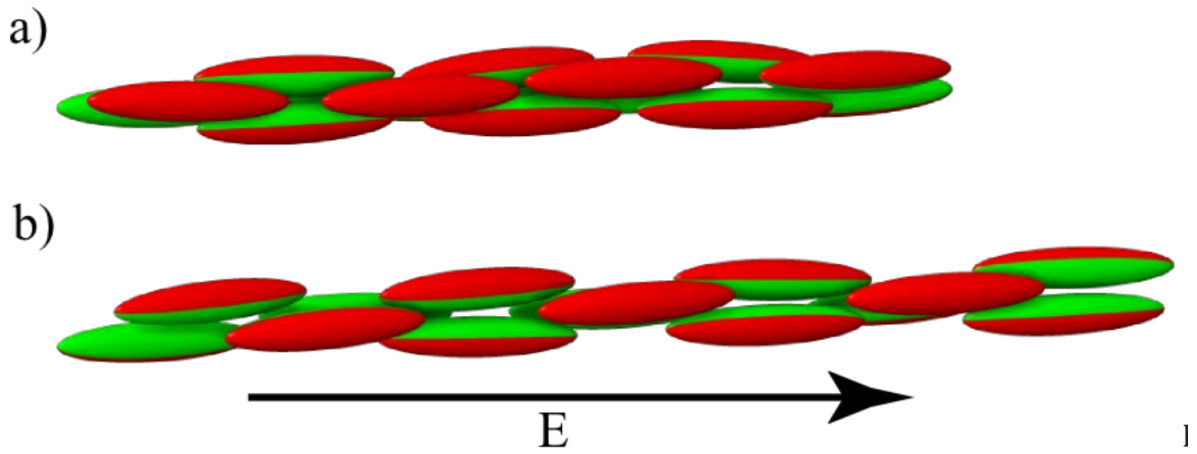


Figure 5.9: a). An ordered fiber (OrF) structure stabilized without an external field. b) Circle-link (CL) structure reconfigured from the OrF pictured in a) upon the application of an external field. The field is simulated by adding an aligning torque to each particle (field-dipole interaction), a magnetic compression (to simulate AC current along the fiber) and positive and negative patches at the tips of the ellipsoids.

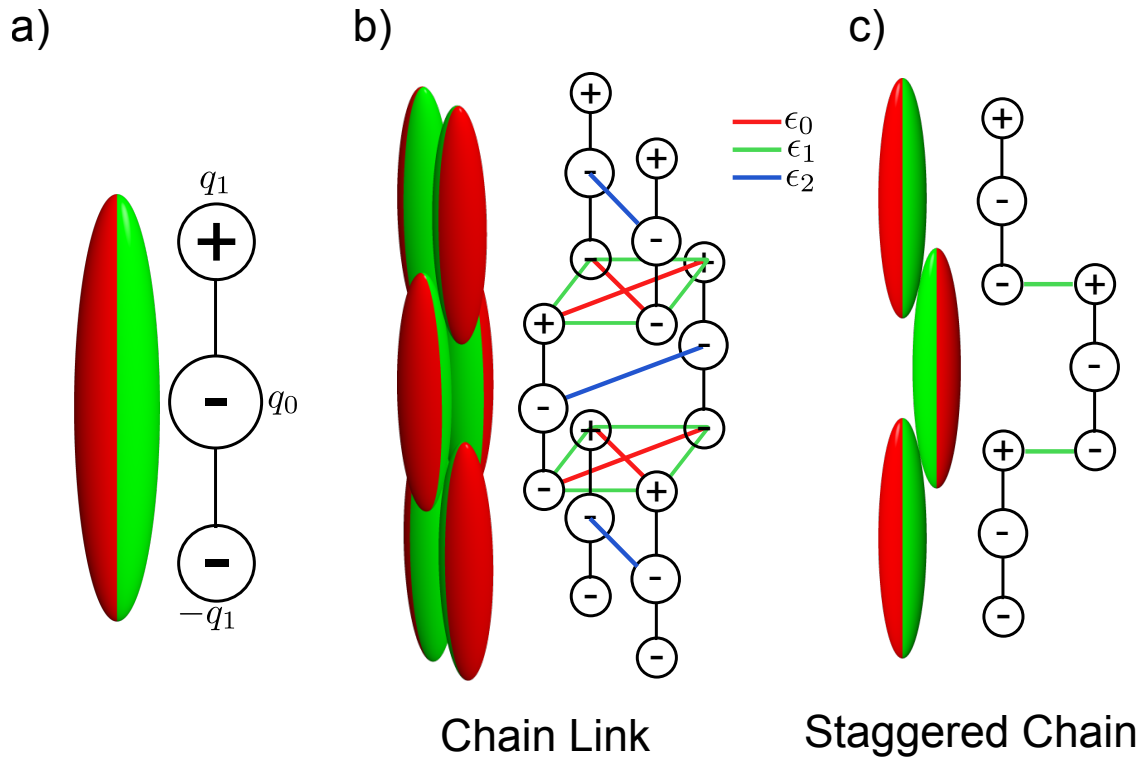


Figure 5.10: Schematics of the electrostatic interactions in the CL and SC structures.

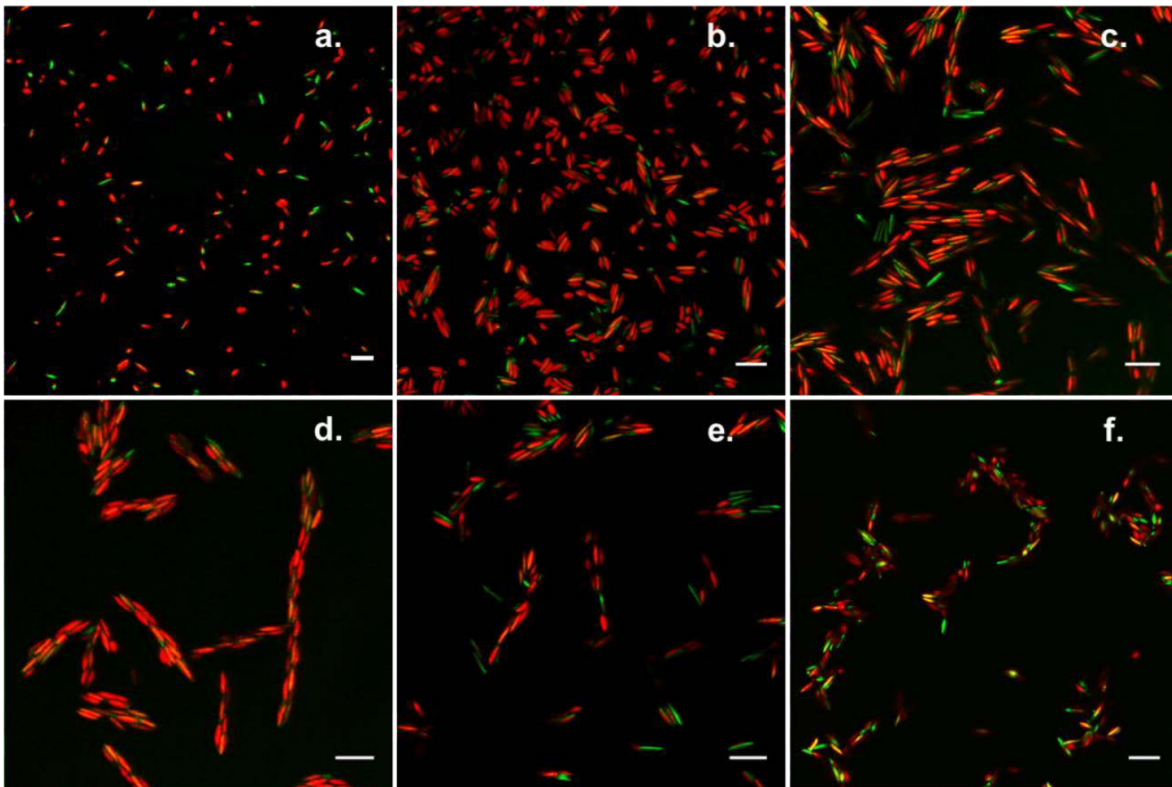


Figure 5.11: CLSM images of carboxylate-stabilized ellipsoid ($r = 5$) self-assembly. Salt concentrations (NaCl concentrations) are: a. 0 mM, b. 1mM, c. 2mM, d. 2.5mM, e. 3mM, f. 5mM. Scale bars are $5\mu m$. Experiments and microscopy conducted by Aayush Shah and Wenjia Zhang

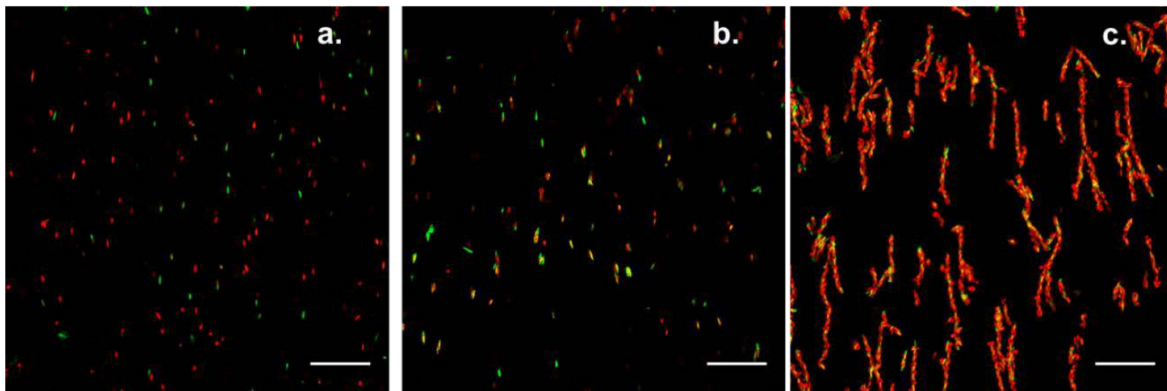


Figure 5.12: a. Aligned free particle phase (AFP) b. Aligned close packed cluster phase (ACIC) c. Aligned ordered fiber phase (AOrF). Scale Bars are $20\mu m$. Experiments and microscopy conducted by Aayush Shah and Wenjia Zhang

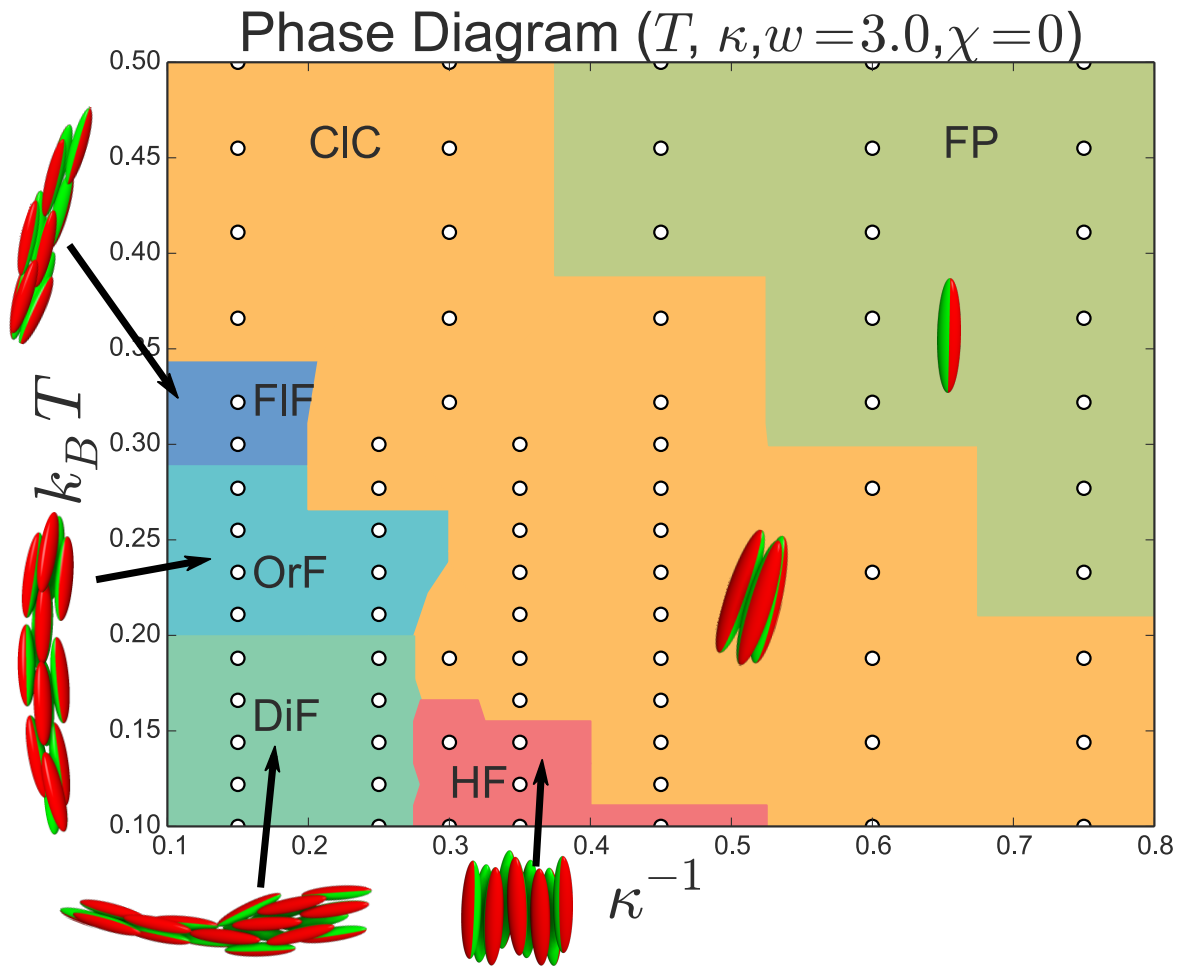


Figure 5.13: Phase diagram in temperature and screening length. The observed phases are free particles (FP), close-pack clusters (CIC), Fluid fibers (FIF), Ordered fibers (OrF), Disordered fibers(DiF), and Horizontal fibers(HF). Clusters extracted from each phase are pictured in the phase diagram. The phases observed in this diagram are the fluid fibers and the horizontal fibers.

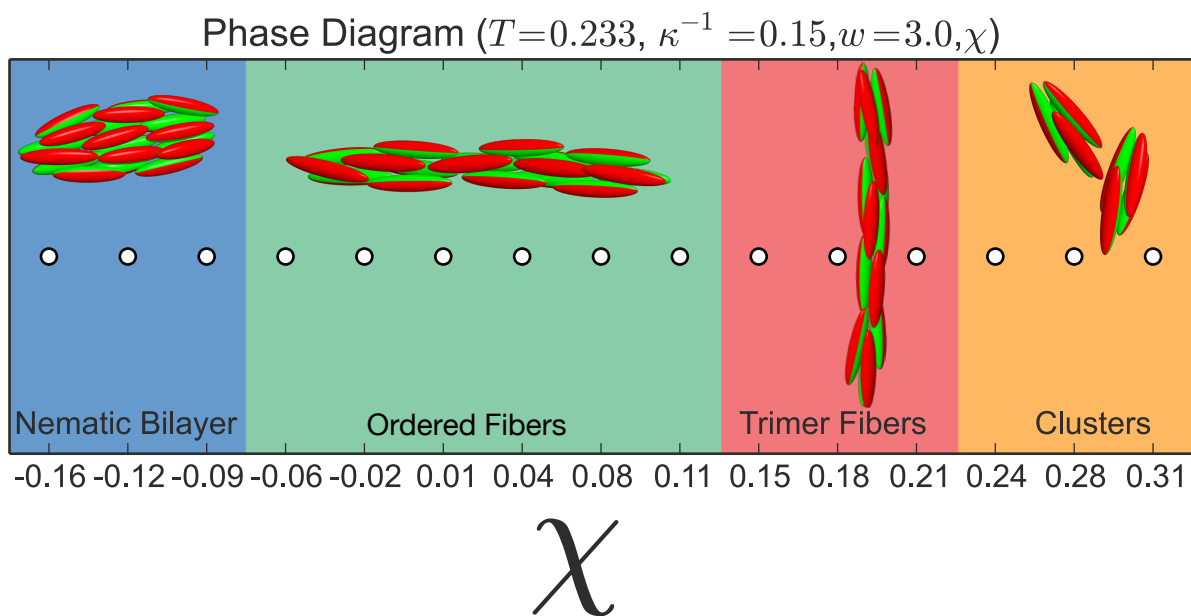


Figure 5.14: Phase diagram of model as a function of χ , which describes the Janus balance of the particles. $\chi = 0$ corresponds to particle with 50% Janus balance; half of their surface area is covered by the patch. If $\chi < 0$ more than half of the particle surface is covered by the patch.

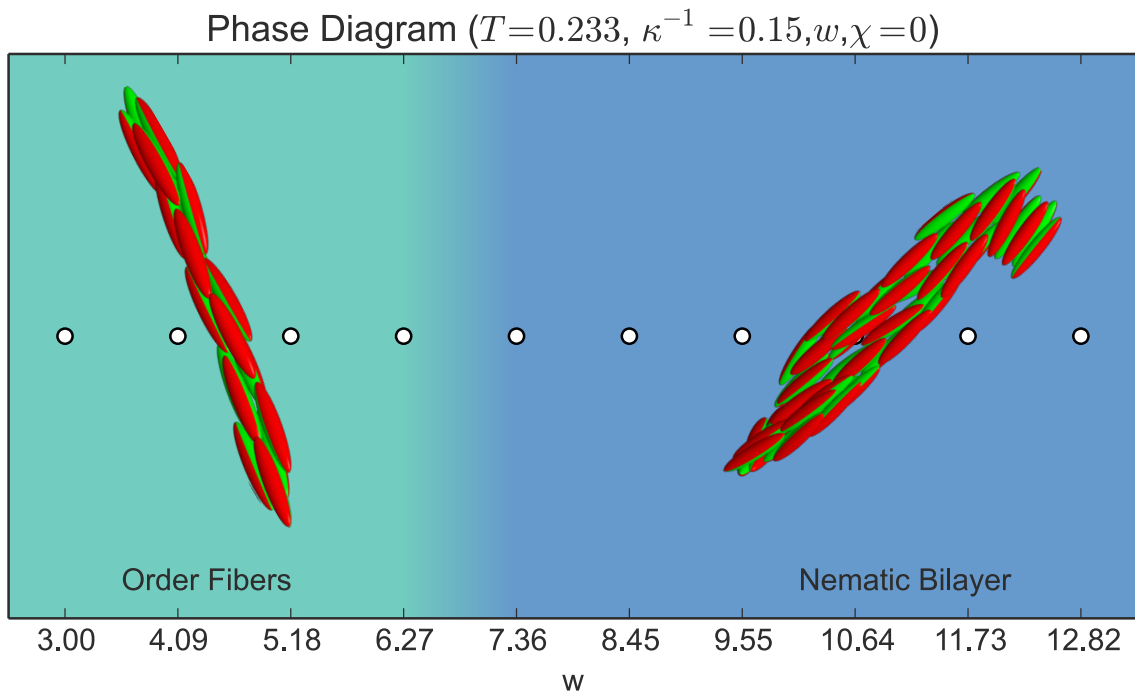


Figure 5.15: Phase diagram of particle model as a function of w . w describes the steepness of the sigmoidal angular modulation of the potential. For reference, a $w=3.0$ potential is plotted in Figures 5.6 and 5.7. As w increases, the angular potential approaches a square well. For $w < 6.27$, ordered fibers self-assemble. For $w > 7.37$, we find that adjacent fibers coalesce into bilayer clusters, consistent with bilayer formation for perfect square well potentials of Janus spheres[161] and spherocylinders[137]

Chapter 6

Outlook

This work has described the role of particle shape in self-assembly of colloidal materials in several example systems. Shape is just one of the many available anisotropy dimensions that can be used for colloidal design[14]; understanding how it affects assembly on its own, and in combination with interactions described by other anisotropy dimensions maximizes its utility in the design of colloid particles.

In chapter 2, design limits with only entropic interactions were presented and our understanding of how densest packing structures can differ from self-assembled ones[59] is further refined. In particular, we identified several forms of entropy (arising from orientational and occupational degeneracies) that stabilize non-densest packing structures under thermodynamic self-assembly. By understanding the origin of the thermodynamic driving forces behind the observed assemblies, we can employ negative design to engineer particles away from these structures by inhibiting these degeneracies. Alternately, one may

exploit these entropic forces to design model systems of orientational (and occupational) "glasses" [162].

The work shown in chapter 3 describes methods that are critical for connecting experimental explorations of the shape anisotropy dimension to theoretical and computational ones (as in chapter 4). Theory and simulation can predict how particle shape can influence thermodynamic and self-assembly behavior, but as is always the case, experiments are the ultimate test. Thus, having a general purpose tool to extract arbitrarily shaped particles from confocal image volumes will be critical in refining our models of anisotropic colloids and establishing a quantitative connection between experiments and simulations along the shape anisotropy dimension.

This tool is first applied in chapter 4 to study the self-assembly of oblate spheroids in solution with large polymer depletants. Several computational studies [97] suggested that oblate spheroids with an aspect ratio of 0.5 could self-assemble into chiral bundles. We fabricated such spheroids, and studied their self-assembly under the closest experimental conditions to these studies we were able to achieve, finding instead the particles assembled into arrested thread-like clusters. We characterized the local clustering using our particle identification codes, and show semi-quantitative agreement with new, idealized MC simulations, both showing kinetic arrest into single-article wide fibers. We are able to attribute this arrested structure to the form of the attractive, emergent interaction between the colloids, dictated by particle shape. This understanding sets the stage for a modified particle designed to assemble chiral bundles.

In chapter 5, we discuss how, in a system dominated by anisotropic enthalpic interaction, shape comes to play a critical role in its reconfigurability and thus utility as a colloidal device. While recreating atomic crystal structures at the nano and colloid scale has its set of interesting applications[136, 163], the large design space of colloids opens up the possibility of active and functional materials [42, 41]. We fabricated and study the self-assembly of prolate Janus spheroids, which form ordered, one-dimensional fibers that can be actuated by the application of external electric field. The particle shape, coupled with the electronic response to the field, permits the reversible reconfiguration. Actuation is a critical element in designing functional colloidal devices; these fibers can find application as a component of, for example, a swimming colloidal "robot." As the line between materials and devices blurs, the role of the material building blocks' arguably simplest characteristic - their shape - remains critical in determining both its assembly's structure and functionality.

Appendix A

Thermodynamic integration of hard anisotropic particles

A.1 Abstract

One frequent goal of running equilibrium thermodynamics simulations is to determine the free-energy minimizing phase or structure at a given state point. Often, the simulator has limited knowledge about what structures their particles are capable of forming. In that case, we are left to start our system in a disordered state and let the equilibrium state self-assemble. In many cases, this is sufficient, but in others our system may fall out of equilibrium or become non-ergodic (e.g., we want to know the stable phase of a system of hard particles at a high packing fraction).

In such cases, we can often use techniques designed to directly compute the

free-energy of a library of candidate structures and identify the thermodynamic state by direct comparison of the relative free energies of these structures. This, of course, only works if we have some idea of the structures or phases a particle may self-assemble. For hard particles, such candidate structures can be generated from densest packings, constructed by hand, or taken from equilibrium simulations at different state points.

In the following sections I will focus on Frenkel-Ladd integration for hard particles, which is a particular type of thermodynamic integration suited for comparing the relative free energies of different crystal structures. Like all thermodynamic integration methods, it relies on computing a reversible path integral between two state points. The value of this integral provides a relative free energy difference between the beginning state and the end state.

A.2 Frenkel-Ladd thermodynamic integration for hard spheres

The crux of Frenkel-Ladd integration is that we want to transform our system (a crystal of truncated tetrahedra for example) into a reference system for which we can analytically compute the free energy (a noninteracting set of harmonic oscillators)[13]. We can compare the free energies of competing crystal structures by taking a path integral from each crystal structure to a common reference state.

For hard spheres of diameter D , one may accomplish this by attaching a spring

to each particle that tethers it to an arbitrary position. Our original Hamiltonian is

$$H(\{\vec{r}_i\}) = \sum_{i=0}^N \sum_{j=i+1}^N U_{HS}(r_{ij}) \quad (\text{A.1})$$

where \vec{r}_i is the position of particle i , N is the number of particles, $r_{ij} = |\vec{r}_i - \vec{r}_j|$ and

$$U_{HS}(r) = \begin{cases} \infty & : r \leq D \\ 0 & : r > D \end{cases}$$

We introduce a spring with a coupling constant γ that tethers particle i to $\vec{r}_{i,0}$. Our Hamiltonian becomes

$$H(\{\vec{r}_i\}) = \sum_{i=0}^N \left[\gamma \epsilon \left(\frac{|\vec{r}_i - \vec{r}_{i,0}|}{\sigma} \right)^2 + \sum_{j=i+1}^N U_{HS}(r_{ij}) \right] \quad (\text{A.2})$$

where γ is a unit-less constant, $\epsilon = 1$ is a reduced energy unit and $\sigma = 1$ is the reduced distance unit. For brevity, we define

$$U_{FL} \equiv \sum_{i=0}^N \epsilon \left(\frac{|\vec{r}_i - \vec{r}_{i,0}|}{\sigma} \right)^2. \quad (\text{A.3})$$

The set $\{\vec{r}_{i,0}\}$ are, in principle, arbitrary. Along our path of integration however, we will increase γ to ∞ , so we require that the $\{\vec{r}_{i,0}\}$ describe a non-overlapping configuration. From a practical standpoint, we always select the equilibrium crystal positions for $\{\vec{r}_{i,0}\}$; this guarantees a non-overlapping configuration and a thermodynamic path

that is easy for our simulation to follow.

With γ now introduced, we can take a reversible thermodynamic path from our original system of hard spheres $\gamma = 0$ to a system of decoupled harmonic oscillators as $\gamma \rightarrow \infty$ - the particles are bound so tightly to their lattice sites that they never venture far enough to bump into each other. The difference in free energy of the Einstein crystal and our target system is

$$F_{Einstein} - F = \int_0^\infty d\gamma \left. \frac{\partial F}{\partial \gamma} \right|_{N,V,T} \quad (\text{A.4})$$

This of course, begs the questions of how to compute $\left. \frac{\partial F}{\partial \gamma} \right|_{N,V,T}$. With Z defined as the canonical partition function, we note:

$$\left. \frac{\partial F}{\partial \gamma} \right|_{N,V,T} = -k_B T \frac{1}{Z} \left. \frac{\partial Z}{\partial \gamma} \right|_{N,V,T} \quad (\text{A.5})$$

where

$$\begin{aligned} Z &= \int \prod_{i=0}^N \mathbf{dr}_i^3 \mathbf{dp}_i^3 \exp(-\beta H') = \int \prod_{i=0}^N \mathbf{dr}_i^3 \mathbf{dp}_i^3 \exp(-\beta (H + \gamma U_{FL})) \\ \left. \frac{\partial Z}{\partial \gamma} \right|_{N,V,T} &= - \int \prod_{i=0}^N \mathbf{dr}_i^3 \mathbf{dp}_i^3 \beta U_{FL} \exp(-\beta H') \\ \left. \frac{\partial F}{\partial \gamma} \right|_{N,V,T} &= \frac{1}{Z} \int \prod_{i=0}^N \mathbf{dr}_i^3 \mathbf{dp}_i^3 U_{FL} \exp(-\beta H') = \langle U_{FL} \rangle_{N,V,T,\gamma} \end{aligned} \quad (\text{A.6})$$

Thus, we can compute $\left. \frac{\partial F}{\partial \gamma} \right|_{N,V,T}$ by computing the ensemble average of U_{FL} in our simulations for $\gamma = 0$ to $\gamma = \infty$ and integrate $\langle U_{FL} \rangle_{N,V,T,\gamma}$.

In practice, we cannot evaluate $\gamma = \infty$; we run simulations for a range of γ

and stop when $\langle U_{FL} \rangle$ plateaus and obeys the equipartition theorem.

Frenkel-Ladd thermodynamic integration for hard particles with shape

To extend the preceeding framework to find the free energy of crystals made of hard shapes, we introduce an additional spring to each particle in our harmonic potential[28]:

$$U_{FL} = \sum_{i=0}^N \gamma \epsilon \left(\frac{|\vec{r}_i - \vec{r}_{i,0}|}{\sigma} \right)^2 + \alpha \epsilon |\vec{q}_i - \vec{q}_{i,0}|^2 \quad (\text{A.7})$$

where \vec{q}_i are the orientations of each particle and $\vec{q}_{i,0}$ are the equilibrium orientations of each particle. As $\alpha \rightarrow \infty$ and $\gamma \rightarrow \infty$, we now have an Einstein crystal that has up to six degrees of freedom. As before, we wish to reversibly transform our system to this Einstein crystal and integrate to find the work required to perform this transformation, which is equivalent to the free energy difference.

$$F_{Einstein} - F = \int_0^\infty d\vec{s}(\gamma, \alpha) \left. \frac{\partial F}{\partial \vec{s}} \right|_{N,V,T} \quad (\text{A.8})$$

In practice, we choose a path \vec{s} along which $\alpha = C\gamma$, where C is a constant (10 has worked well in previous works[28]). This constant is chosen such that the transformation of hard particle to harmonic oscillator happens for rotational and translational degree of freedom at similar values of γ .

Now, if we wish to compare the free energy of a hard-particle crystal computed

via Frenkel Ladd integration with the free energy some other method, or the free energy of another shape we must compute the free energy of the Einstein crystal analytically as a common reference for the free energy. See Frenkel and Smit [13] for the expression for spherical particles and Haji-Akbari et al. [28] for the expression for non-spherical particles.

If a spring acting on quaternions is used, as described here, one must correct for the degeneracy of the quaternion representation of rotations subtracting $Nk_B T \ln(2)$. If the shape has a rotational symmetry of order N_R , a similar shift to the free energy of magnitude $-Nk_B T \ln(N_R)$ must be added to account for the identical particle orientations.

Frenkel-Ladd integration with degenerate crystals

One case that requires special consideration is the comparison of a crystal with orientational degeneracy to one without orientational degeneracy. In a crystal with orientational degeneracy, each particle can equivalently occupy its lattice site at one of N_R orientations.

In practice, we choose one instance of the degenerate crystal and then introduce terms in the Hamiltonian that depend on those particular particle orientations. Since we have introduced terms in our Hamiltonian that now make certain states distinguishable from those which would have been considered equivalent in our original system, we must introduce a correction when we compute the free energy. Failing to do so, we would underestimate the latent heat of melting from an orientationally ordered crystal at high density to an orientationally degenerate crystal at lower density.

In the simplest of cases, each particle's orientation is completely independent

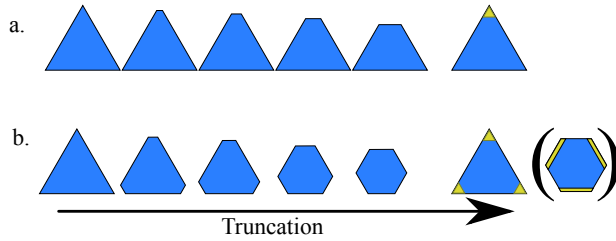


Figure A.1: Family of singly and triply truncated triangles

of its neighbors and there are N^{N_R} instances of the orientationally degenerate crystal for each instance of the orientationally ordered one; a net addition of $N \ln(N_R)$ of entropy. This entropy can be quite significant in stabilizing orientationally degenerate structures over orientationally ordered ones. Figure 2.3 shows how orientational degeneracy stabilizes an orientationally degenerate diamond crystal relative to a space-filling hexagonal diamond configuration to a very high density of $\phi_p = 0.78$.

Frenkel-Ladd calculations in shape ensembles

Considering the comparison of free energies between orientationally degenerate and orientationally ordered crystals computed via Frenkel-Ladd integration gives us a good starting point to consider the comparison of free energies of different shapes. Let us consider the families of truncated triangles shown in Figure A.1. In A.1a, one corner of the triangle is progressively truncated. In A.1b, all three corners to the triangle are symmetrically truncated, preserving the three-fold symmetry of the original triangle; this truncation interpolates between a triangle and hexagon (six-fold rotational symmetry).

In both families, there is one shape in the family with higher symmetry than

the rest; the triangle and hexagons for a and b respectively. This is important to note, because our Hamiltonian H has a one- and three-fold rotational symmetry, respectively.

$$H \rightarrow H(t) \tag{A.9}$$

where t is the degree of truncation on the specified vertex/vertices. We can define $\mu_s(t)$, a conjugate variable to the particle truncation t [164]; we can think about taking a path along μ_s to do thermodynamic work.

Moving on, we consider the crystal structures formed by the single truncation particles, shown in Figure A.2. Hard triangles will fill space in a triangular tiling. If we begin to truncate one of the tips, there are two options - an orientationally ordered, space filling packing of trapezoids or a three-fold orientationally degenerate triangular tiling.

Now, at zero truncation, we notice that the orientationally degenerate structure and orientationally ordered structure are identical, if we ignore the yellow tips. It might be tempting to wonder whether the orientations of the triangles are “distinguishable.” This issue is closely related to the Gibbs paradox[165, 166]. As per Jaynes [165], the clearest way around any confusion whether particle labels are distinguishable is to imagine extracting work in a way in which the particle labels matter.

For triangles, we can imagine starting with highly truncated triangles in the rotationally ordered crystals. As we decrease the truncation level, the penalty for packing in the orientationally degenerate structure decreases, while the entropy gain remains the same - there will eventually be a transition from one to the other. At fixed pressure, this transition

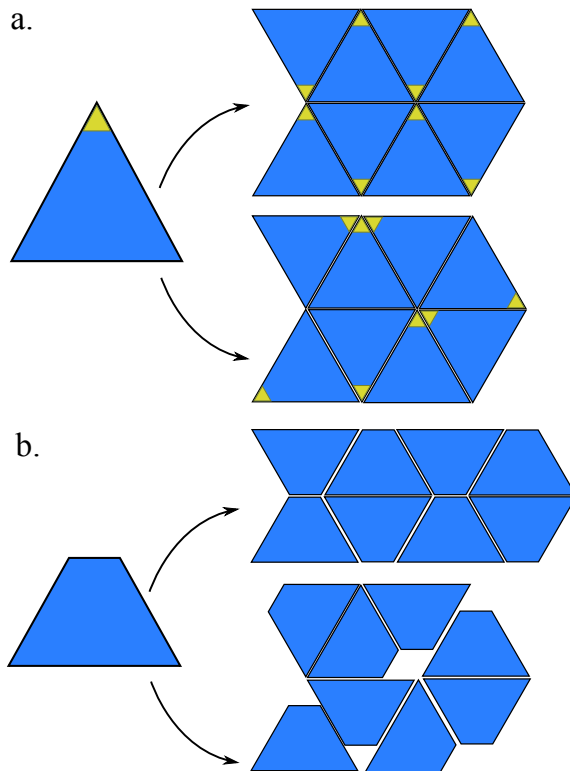


Figure A.2: Singly truncated triangle crystals. a) Orientationally ordered(top) and degenerate(bottom) crystals at zero-truncation. b) Orientationally order(top) and degenerate(bottom) crystals.

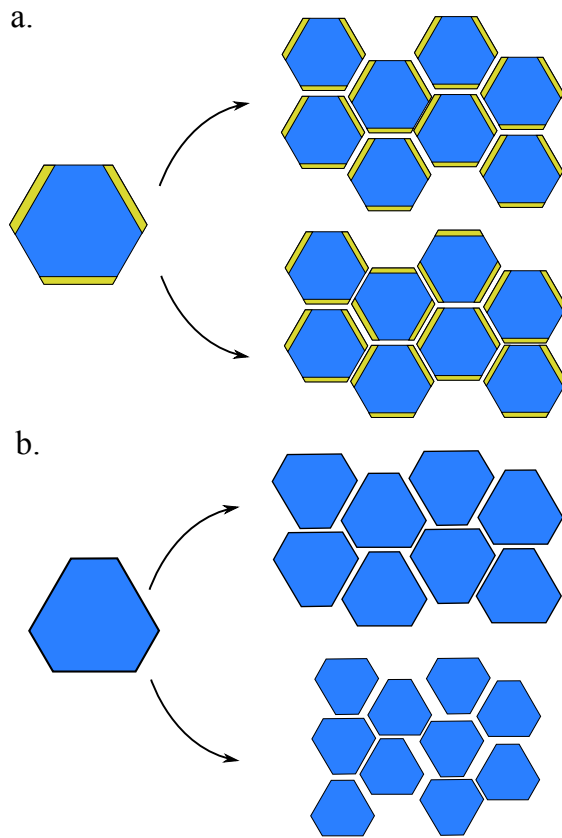


Figure A.3: Triply truncation triangle crystal. a) Orientationally ordered(top) and degenerate(bottom) crystals at zero-truncation. b) Orientationally order(top) and degenerate(bottom) crystals.

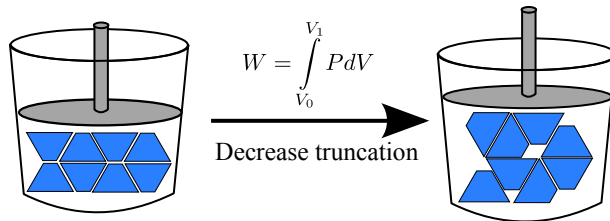


Figure A.4: Extraction of work from changing particle truncation.

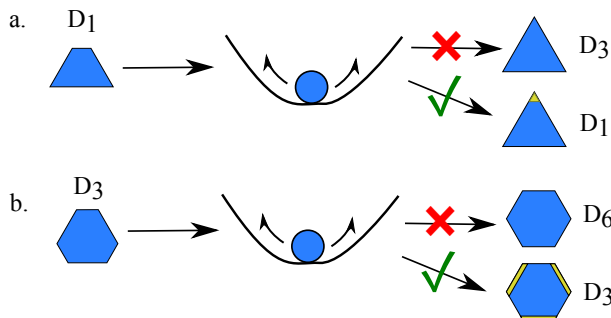


Figure A.5: Valid thermodynamic integration paths for singly and triply truncated triangles will result in a net volume gain due to packing inefficiencies (as in Figure A.4. Clearly in this “shape ensemble,”[164] the actual orientation of the particles matters and affects the work that can be extracted.

So, even in the perfect triangle limit, we must track the symmetric orientations as distinguishable because we can extract work from the system by manipulating the particle shape in a way that depends on the precise orientation of the triangle. Appropriate thermodynamic paths are illustrated in Figure A.5.

For the second family, we have an analogous situation for the hexagons. The hexagons must be treated as three-fold symmetric shapes, rather than six fold if we wish to compare the free energy of its crystals with crystals of other shapes in this family.

Alternately, we recognize the fact that the Hamiltonian has a one- and three-

fold symmetry in these cases. Even though for certain values of this parameter t , the Hamiltonian might have higher symmetry, the symmetry of the Hamiltonian in a thermodynamic ensemble in which we are allowing t to fluctuate is the lowest symmetry that can be achieved for any value of t .

Frenkel Ladd calculations in mixtures

We may also be interested in computing the free energy of shape mixtures. One simple example is that of an occupationally degenerate crystal, where the species at each lattice site is completely random compared to a binary crystal with specified particle positions. In this case, a membrane could be used to extract mechanical work. An occupationally degenerate crystal has a term equivalent to lattice gas mixing entropy that would not be sampled by Frenkel-Ladd integration and requires explicit addition.

Another system of interest is one comprised of complementarily shaped particles; polygons are split into halves with interlocking teeth, shown in Figure A.6. The premise is that these particle halves will find each other and self-assemble into paired crystals. The teeth on the particles can be described by a triangular wave of a certain frequency - at certain frequencies, the particle halves are self-complementary. That means at certain frequencies we have a single component system and at others we have a binary mixtures. We would like to compare the relative free energies of shapes that are self-complementary and those that are not.

The Hamiltonian for this family of particles depends on modifying the left and

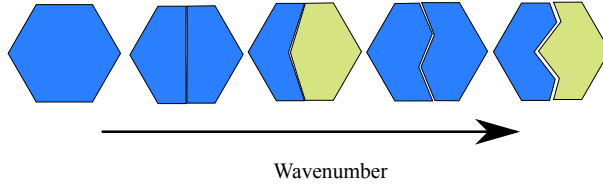


Figure A.6: Family of complementary, hexagon-forming particles

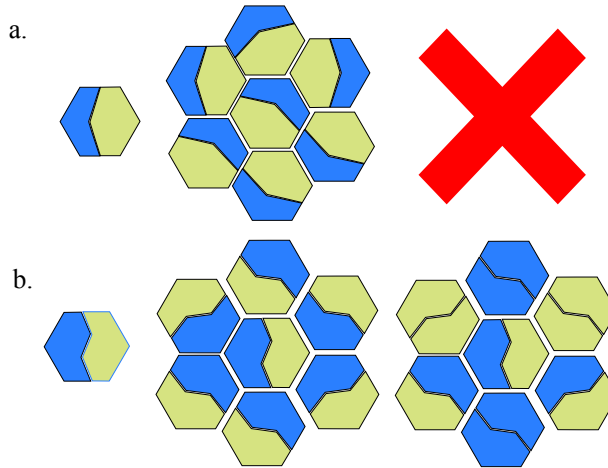


Figure A.7: Crystals formed by a) complementary and b) self-complementary particles

right halves of particles; the Hamiltonian dictates that we label particles “left” and “right” even if they are identical for a particle wavenumber. Figure A.7 illustrates the types of crystals that complementary and self-complementary shapes can form. There are a number of degeneracies. Both A.7a and A.7b have a six-fold rotational degeneracy. Additionally, the even-wavenumber particles in A.7 also have occupational degeneracy.

Moving forward, we count the number of ways to distribute labels to the particles. For the complementary particles we must place a left and right particle at each lattice site. For self-complementary particles, we can place one left and one right particle, or two lefts or two rights, subject to the global constraint that there must be an equal number of left and right particles.

To count the number of ways to distribute the left and right particles, we imagine placing $\frac{N}{2}$ left-particles on N lattice sites and filling in the rest with right particles. The problem here is that the lattice sites with two left or two right only have a three-fold rotational degeneracies. Like dealing with truncated triangles, the easiest way to proceed is to select the lowest symmetry in the system. Before, we constrained by a parameterized Hamiltonian of the shape. Here, we are constrained by the Frenkel Ladd Hamiltonian, which contains information about the particle type - a paired crystal containing some sites with only three-fold symmetry.

To proceed correctly, we select an instance of the three-fold degenerate crystal. First we count the number of ways that left and right pairs can be placed on these lattice sites - simply $2^{\frac{N}{2}}$. Then we count the number of ways to distribute $\frac{N}{2}$ particles onto N lattice sites for the self-complementary case. There are $\binom{N}{\frac{N}{2}}$ ways of doing this. Thus, the net difference in entropy between these two states is

$$\Delta S = k_b \left(\ln \left(\binom{N}{\frac{N}{2}} \right) - \ln \left(2^{\frac{N}{2}} \right) \right) \Delta S = \frac{Nk_B}{2} \ln(2) \quad (\text{A.10})$$

Perhaps the simplest way to think about this is to consider that the Hamiltonian we use to perform Frenkel Ladd integration has no notion of orientational degeneracy. In this case we must consider that for the left and right paired crystal, there are $6^{\frac{N}{2}}$ instances for each Frenkel Ladd Hamiltonian. In the case of the left and right particles being identical, we are reduced to $3^{\frac{N}{2}}$ rotationally degenerate states for each of the $\binom{N}{\frac{N}{2}}$ possible pairings. This yields the exact same expression for the entropy difference and the approach

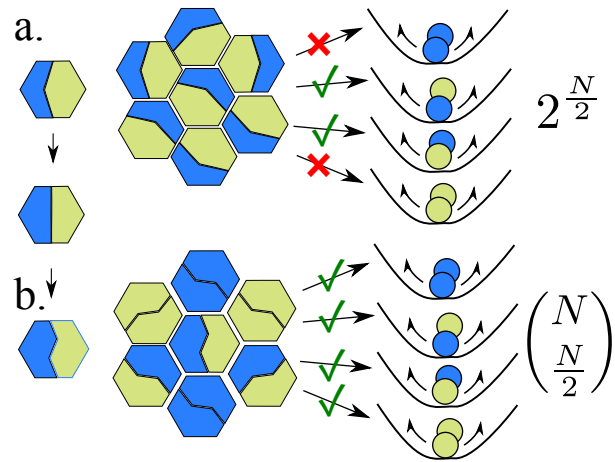


Figure A.8: Thermodynamic integration path to compare complementary and self-complementary particles

is illustrated in Figure A.8.

Bibliography

- [1] John A Pelesko. *Self Assembly: The Science of Things That Put Themselves Together: John A. Pelesko: 9781584886877: Amazon.com: Books*. Chapman and Hall/CRC, Boca Raton, FL, 2014 edition, 2007. ISBN 1584886870.
- [2] R. G. Bower, A. J. Benson, R. Malbon, J. C. Helly, C. S. Frenk, C. M. Baugh, S. Cole, and C. G. Lacey. Breaking the hierarchy of galaxy formation. *Monthly Notices of the Royal Astronomical Society*, 370(2):645–655, August 2006. ISSN 0035-8711. doi: 10.1111/j.1365-2966.2006.10519.x.
- [3] George M Whitesides and Bartosz Grzybowski. Self-assembly at all scales. *Science*, 295(5564):2418–21, March 2002. ISSN 1095-9203. doi: 10.1126/science.1070821.
- [4] Leigh Tesfatsion. Agent-based computational economics: growing economies from the bottom up. *Artificial life*, 8(1):55–82, January 2002. ISSN 1064-5462. doi: 10.1162/106454602753694765.
- [5] Shuguang Zhang. Fabrication of novel biomaterials through molecular self-assembly. *Nature biotechnology*, 21(10):1171–8, October 2003. ISSN 1087-0156. doi: 10.1038/nbt874.
- [6] Dinakar M. Salunke, Donald L.D. Caspar, and Robert L. Garcea. Self-assembly of purified polyomavirus capsid protein VP1. *Cell*, 46(6):895–904, September 1986. ISSN 00928674. doi: 10.1016/0092-8674(86)90071-1.
- [7] Samir Mitragotri and Joerg Lahann. Physical approaches to biomaterial design. *Nature Materials*, 8(1):15–23, January 2009. ISSN 1476-1122. doi: 10.1038/nmat2344.
- [8] Mark Yim, Wei-min Shen, Behnam Salemi, Daniela Rus, Mark Moll, Hod Lipson, Eric Klavins, and Gregory Chirikjian. Modular Self-Reconfigurable Robot Systems [Grand Challenges of Robotics]. *IEEE Robotics & Automation Magazine*, 14(1):43–52, March 2007. ISSN 1070-9932. doi: 10.1109/MRA.2007.339623.
- [9] Jonas Neubert, Abraham P Cantwell, Stephane Constantin, Michael Kalontarov, David Erickson, and Hod Lipson. A robotic module for stochastic fluidic assembly of 3D self-reconfiguring structures. In *2010 IEEE International Conference on Robotics*

- and Automation*, pages 2479–2484. IEEE, May 2010. ISBN 978-1-4244-5038-1. doi: 10.1109/ROBOT.2010.5509455.
- [10] Kyle J M Bishop, Christopher E Wilmer, Siowling Soh, and Bartosz A Grzybowski. Nanoscale forces and their uses in self-assembly. *Small*, 5(14):1600–30, July 2009. ISSN 1613-6829. doi: 10.1002/smll.200900358.
- [11] Henk N.W. Lekkerkerker and Remco Tuinier. *Colloids and the Depletion Interaction*. Springer Science & Business Media, 2011. ISBN 9400712227.
- [12] Donald Allan McQuarrie. *Statistical Mechanics*. University Science Books, 2000. ISBN 1891389157.
- [13] Daan Frenkel and Berend Smit. *Understanding Molecular Simulation: From Algorithms to Applications*. Academic Press, 2001. ISBN 0080519989.
- [14] S C Glotzer and M J Solomon. Anisotropy of building blocks and their assembly into complex structures. *Nature Materials*, 6:557–562, 2007.
- [15] Shan Jiang, Qian Chen, Mukta Tripathy, Erik Luijten, Kenneth S Schweizer, and Steve Granick. Janus particle synthesis and assembly. *Advanced materials (Deerfield Beach, Fla.)*, 22(10):1060–71, March 2010. ISSN 1521-4095. doi: 10.1002/adma.200904094.
- [16] Joel Henzie, Michael Grünwald, Asaph Widmer-Cooper, Phillip L Geissler, and Peidong Yang. Self-assembly of uniform polyhedral silver nanocrystals into densest packings and exotic superlattices. *Nature Materials*, 11(2):131–7, February 2012. ISSN 1476-1122. doi: 10.1038/nmat3178.
- [17] Karol Miszta, Joost de Graaf, Giovanni Bertoni, Dirk Dorfs, Rosaria Brescia, Sergio Marras, Luca Ceseracciu, Roberto Cingolani, René van Roij, Marjolein Dijkstra, and Liberato Manna. Hierarchical self-assembly of suspended branched colloidal nanocrystals into superlattice structures. *Nature Materials*, 10(11):872–6, November 2011. ISSN 1476-1122. doi: 10.1038/nmat3121.
- [18] Edwin Snoeks, Alfons van Blaaderen, Teun van Dillen, Carlos M van Kats, Mark L Brongersma, and Albert Polman. Colloidal ellipsoids with continuously variable shape. *Advanced Materials*, 12(20):1511–1514, 2000.
- [19] J.F. Favier, M.H. AbbaspourFard, M. Kremmer, and A.O. Raji. Shape representation of axisymmetrical, nonspherical particles in discrete element simulation using multi-element model particles. *Engineering Computations*, 16(4):467–480, June 1999. ISSN 0264-4401. doi: 10.1108/02644409910271894.
- [20] Marjolein Dijkstra. *Advances in Chemical Physics, Advances in Chemical Physics*, volume 156. John Wiley & Sons, 2014.

- [21] Daan Frenkel. Entropy-driven phase transitions. *Physica A: Statistical Mechanics and its Applications*, 263(1-4):26–38, February 1999. ISSN 03784371. doi: 10.1016/S0378-4371(98)00501-9.
- [22] G. van Anders, D. Klotsa, N. K. Ahmed, M. Engel, and S. C. Glotzer. Understanding shape entropy through local dense packing. *Proceedings of the National Academy of Sciences*, 111(45):E4812–4821, October 2014. ISSN 0027-8424. doi: 10.1073/pnas.1418159111.
- [23] P. N. Pusey and W. van Meegen. Phase behaviour of concentrated suspensions of nearly hard colloidal spheres. *Nature*, 320:340–342, 1986. ISSN 0028-0836. doi: 10.1038/320340a0.
- [24] Pablo F Damasceno, Michael Engel, and Sharon C Glotzer. Predictive self-assembly of polyhedra into complex structures. *Science*, 337(6093):453–7, July 2012. ISSN 1095-9203.
- [25] Umang Agarwal and Fernando A Escobedo. Mesophase behaviour of polyhedral particles. *Nature Materials*, 10(3):230–5, March 2011. ISSN 1476-1122. doi: 10.1038/nmat2959.
- [26] Mihir Khadilkar, Umang Agarwal, and Fernando Escobedo. Phase behavior of binary mixtures of convex hard polyhedra. *Soft Matter*, October 2013. ISSN 1744-683X.
- [27] Amir Haji-Akbari, Elizabeth R. Chen, Michael Engel, and Sharon C. Glotzer. Packing and self-assembly of truncated triangular bipyramids. *Physical Review E*, 88(1):012127, July 2013. ISSN 1539-3755. doi: 10.1103/PhysRevE.88.012127.
- [28] Amir Haji-Akbari, Michael Engel, and Sharon C Glotzer. Phase diagram of hard tetrahedra. *The Journal of Chemical Physics*, 135(19):194101, November 2011. ISSN 1089-7690.
- [29] Frank Smallenburg, Laura Filion, Matthieu Marechal, and Marjolein Dijkstra. Vacancy-stabilized crystalline order in hard cubes. *Proceedings of the National Academy of Sciences of the United States of America*, 109(44):17886–90, October 2012. ISSN 1091-6490.
- [30] Anjan P. Gantapara, Joost de Graaf, René van Roij, and Marjolein Dijkstra. Phase Diagram and Structural Diversity of a Family of Truncated Cubes: Degenerate Close-Packed Structures and Vacancy-Rich States. *Physical Review Letters*, 111(1):015501, July 2013. ISSN 0031-9007.
- [31] Amir Haji-Akbari, Michael Engel, Aaron S Keys, Xiaoyu Zheng, Rolfe G Petschek, Peter Palffy-Muhoray, and Sharon C Glotzer. Disordered, quasicrystalline and crystalline phases of densely packed tetrahedra. *Nature*, 462(7274):773–7, December 2009. ISSN 1476-4687.

- [32] Sho Asakura and Fumio Oosawa. On Interaction between Two Bodies Immersed in a Solution of Macromolecules. *The Journal of Chemical Physics*, 22(7):1255, December 1954. ISSN 00219606. doi: 10.1063/1.1740347.
- [33] R Tuinier, J Rieger, and C G de Kruif. Depletion-induced phase separation in colloid-polymer mixtures. *Advances in Colloid and Interface Science*, 103(1):1–31, March 2003. ISSN 0001-8686. doi: 10.1016/S0001-8686(02)00081-7.
- [34] J Crocker and D Grier. Methods of Digital Video Microscopy for Colloidal Studies. *Journal of Colloid and Interface Science*, 179(1):298–310, April 1996. ISSN 00219797. doi: 10.1006/jcis.1996.0217.
- [35] Elizabeth R. Chen, Michael Engel, and Sharon C. Glotzer. Dense Crystalline Dimer Packings of Regular Tetrahedra. *Discrete & Computational Geometry*, 44(2):253–280, July 2010. ISSN 0179-5376.
- [36] Qian Chen, Sung Chul Bae, and Steve Granick. Directed self-assembly of a colloidal kagome lattice. *Nature*, 469(7330):381–4, January 2011. ISSN 1476-4687. doi: 10.1038/nature09713.
- [37] Xiaoming Mao, Qian Chen, and Steve Granick. Entropy favours open colloidal lattices. *Nature Materials*, 12(3):217–22, March 2013. ISSN 1476-1122. doi: 10.1038/nmat3496.
- [38] Francesco Sciortino, Achille Giacometti, and Giorgio Pastore. A numerical study of one-patch colloidal particles: from square-well to Janus. *Physical chemistry chemical physics : PCCP*, 12(38):11869–77, October 2010. ISSN 1463-9084. doi: 10.1039/c0cp00504e.
- [39] Daniel J Beltran-Villegas, Benjamin A Schultz, Nguyen H P Nguyen, Sharon C Glotzer, and Ronald G Larson. Phase behavior of Janus colloids determined by sedimentation equilibrium. *Soft Matter*, 10(26):4593–602, July 2014. ISSN 1744-6848. doi: 10.1039/c3sm53136h.
- [40] Sumit Gangwal, Olivier J Cayre, and Orlin D Velev. Dielectrophoretic assembly of metallodielectric Janus particles in AC electric fields. *Langmuir*, 24(23):13312–20, December 2008. ISSN 0743-7463. doi: 10.1021/la8015222.
- [41] Bin Ren, Aleksey Ruditskiy, Jung Hun Kevin Song, and Ilona Kretzschmar. Assembly behavior of iron oxide-capped Janus particles in a magnetic field. *Langmuir*, 28(2): 1149–56, January 2012. ISSN 1520-5827. doi: 10.1021/la203969f.
- [42] Jeremie Palacci, Stefano Sacanna, Asher Preska Steinberg, David J Pine, and Paul M Chaikin. Living crystals of light-activated colloidal surfers. *Science*, 339(6122):936–40, February 2013. ISSN 1095-9203. doi: 10.1126/science.1230020.

- [43] Robert J Macfarlane, Ryan V Thaner, Keith A Brown, Jian Zhang, Byeongdu Lee, Son-Binh T Nguyen, and Chad A Mirkin. Importance of the DNA "bond" in programmable nanoparticle crystallization. *Proceedings of the National Academy of Sciences of the United States of America*, 111(42):14995–15000, October 2014. ISSN 1091-6490. doi: 10.1073/pnas.1416489111.
- [44] Chuan Zhang, Robert J Macfarlane, Kaylie L Young, Chung Hang J Choi, Liangliang Hao, Evelyn Auyeung, Guoliang Liu, Xiaozhu Zhou, and Chad A Mirkin. A general approach to DNA-programmable atom equivalents. *Nature Materials*, 12(8):741–6, August 2013. ISSN 1476-1122. doi: 10.1038/nmat3647.
- [45] Yugang Zhang, Fang Lu, Kevin G Yager, Daniel van der Lelie, and Oleg Gang. A general strategy for the DNA-mediated self-assembly of functional nanoparticles into heterogeneous systems. *Nature Nanotechnology*, 8(11):865–72, November 2013. ISSN 1748-3395. doi: 10.1038/nnano.2013.209.
- [46] Zhen-Gang Wang and Baoquan Ding. DNA-based self-assembly for functional nanomaterials. *Advanced materials (Deerfield Beach, Fla.)*, 25(28):3905–14, July 2013. ISSN 1521-4095. doi: 10.1002/adma.201301450.
- [47] Pablo F Damasceno, Michael Engel, and Sharon C Glotzer. Crystalline assemblies and densest packings of a family of truncated tetrahedra and the role of directional entropic forces. *ACS Nano*, 6(1):609–14, January 2012. ISSN 1936-086X. doi: 10.1021/nn204012y.
- [48] Weikai Qi, Joost de Graaf, Fen Qiao, Sergio Marras, Liberato Manna, and Marjolein Dijkstra. Phase diagram of octapod-shaped nanocrystals in a quasi-two-dimensional planar geometry. *The Journal of Chemical Physics*, 138(15):154504, April 2013. ISSN 1089-7690.
- [49] Michael Engel, Joshua A. Anderson, Sharon C. Glotzer, Masaharu Isobe, Etienne P. Bernard, and Werner Krauth. Hard-disk equation of state: First-order liquid-hexatic transition in two dimensions with three simulation methods. *Physical Review E*, 87(4):042134, April 2013. ISSN 1539-3755. doi: 10.1103/PhysRevE.87.042134.
- [50] Ulrich Muller. *Symmetry Relationships between Crystal Structures: Applications of Crystallographic Group Theory in Crystal Chemistry (International Union of Crystallography Texts on Crystallography)*. Oxford University Press, USA, 2013.
- [51] Guangnan Meng, Natalie Arkus, Michael P Brenner, and Vinothan N Manoharan. The free-energy landscape of clusters of attractive hard spheres. *Science*, 327(5965):560–3, January 2010. ISSN 1095-9203.
- [52] Greg van Anders, N Khalid Ahmed, Ross Smith, Michael Engel, and Sharon C Glotzer. Entropically patchy particles: engineering valence through shape entropy. *ACS Nano*, 8(1):931–40, January 2014. ISSN 1936-086X. doi: 10.1021/nn4057353.

- [53] Pablo F Damasceno, Michael Engel, and Sharon C Glotzer. Crystalline Assemblies and Densest Packings of a Family of Truncated Tetrahedra and the Role of Directional Entropic Forces. *ACS Nano*, 6(1):23, September 2011. ISSN 1936-086X. doi: 10.1021/nn204012y.
- [54] Amir Haji-Akbari, Michael Engel, and Sharon C. Glotzer. Degenerate Quasicrystal of Hard Triangular Bipyramids. *Physical Review Letters*, 107(21):215702, November 2011. ISSN 0031-9007.
- [55] Y. Jiao, F. Stillinger, and S. Torquato. Optimal packings of superballs. *Physical Review E*, 79(4):041309, April 2009. ISSN 1539-3755.
- [56] Ran Ni, Anjan Prasad Gantapara, Joost de Graaf, René van Roij, and Marjolein Dijkstra. Phase diagram of colloidal hard superballs: from cubes via spheres to octahedra. *arXiv:1111.4357*, November 2011.
- [57] Yoav Kallus and Veit Elser. Dense-packing crystal structures of physical tetrahedra. *Physical Review E*, 83(3):036703, March 2011. ISSN 1539-3755.
- [58] Joost de Graaf, René van Roij, and Marjolein Dijkstra. Dense Regular Packings of Irregular Nonconvex Particles. *Physical Review Letters*, 107(15):155501, October 2011. ISSN 0031-9007.
- [59] Elizabeth R. Chen, Daphne Klotsa, Michael Engel, Pablo F. Damasceno, and Sharon C. Glotzer. Complexity in Surfaces of Densest Packings for Families of Polyhedra. *Physical Review X*, 4(1):011024, February 2014. ISSN 2160-3308.
- [60] Bettina S John, Carol Juhlin, and Fernando A Escobedo. Phase behavior of colloidal hard perfect tetragonal parallelepipeds. *The Journal of Chemical Physics*, 128(4):044909, January 2008. ISSN 0021-9606. doi: 10.1063/1.2819091.
- [61] Mihir R Khadilkar and Fernando A Escobedo. Self-assembly of binary space-tessellating compounds. *The Journal of Chemical Physics*, 137(19):194907, November 2012. ISSN 1089-7690.
- [62] S Torquato and Y Jiao. Dense packings of the Platonic and Archimedean solids. *Nature*, 460(7257):876–9, August 2009. ISSN 1476-4687.
- [63] Avni Jain, Jeffrey R. Errington, and Thomas M. Truskett. Inverse design of simple pairwise interactions with low-coordinated 3D lattice ground states. *Soft Matter*, 9(14):3866, March 2013. ISSN 1744-683X. doi: 10.1039/c3sm27785b.
- [64] A. Schofield. Binary hard-sphere crystals with the cesium chloride structure. *Physical Review E*, 64(5):051403, October 2001. ISSN 1063-651X. doi: 10.1103/PhysRevE.64.051403.

- [65] P. Bartlett, R. Ottewill, and P. Pusey. Superlattice formation in binary mixtures of hard-sphere colloids. *Physical Review Letters*, 68(25):3801–3804, June 1992. ISSN 0031-9007. doi: 10.1103/PhysRevLett.68.3801.
- [66] Jaime A Millan, Daniel Ortiz, Greg van Anders, and Sharon C Glotzer. Self-assembly of archimedean tilings with enthalpically and entropically patchy polygons. *ACS Nano*, 8(3):2918–28, March 2014. ISSN 1936-086X. doi: 10.1021/nn500147u.
- [67] Peter Schultz, Kevin Leung, and E. Stechel. Small rings and amorphous tetrahedral carbon. *Physical Review B*, 59(2):733–741, January 1999. ISSN 0163-1829.
- [68] Amir Haji-Akbari, Elizabeth R. Chen, Michael Engel, and Sharon C. Glotzer. Packing and self-assembly of truncated triangular bipyramids. *Physical Review E*, 88(1):012127, July 2013. ISSN 1539-3755. doi: 10.1103/PhysRevE.88.012127.
- [69] Matthieu Marechal and Marjolein Dijkstra. Stability of orientationally disordered crystal structures of colloidal hard dumbbells. *Physical Review E*, 77(6):061405, June 2008. ISSN 1539-3755.
- [70] C P Royall, M E Leunissen, and A van Blaaderen. A new colloidal model system to study long-range interactions quantitatively in real space. *Journal of Physics: Condensed Matter*, 15(48):S3581–S3596, December 2003. ISSN 0953-8984. doi: 10.1088/0953-8984/15/48/017.
- [71] U Gasser, E R Weeks, A Schofield, P N Pusey, and D A Weitz. Real-space imaging of nucleation and growth in colloidal crystallization. *Science*, 292(5515):258–62, April 2001. ISSN 0036-8075. doi: 10.1126/science.1058457.
- [72] William T M Irvine, Mark J Bowick, and Paul M Chaikin. Fractionalization of interstitials in curved colloidal crystals. *Nature Materials*, 11(11):948–51, November 2012. ISSN 1476-1122. doi: 10.1038/nmat3429.
- [73] Fabian M. Schaller, Max Neudecker, Mohammad Saadatfar, Gary Delaney, Gerd E. Schröder-Turk, and Matthias Schröter. Local origin of global contact numbers in frictional ellipsoid packings. *arXiv:1312.1327*, December 2013.
- [74] J Bohm, A S Frangakis, R Hegerl, S Nickell, D Typke, and W Baumeister. Toward detecting and identifying macromolecules in a cellular context: template matching applied to electron tomograms. *Proceedings of the National Academy of Sciences of the United States of America*, 97(26):14245–50, December 2000. ISSN 0027-8424. doi: 10.1073/pnas.230282097.
- [75] Mathieu Leocmach and Hajime Tanaka. A novel particle tracking method with individual particle size measurement and its application to ordering in glassy hard sphere colloids. *Soft Matter*, 9(5):1447, January 2013. ISSN 1744-683X. doi: 10.1039/c2sm27107a.

- [76] Ali Mohraz and Michael J Solomon. Direct visualization of colloidal rod assembly by confocal microscopy. *Langmuir*, 21(12):5298–306, June 2005. ISSN 0743-7463. doi: 10.1021/la046908a.
- [77] T. H. Besseling, M. Hermes, A. Kuijk, B. de Nijs, T. S. Deng, M. Dijkstra, A. Imhof, and A. van Blaaderen. Determination of the positions and orientations of concentrated rod-like colloids from 3D microscopy data. *arXiv:1406.4985*, June 2014.
- [78] Aayush A Shah, Benjamin Schultz, Kevin L Kohlstedt, Sharon C Glotzer, and Michael J Solomon. Synthesis, assembly, and image analysis of spheroidal patchy particles. *Langmuir*, 29(15):4688–96, April 2013. ISSN 1520-5827. doi: 10.1021/la400317t.
- [79] Max Neudecker, Stephan Ulrich, Stephan Herminghaus, and Matthias Schröter. Jammed Frictional Tetrahedra are Hyperstatic. *Physical Review Letters*, 111(2): 028001, July 2013. ISSN 0031-9007. doi: 10.1103/PhysRevLett.111.028001.
- [80] Kejia Chen, Stephen M Anthony, and Steve Granick. Extending particle tracking capability with Delaunay triangulation. *Langmuir*, 30(16):4760–6, April 2014. ISSN 1520-5827. doi: 10.1021/la500323r.
- [81] J. Cousty, G. Bertrand, L. Najman, and M. Couprie. Watershed cuts: Thinnings, shortest path forests, and topological watersheds. *Pattern Analysis and Machine Intelligence, IEEE Transactions on*, 32(5):925–939, May 2010. ISSN 0162-8828. doi: 10.1109/TPAMI.2009.71.
- [82] A Aggeli, I A Nyrkova, M Bell, R Harding, L Carrick, T C McLeish, A N Semenov, and N Boden. Hierarchical self-assembly of chiral rod-like molecules as a model for peptide beta -sheet tapes, ribbons, fibrils, and fibers. *Proceedings of the National Academy of Sciences of the United States of America*, 98(21):11857–62, October 2001. ISSN 0027-8424. doi: 10.1073/pnas.191250198.
- [83] Leonard R. MacGillivray and Jerry L. Atwood. A chiral spherical molecular assembly held together by 60 hydrogen bonds. *Nature*, 389(6650):469–472, October 1997. ISSN 0028-0836. doi: 10.1038/38985.
- [84] Javier Arsuaga, Mariel Vazquez, Paul McGuirk, Sonia Trigueros, De Witt Summers, and Joaquim Roca. DNA knots reveal a chiral organization of DNA in phage capsids. *Proceedings of the National Academy of Sciences of the United States of America*, 102(26):9165–9, June 2005. ISSN 0027-8424. doi: 10.1073/pnas.0409323102.
- [85] James C Mitchell, J Robin Harris, Jonathan Malo, Jonathan Bath, and Andrew J Turberfield. Self-assembly of chiral DNA nanotubes. *Journal of the American Chemical Society*, 126(50):16342–3, December 2004. ISSN 0002-7863. doi: 10.1021/ja043890h.
- [86] A. Stasiak. Knotted Fishing Line, Covalent Bonds, and Breaking Points. *Science*, 286(5437):11a–11, October 1999. ISSN 00368075. doi: 10.1126/science.286.5437.11a.

- [87] Jihyeon Yeom, Bongjun Yeom, Henry Chan, Kyle W Smith, Sergio Dominguez-Medina, Joong Hwan Bahng, Gongpu Zhao, Wei-Shun Chang, Sung-Jin Chang, Andrey Chuvilin, Dzmitry Melnikau, Andrey L Rogach, Peijun Zhang, Stephan Link, Petr Král, and Nicholas A Kotov. Chiral templating of self-assembling nanostructures by circularly polarized light. *Nature Materials*, 14(1):66–72, January 2015. ISSN 1476-1122. doi: 10.1038/nmat4125.
- [88] Wei Ma, Hua Kuang, Libing Wang, Liguang Xu, Wei-Shun Chang, Huanan Zhang, Maozhong Sun, Yinyue Zhu, Yuan Zhao, Liqiang Liu, Chuanlai Xu, Stephan Link, and Nicholas A Kotov. Chiral plasmonics of self-assembled nanorod dimers. *Scientific reports*, 3:1934, January 2013. ISSN 2045-2322. doi: 10.1038/srep01934.
- [89] Sudhanshu Srivastava, Aaron Santos, Kevin Critchley, Ki-Sub Kim, Paul Podsiadlo, Kai Sun, Jaebeom Lee, Chuanlai Xu, G Daniel Lilly, Sharon C Glotzer, and Nicholas A Kotov. Light-controlled self-assembly of semiconductor nanoparticles into twisted ribbons. *Science*, 327(5971):1355–9, March 2010. ISSN 1095-9203. doi: 10.1126/science.1177218.
- [90] Lingxiang Jiang, Julius W J de Folter, Jianbin Huang, Albert P Philipse, Willem K Kegel, and Andrei V Petukhov. Helical colloidal sphere structures through thermoreversible co-assembly with molecular microtubes. *Angewandte Chemie (International ed. in English)*, 52(12):3364–8, March 2013. ISSN 1521-3773. doi: 10.1002/anie.201209767.
- [91] Thomas Gibaud, Edward Barry, Mark J Zakhary, Mir Henglin, Andrew Ward, Yasheng Yang, Cristina Berciu, Rudolf Oldenbourg, Michael F Hagan, Daniela Nicastro, Robert B Meyer, and Zvonimir Dogic. Reconfigurable self-assembly through chiral control of interfacial tension. *Nature*, 481(7381):348–51, January 2012. ISSN 1476-4687. doi: 10.1038/nature10769.
- [92] Jérôme J Crassous, Adriana M Mihut, Erik Wernersson, Patrick Pfeleiderer, Jan Vermant, Per Linse, and Peter Schurtenberger. Field-induced assembly of colloidal ellipsoids into well-defined microtubules. *Nature Communications*, 5:5516, January 2014. ISSN 2041-1723. doi: 10.1038/ncomms6516.
- [93] Qian Chen, Jonathan K Whitmer, Shan Jiang, Sung Chul Bae, Erik Luijten, and Steve Granick. Supracolloidal reaction kinetics of Janus spheres. *Science*, 331(6014):199–202, January 2011. ISSN 1095-9203. doi: 10.1126/science.1197451.
- [94] Anton Kuzyk, Robert Schreiber, Zhiyuan Fan, Günther Pardatscher, Eva-Maria Roller, Alexander Högele, Friedrich C Simmel, Alexander O Govorov, and Tim Liedl. DNA-based self-assembly of chiral plasmonic nanostructures with tailored optical response. *Nature*, 483(7389):311–4, March 2012. ISSN 1476-4687. doi: 10.1038/nature10889.

- [95] R P Goodman, I A T Schaap, C F Tardin, C M Erben, R M Berry, C F Schmidt, and A J Turberfield. Rapid chiral assembly of rigid DNA building blocks for molecular nanofabrication. *Science*, 310(5754):1661–5, December 2005. ISSN 1095-9203. doi: 10.1126/science.1120367.
- [96] Dwaipayan Chakrabarti and David Wales. Tilted and Helical Columnar Phases for an Axially Symmetric Discoidal System. *Physical Review Letters*, 100(12):127801, March 2008. ISSN 0031-9007. doi: 10.1103/PhysRevLett.100.127801.
- [97] P Prybytak, W J Frith, and D J Cleaver. Hierarchical self-assembly of chiral fibres from achiral particles. *Interface focus*, 2(5):651–7, October 2012. ISSN 2042-8898. doi: 10.1098/rsfs.2011.0104.
- [98] Szilard Fejer and David Wales. Helix Self-Assembly from Anisotropic Molecules. *Physical Review Letters*, 99(8):086106, August 2007. ISSN 0031-9007. doi: 10.1103/PhysRevLett.99.086106.
- [99] Kun Zhao and Thomas Mason. Directing Colloidal Self-Assembly through Roughness-Controlled Depletion Attractions. *Physical Review Letters*, 99(26):268301, December 2007. ISSN 0031-9007. doi: 10.1103/PhysRevLett.99.268301.
- [100] Felix M. van der Kooij and Henk N. W. Lekkerkerker. Formation of Nematic Liquid Crystals in Suspensions of Hard Colloidal Platelets. *The Journal of Physical Chemistry B*, 102(40):7829–7832, October 1998. ISSN 1520-6106. doi: 10.1021/jp981534d.
- [101] van der Kooij FM, K Kassapidou, and HN Lekkerkerker. Liquid crystal phase transitions in suspensions of polydisperse plate-like particles. *Nature*, 406(6798):868–71, August 2000. ISSN 1476-4687. doi: 10.1038/35022535.
- [102] Barbara Ruzicka, Emanuela Zaccarelli, Laura Zulian, Roberta Angelini, Michael Sztucki, Abdellatif Moussaïd, Theyencheri Narayanan, and Francesco Sciortino. Observation of empty liquids and equilibrium gels in a colloidal clay. *Nature Materials*, 10(1):56–60, January 2011. ISSN 1476-1122. doi: 10.1038/nmat2921.
- [103] Masami Okamoto, Pham Hoai Nam, Pralay Maiti, Tadao Kotaka, Takashi Nakayama, Mitsuko Takada, Masahiro Ohshima, Arimitsu Usuki, Naoki Hasegawa, and Hirotaka Okamoto. Biaxial Flow-Induced Alignment of Silicate Layers in Polypropylene/Clay Nanocomposite Foam. *Nano Letters*, 1(9):503–505, September 2001. ISSN 1530-6984. doi: 10.1021/nl010051+.
- [104] E Paineau, K Antonova, C Baravian, I Bihannic, P Davidson, I Dozov, M Impérator-Clerc, P Levitz, A Madsen, F Meneau, and L J Michot. Liquid-crystalline nematic phase in aqueous suspensions of a disk-shaped natural beidellite clay. *The Journal of Physical Chemistry B*, 113(48):15858–69, December 2009. ISSN 1520-5207. doi: 10.1021/jp908326y.

- [105] R. Angelini and E. Zaccarelli. Glassglass transition during aging of a colloidal clay. *Nature Communications*, 5:4049, 2014.
- [106] M. Dijkstra, J. Hansen, and P.A. Madden. Gelation of a Clay Colloid Suspension. *Physical Review Letters*, 75(11):2236–2239, September 1995. ISSN 0031-9007. doi: 10.1103/PhysRevLett.75.2236.
- [107] Daniel Florea and Hans M Wyss. Towards the self-assembly of anisotropic colloids: monodisperse oblate ellipsoids. *Journal of Colloid and Interface Science*, 416:30–7, February 2014. ISSN 1095-7103. doi: 10.1016/j.jcis.2013.10.027.
- [108] Yongxing Hu, Jianping Ge, Tierui Zhang, and Yadong Yin. A Blown Film Process to Disk-Shaped Polymer Ellipsoids. *Advanced Materials*, 20(23):4599–4602, December 2008. ISSN 09359648. doi: 10.1002/adma.200801985.
- [109] L. Antl, J.W. Goodwin, R.D. Hill, R.H. Ottewill, S.M. Owens, S. Papworth, and J.A. Waters. The preparation of poly(methyl methacrylate) latices in non-aqueous media. *Colloids and Surfaces*, 17(1):67–78, January 1986. ISSN 01666622. doi: 10.1016/0166-6622(86)80187-1.
- [110] Andrew I. Campbell and Paul Bartlett. Fluorescent Hard-Sphere Polymer Colloids for Confocal Microscopy. *Journal of Colloid and Interface Science*, 256(2):325–330, December 2002. ISSN 00219797. doi: 10.1006/jcis.2002.8669.
- [111] Zhenkun Zhang, Patrick Pfeiderer, Andrew B Schofield, Christian Clasen, and Jan Vermant. Synthesis and directed self-assembly of patterned anisometric polymeric particles. *Journal of the American Chemical Society*, 133(3):392–5, January 2011. ISSN 1520-5126. doi: 10.1021/ja108099r.
- [112] Howard Brenner. Rheology of a dilute suspension of axisymmetric Brownian particles. *International Journal of Multiphase Flow*, 1(2):195–341, April 1974. ISSN 03019322. doi: 10.1016/0301-9322(74)90018-4.
- [113] Deshpremy Mukhija and Michael J Solomon. Translational and rotational dynamics of colloidal rods by direct visualization with confocal microscopy. *Journal of Colloid and Interface Science*, 314(1):98–106, October 2007. ISSN 0021-9797. doi: 10.1016/j.jcis.2007.05.055.
- [114] Clare Dibble, Michael Kogan, and Michael Solomon. Structure and dynamics of colloidal depletion gels: Coincidence of transitions and heterogeneity. *Physical Review E*, 74(4):041403, October 2006. ISSN 1539-3755. doi: 10.1103/PhysRevE.74.041403.
- [115] Isla Zhang, C. Patrick Royall, Malcolm A. Faers, and Paul Bartlett. Phase separation dynamics in colloidpolymer mixtures: the effect of interaction range. *Soft Matter*, 9(6):2076, January 2013. ISSN 1744-683X. doi: 10.1039/c2sm27119b.

- [116] Sandra Wegner, Tamás Börzsönyi, Tomasz Bien, Georg Rose, and Ralf Stannarius. Alignment and dynamics of elongated cylinders under shear. *Soft Matter*, 8(42):10950, October 2012. ISSN 1744-683X. doi: 10.1039/c2sm26452h.
- [117] Leonid Paramonov and Sophia N Yaliraki. The directional contact distance of two ellipsoids: coarse-grained potentials for anisotropic interactions. *The Journal of Chemical Physics*, 123(19):194111, November 2005. ISSN 0021-9606. doi: 10.1063/1.2102897.
- [118] Joshua A. Anderson and Sharon C. Glotzer. The development and expansion of HOOMD-blue through six years of GPU proliferation. *arXiv:1308.5587*, August 2013.
- [119] Peter Bolhuis and Daan Frenkel. Numerical study of the phase diagram of a mixture of spherical and rodlike colloids. *The Journal of Chemical Physics*, 101(11):9869, December 1994. ISSN 00219606. doi: 10.1063/1.467953.
- [120] Wenping Wang, Jiaye Wang, and Myung-Soo Kim. An algebraic condition for the separation of two ellipsoids. *Computer Aided Geometric Design*, 18(6):531–539, July 2001. ISSN 01678396. doi: 10.1016/S0167-8396(01)00049-8.
- [121] Salvatore Alfano and Meredith L. Greer. Determining If Two Solid Ellipsoids Intersect. *Journal of Guidance Control and Dynamics*, 26(1), January 2003.
- [122] Xiaoyu Zheng, Wilder Iglesias, and Peter Palffy-Muhoray. Distance of closest approach of two arbitrary hard ellipsoids. *Physical Review E - Statistical, Nonlinear, and Soft Matter Physics*, 79:2–5, 2009. ISSN 15393755. doi: 10.1103/PhysRevE.79.057702.
- [123] Jacques Charles François Sturm. Mémoire sur la résolution des équations numériques. *Bulletin des Sciences de Férussac*, 11:419–425, 1829.
- [124] Lilian C Hsiao, Richmond S Newman, Sharon C Glotzer, and Michael J Solomon. Role of isostaticity and load-bearing microstructure in the elasticity of yielded colloidal gels. *Proceedings of the National Academy of Sciences of the United States of America*, 109(40):16029–34, October 2012. ISSN 1091-6490. doi: 10.1073/pnas.1206742109.
- [125] Francesco Sciortino, Stefano Mossa, Emanuela Zaccarelli, and Piero Tartaglia. Equilibrium Cluster Phases and Low-Density Arrested Disordered States: The Role of Short-Range Attraction and Long-Range Repulsion. *Physical Review Letters*, 93(5):055701, July 2004. ISSN 0031-9007. doi: 10.1103/PhysRevLett.93.055701.
- [126] Andrew Campbell, Valerie Anderson, Jeroen van Duijneveldt, and Paul Bartlett. Dynamical Arrest in Attractive Colloids: The Effect of Long-Range Repulsion. *Physical Review Letters*, 94(20):208301, May 2005. ISSN 0031-9007. doi: 10.1103/PhysRevLett.94.208301.
- [127] S Mossa, F Sciortino, P Tartaglia, and E Zaccarelli. Ground-state clusters for short-range attractive and long-range repulsive potentials. *Langmuir*, 20(24):10756–63, November 2004. ISSN 0743-7463. doi: 10.1021/la048554t.

- [128] Stephen Whitelam and Phillip L Geissler. Avoiding unphysical kinetic traps in Monte Carlo simulations of strongly attractive particles. *The Journal of chemical physics*, 127(15):154101, October 2007. ISSN 0021-9606. doi: 10.1063/1.2790421.
- [129] Eric Jankowski and Sharon C. Glotzer. A comparison of new methods for generating energy-minimizing configurations of patchy particles. *The Journal of Chemical Physics*, 131(10):104104, September 2009. ISSN 00219606. doi: 10.1063/1.3223834. URL <http://scitation.aip.org/content/aip/journal/jcp/131/10/10.1063/1.3223834>.
- [130] Douglas J. Ashton, Robert L. Jack, and Nigel B. Wilding. Self-assembly of colloidal polymers via depletion-mediated lock and key binding. *Soft Matter*, 9(40):9661, September 2013. ISSN 1744-683X. doi: 10.1039/c3sm51839f. URL <http://pubs.rsc.org/en/content/articlehtml/2013/sm/c3sm51839f>.
- [131] Kirstin Purdy, Zvonimir Dogic, Seth Fraden, Adrian Rühm, Lawrence Lurio, and Simon Mochrie. Measuring the nematic order of suspensions of colloidal fd virus by x-ray diffraction and optical birefringence. *Physical Review E*, 67(3):031708, March 2003. ISSN 1063-651X. doi: 10.1103/PhysRevE.67.031708.
- [132] Michael J. Solomon and Patrick T. Spicer. Microstructural regimes of colloidal rod suspensions, gels, and glasses. *Soft Matter*, 6(7):1391, March 2010. ISSN 1744-683X. doi: 10.1039/b918281k.
- [133] Aayush A Shah, Benjamin Schultz, Wenjia Zhang, Sharon C Glotzer, and Michael J Solomon. Actuation of shape-memory colloidal fibres of Janus ellipsoids. *Nature Materials*, 14(1):117–124, November 2014. ISSN 1476-1122. doi: 10.1038/nmat4111.
- [134] Amar B Pawar and Ilona Kretzschmar. Fabrication, assembly, and application of patchy particles. *Macromolecular Rapid Communications*, 31(2):150–68, January 2010. ISSN 1521-3927. doi: 10.1002/marc.200900614.
- [135] Lang Feng, Rémi Dreyfus, Ruojie Sha, Nadrian C Seeman, and Paul M Chaikin. DNA patchy particles. *Advanced materials (Deerfield Beach, Fla.)*, 25(20):2779–83, May 2013. ISSN 1521-4095. doi: 10.1002/adma.201204864.
- [136] Zhenli Zhang, Aaron S Keys, Ting Chen, and Sharon C Glotzer. Self-assembly of patchy particles into diamond structures through molecular mimicry. *Langmuir*, 21(25):11547–51, December 2005. ISSN 0743-7463. doi: 10.1021/la0513611.
- [137] Robert Vácha and Daan Frenkel. Relation between molecular shape and the morphology of self-assembling aggregates: a simulation study. *Biophysical journal*, 101(6):1432–9, September 2011. ISSN 1542-0086. doi: 10.1016/j.bpj.2011.07.046.
- [138] Ya Liu, Wei Li, Toni Perez, James D Gunton, and Genevieve Brett. Self assembly of Janus ellipsoids. *Langmuir*, 28(1):3–9, January 2012. ISSN 1520-5827. doi: 10.1021/la2032303.

- [139] Kundan Chaudhary, Qian Chen, Jaime J Juárez, Steve Granick, and Jennifer A Lewis. Janus colloidal matchsticks. *Journal of the American Chemical Society*, 134(31):12901–3, August 2012. ISSN 1520-5126. doi: 10.1021/ja305067g.
- [140] Anke Kuijk, Alfons van Blaaderen, and Arnout Imhof. Synthesis of monodisperse, rodlike silica colloids with tunable aspect ratio. *Journal of the American Chemical Society*, 133(8):2346–9, March 2011. ISSN 1520-5126. doi: 10.1021/ja109524h.
- [141] Simon O. Lumsdon, Eric W. Kaler, and Orlin D. Velev. Two-Dimensional Crystallization of Microspheres by a Coplanar AC Electric Field. *Langmuir*, 20(6):2108–2116, March 2004. ISSN 0743-7463. doi: 10.1021/la035812y.
- [142] John Singh, Pushkar Lele, Florian Nettesheim, Norman Wagner, and Eric Furst. One- and two-dimensional assembly of colloidal ellipsoids in ac electric fields. *Physical Review E*, 79(5):050401, May 2009. ISSN 1539-3755. doi: 10.1103/PhysRevE.79.050401.
- [143] Anand Yethiraj, Alan Wouterse, Benito Groh, and Alfons van Blaaderen. Nature of an Electric-Field-Induced Colloidal Martensitic Transition. *Physical Review Letters*, 92(5):058301, February 2004. ISSN 0031-9007. doi: 10.1103/PhysRevLett.92.058301.
- [144] Ahmet Faik Demirörs, Patrick M Johnson, Carlos M van Kats, Alfons van Blaaderen, and Arnout Imhof. Directed self-assembly of colloidal dumbbells with an electric field. *Langmuir*, 26(18):14466–71, September 2010. ISSN 1520-5827. doi: 10.1021/la102134w.
- [145] David A. Porter and Kenneth E. Easterling. *Phase Transformations in Metals and Alloys, Third Edition (Revised Reprint)*. CRC Press, 1992. ISBN 0748757414.
- [146] Trung Dac Nguyen, Carolyn L. Phillips, Joshua A. Anderson, and Sharon C. Glotzer. Rigid body constraints realized in massively-parallel molecular dynamics on graphics processing units. *Computer Physics Communications*, 182(11):2307–2313, November 2011. ISSN 00104655. doi: 10.1016/j.cpc.2011.06.005.
- [147] Kun Liu, Zhihong Nie, Nana Zhao, Wei Li, Michael Rubinstein, and Eugenia Kumacheva. Step-growth polymerization of inorganic nanoparticles. *Science*, 329(5988):197–200, July 2010. ISSN 1095-9203. doi: 10.1126/science.1189457.
- [148] Kundan Chaudhary, Jaime J Juárez, Qian Chen, Steve Granick, and Jennifer A Lewis. Reconfigurable assemblies of Janus rods in AC electric fields. *Soft Matter*, 10(9):1320–4, March 2014. ISSN 1744-6848. doi: 10.1039/c3sm52418c.
- [149] Thomas Halsey and Will Toor. Structure of electrorheological fluids. *Physical Review Letters*, 65(22):2820–2823, November 1990. ISSN 0031-9007. doi: 10.1103/PhysRevLett.65.2820.

- [150] Kipton Barros, Daniel Sinkovits, and Erik Luijten. Efficient and accurate simulation of dynamic dielectric objects. *The Journal of Chemical Physics*, 140(6):064903, February 2014. ISSN 1089-7690. doi: 10.1063/1.4863451.
- [151] C Wyatt Shields, Shan Zhu, Ye Yang, Bhuvnesh Bharti, Jonathan Liu, Benjamin B Yellen, Orlin D Velev, and Gabriel P López. Field-directed of patchy anisotropic microparticles with defined shape. *Soft Matter*, 9(38):9219–29, September 2013. ISSN 1744-6848. doi: 10.1039/c3sm51119g.
- [152] Marileen Dogterom, Jacob W J Kerssemakers, Guillaume Romet-Lemonne, and Marcel E Janson. Force generation by dynamic microtubules. *Current Opinion in Cell Biology*, 17(1):67–74, February 2005. ISSN 0955-0674. doi: 10.1016/j.ceb.2004.12.011.
- [153] W A Linke, V I Popov, and G H Pollack. Passive and active tension in single cardiac myofibrils. *Biophysical journal*, 67(2):782–92, August 1994. ISSN 0006-3495. doi: 10.1016/S0006-3495(94)80538-7.
- [154] Matthew J Footer, Jacob W J Kerssemakers, Julie A Theriot, and Marileen Dogterom. Direct measurement of force generation by actin filament polymerization using an optical trap. *Proceedings of the National Academy of Sciences of the United States of America*, 104(7):2181–6, February 2007. ISSN 0027-8424. doi: 10.1073/pnas.0607052104.
- [155] A. L. Rogach, N. A. Kotov, D. S. Koktysh, J. W. Ostrander, and G. A. Ragoisha. Electrophoretic Deposition of Latex-Based 3D Colloidal Photonic Crystals: A Technique for Rapid Production of High-Quality Opals. *Chemistry of Materials*, 12(9): 2721–2726, September 2000. ISSN 0897-4756. doi: 10.1021/cm000274l.
- [156] Marek Grzelczak, Jan Vermant, Eric M Furst, and Luis M Liz-Marzán. Directed self-assembly of nanoparticles. *ACS Nano*, 4(7):3591–605, July 2010. ISSN 1936-086X. doi: 10.1021/nn100869j.
- [157] E C M Vermolen, A Kuijk, L C Filion, M Hermes, J H J Thijssen, M Dijkstra, and A van Blaaderen. Fabrication of large binary colloidal crystals with a NaCl structure. *Proceedings of the National Academy of Sciences of the United States of America*, 106 (38):16063–7, September 2009. ISSN 1091-6490. doi: 10.1073/pnas.0900605106.
- [158] Aayush A Shah, Heekyoung Kang, Kevin L Kohlstedt, Kyung Hyun Ahn, Sharon C Glotzer, Charles W Monroe, and Michael J Solomon. Liquid crystal order in colloidal suspensions of spheroidal particles by direct current electric field assembly. *Small*, 8 (10):1551–62, May 2012. ISSN 1613-6829. doi: 10.1002/sml.201102265.
- [159] W.B. Russel, D. A. Saville, and W. R. Schowalter. *Colloidal Dispersions*. Cambridge University Press, Cambridge, UK, 1999 edition, 1992. ISBN 9780521426008.

- [160] Sumit Gangwal, Amar Pawar, Ilona Kretzschmar, and Orlin D. Velev. Programmed assembly of metalodielectric patchy particles in external AC electric fields. *Soft Matter*, 6(7):1413, March 2010. ISSN 1744-683X. doi: 10.1039/b925713f.
- [161] Teun Vissers, Zdenek Preisler, Frank Smalenburg, Marjolein Dijkstra, and Francesco Sciortino. Predicting crystals of Janus colloids. *The Journal of Chemical Physics*, 138(16):164505, April 2013. ISSN 1089-7690. doi: 10.1063/1.4801438.
- [162] Shan Jiang, Jing Yan, Jonathan K. Whitmer, Stephen M. Anthony, Erik Luijten, and Steve Granick. Orientationally Glassy Crystals of Janus Spheres. *Physical Review Letters*, 112(21):218301, May 2014. ISSN 0031-9007. doi: 10.1103/PhysRevLett.112.218301.
- [163] Mirjam E Leunissen, Christina G Christova, Antti-Pekka Hynninen, C Patrick Royall, Andrew I Campbell, Arnout Imhof, Marjolein Dijkstra, René van Roij, and Alfons van Blaaderen. Ionic colloidal crystals of oppositely charged particles. *Nature*, 437(7056):235–40, September 2005. ISSN 1476-4687. doi: 10.1038/nature03946.
- [164] Greg van Anders, Daphne Klotsa, Andrew Karas, and Sharon C Glotzer. Shape ensembles of hard particles. *preprint*, 2015.
- [165] E T Jaynes. *Maximum Entropy and Bayesian Methods*. Springer Netherlands, Dordrecht, 1992. ISBN 978-90-481-4220-0. doi: 10.1007/978-94-017-2219-3.
- [166] Robert H. Swendsen. Statistical Mechanics of Classical Systems with Distinguishable Particles. *Journal of Statistical Physics*, 107(5-6):1143–1166, June 2002. ISSN 1572-9613. doi: 10.1023/A:1015161825292.